Synthesis and Integration of Functional Nanomaterials on Optical Fiber Platforms for Points and Distributed Sensing for Energy Applications

by

Rongtao Cao

B.S., Xidian University, 2011

M.S., Xidian University, 2014

Submitted to the Graduate Faculty of the

The Swanson School of Engineering in partial fulfillment

of the requirements for the degree of

Doctor of Philosophy

University of Pittsburgh

2020

UNIVERSITY OF PITTSBURGH

SWANSON SCHOOL OF ENGINEERING

This dissertation was presented

by

Rongtao Cao

It was defended on

January 10, 2020

and approved by

Kevin P. Chen, Ph.D., Professor, Department of Electrical and Computer Engineering

Guangyong Li, Ph.D., Associate Professor, Department of Electrical and Computer Engineering

Susheng Tan, Ph.D., Associate Professor, Department of Electrical and Computer Engineering

Feng Xiong, Ph.D., Assistant Professor, Department of Electrical and Computer Engineering

Paul R. Ohodnicki, Ph.D., Associate Professor, Department of Mechanical Engineering and Materials Science

Dissertation Director: Kevin P. Chen, Ph.D., Professor, Department of Electrical and Computer Engineering

Synthesis and Integration of Functional Nanomaterials on Optical Fiber Platforms for Points and Distributed Sensing for Energy Applications

Rongtao Cao, PhD

University of Pittsburgh, 2020

As relatively clean and abundant energy sources, large-scale utilization of natural gas and hydrogen gas fuel for automobile and electricity productions have been considered by many countries as key energy strategies to reduce greenhouse emission and to improve air quality. Methane, the major constituent of natural gas, is an extremely potent greenhouse gas, while hydrogen is highly flammable. The extraction, production, storage, transportation, and combustion of both gas fuels requires extensive deployment of low-cost sensors with sufficient sensitivity to monitor emissions of these gas species throughout energy infrastructure.

Fiber optical sensors, compared with conventional electrical sensors, has been considered effective sensing tools for energy applications due to their resilience to harsh environment, inert for reactive/flammable gases, and immune to electromagnetic fields. A unique trait for fiber optics sensors is their capability to perform distributed measurements along the entire length of optical fibers across great distance using a single fiber. However, optical fiber based on silica materials are insensitive to changes of ambient gas compositions.

This dissertation describes research efforts to synthesize novel functional nanomaterials including rare-earth doped metal oxide nanocomposite, metal organic frameworks doped polymer, nanoscale metal alloy that is sensitive to hydrogen and methane gas from the room temperature to 750 ℃. These functional nanomaterials were integrated with various optical fiber sensors

platforms including both telecom fibers and D-shaped micro-structured fibers. Nanostructure-textured optical fiber was utilized to increase the surface-to-volume ratio of the metal alloy sensory film while dimension and density of the nanostructure was specifically chosen to limit the light scattering. Through on-fiber transaction mechanism such as evanescent interaction and gas-absorption induced on-fiber strain, Rayleigh-based distributed fiber sensors based on optical frequency domain reflectometry and intrinsic Fabry–Perot interferometer were used to measure fuel gas concentration from 0.25% to 40% from room temperature to 750 ℃ with excellent repeatability.

Research works documented in this dissertation shows that highly controllable VLSI microfabrication schemes and novel functional nanomaterials can be used to enhance functionality of optical fibers to produce high performance fiber optical chemical sensors for both distributed and point measurements for both fossil energy and renewable energy applications.

Table of Contents

Preface xv

1.0 Introduction 1

2.0 Sensor Design 10

2.1 Fabrication of Nanostructure-Textured Surface 10

2.1.1 Overview 10

2.1.2 Nanostructure Fabrication on Optical Fiber 12

2.2 Sensory Film Coating on Nanostructures 17

2.2.1 Overview 17

2.2.2 Sensing Film Distribution on Nanostructure-Textured Surface 19

2.3 Metal-Organic Framework Functionalized Polymer 24

2.3.1 Metal-Organic Framework 24

2.3.2 UV-Curable Polymer 26

2.4 Evanescent Wave Absorption 27

2.4.1 Evanescent Wave 27

2.4.2 Evanescent Wave Absorbance 28

2.5 Fabry-Perot Interferometer 30

2.5.1 Principle of Fiber Fabry-Perot Interferometer 30

2.5.2 Fabrication of Fabry-Perot Cavity in Optical Fiber 34

2.6 Rayleigh Optical Frequency Domain Reflectometry 36

2.6.1 Overview 36

2.6.2 OFDR System and Principle 38

3.0 Optical Methane Sensor Based on Metal-Organic Framework Functionalized Polymer Coating..... 44

3.1 Overview..... 44

3.2 Sensory Film Optimization..... 46

3.3 Sensor Fabrication..... 50

3.4 Sensor Characterization..... 53

4.0 Optical Hydrogen Sensor Based on Metal Alloy Functionalized Nanocones..... 63

4.1 Overview..... 63

4.2 Sensory Fabrication..... 66

4.3 Sensory Characterization..... 69

5.0 Optical Sensors Based on Fabry-Perot Interferometer..... 79

5.1 Overview..... 79

5.2 Hydrogen Sensor at Room Temperature..... 81

5.2.1 Sensor Fabrication..... 81

5.2.2 Sensor Characterization..... 83

5.3 Hydrogen Sensor at High Temperature..... 92

5.3.1 Overview..... 92

5.3.2 Sensor Fabrication and Characterization..... 93

5.4 Methane Sensor..... 97

6.0 Fiber Optical Distributed Hydrogen Sensor at High Temperature..... 101

6.1 Overview..... 101

6.2 Sensor Fabrication..... 102

6.3 Sensor Characterization..... 103

7.0 Conclusion and Future Work 107

Bibliography 109

List of Tables

Table 1. The composition of the UV-curable polymer..... 26

List of Figures

Figure 1. Pipeline structure for gas transportation. 2

Figure 2. (a) Schematic and real (inset) image of solid oxide fuel cell, (b) the schematic of underlying principle..... 7

Figure 3. Cross-sectional view of D-shaped fiber..... 12

Figure 4. SEM top-view (left) and cross-sectional view (right) of the etched sample with the etching power of (a) 100 W, (b) 150 W, and (c) 300 W..... 14

Figure 5. Schematic of nanostructure formation. 15

Figure 6. SEM-EDX spectrum of the etched fiber surface. 16

Figure 7. Cross-sectional view of the nanograss on top of the optical fiber with height of (a) 600 nm, (b) 2.5 µm; a(ii) and b(ii) is the enlarged image of the structure. 17

Figure 8. Cross-sectional topography of nanostructure (a) before and (b) after annealing. 20

Figure 9. Top-view (a) and (b) cross-sectional view of the HfO_2 protected nanograss, (c) EDX spectrum of the nanostructure..... 21

Figure 10. The top (left) and cross-sectional (right) view of the sensing film on nanograss with (a) 4 min, (b) 6 min, (c) 7 min, (d) 10 min etching. 23

Figure 11. Schematic of gas absorption process by MOF. 25

Figure 12. SEM image the ZIF-8 MOF..... 25

Figure 13. Schematic image of evanescent wave in optical fiber. 27

Figure 14. Schematic of the intrinsic FPI structure..... 31

Figure 15. Reflected (a) and transmitted spectrum (b) of Airy function. 33

Figure 16. FPI sensor interference spectrum. 33

Figure 17. (a) Schematic of the cavity fabrication by femtosecond laser writing, (b) OFDR spectrum of the enhanced fiber with 1 cavity, inset is the enlarged figure of the enhanced points. 35

Figure 18. Schematic of OFDR system. 39

Figure 19. Chemicals used in the UV-curable polymeric system. 47

Figure 20. (a) Refractive indices of the mixture, (b) viscosity at different temperatures with the increase of ratio of MOFs. 48

Figure 21. Young's modulus (a), and maximum elongation at break (b) of the sensory film with various MOF ratios. 49

Figure 22. (a) SEM image of ZIF-8 MOF, (b) Etched multimode fiber, (c) Cross-sectional view of coated sensor, (d) EDX result of the sensor polymer cladding. 51

Figure 23. Experimental setup. 52

Figure 24. Time-dependent response of sensor in response of methane exposure with various concentrations, inset is the response of the reference sensor without MOFs. 53

Figure 25. Sensor's response to multiple cycles of methane exposure. 55

Figure 26. (a) Sensing speed and normalized power change as a function of different MOF weight ratios, (b) response of the three sensors with different coating thickness. 56

Figure 27. Detection limits of MMF sensor with various sensing length, inset is the response of the sensor exposed to the methane gas with the maximum detectable concentrations. 59

Figure 28. (a) Etched D-shape fiber, (b) Cross-sectional view of the fabricated sensor based on D-shape fiber. 60

Figure 29. Time-dependent response of sensor based on D-shaped fiber. 61

Figure 30. Response of the D-shaped fiber to multiple cycles of methane gas with various gas concentrations. 61

Figure 31. (a) Cross-sectional view of the coated fiber with fiber core being marked by red circle, inset describes the whole sensor manufacturing process, (b) image of the fiber surface, enlarged view is shown in the inset, (c) the distribution of the metal alloy on top of the nanocones by TEM, inset shows the magnified image, (d) top figure shows area selected for EDS mapping, and bottom figure shows the mapping result. 68

Figure 32. Setup for sensor characterization. 69

Figure 33. (a) Response of the sensors with and without nanostructures to various hydrogen concentrations, (b) response speed of those two sensors. Inset shows the sensing profiles of those two sensors upon 4% hydrogen exposure. 72

Figure 34. The response of the sensor to both 10% (a) and 2% (b) hydrogen exposure. 73

Figure 35. (a) Time-dependent response of sensor to repeative cycles of hydrogen with concentration up to 10%, (b) corresponding output light power variations. 75

Figure 36. (a) Response time versus gas concentration when varies the coating thickness of the functional film, the response of sensors with various coating thickness to 4% (inset) and 2%(b) hydrogen gas. 77

Figure 37. Sensory response at elevated temperatures upon hydrogen exposure with various concentrations. 78

Figure 38. (a) OFDR spectrum of the Rayleigh enhanced points in optical fiber, (b) Cross-sectional view of the optical fiber, inset is the enlarged area (red rectangular) of the Pd thin film. 82

Figure 39. Schematic of experimental setup. 83

Figure 40. (a) Interference spectrum of the point sensor, (b) demodulated spectrum of the sensor, (c) time-dependent response of the sensor to various hydrogen concentrations.. 86

Figure 41. (a) Tensile strain ratio in response to gas concentrations in referring to the hydrogen level of 0.25%, inset is fitted curve, and (b) response time of the two cavities upon hydrogen exposure with various concentrations. 88

Figure 42. The time-dependent response of the point sensor to multiple cycles of hydrogen gas with the concentration of 0.5% and 2%. 89

Figure 43. (a) The interference spectrum of the distributed sensor, (b) the demodulated profiler, (c) the time-dependent response, and (d) tensile strain profiler of the multiple sensors to hydrogen gas exposure. 91

Figure 44. (a) Interference pattern of the laser processed cavity, (b) demodulated cavity spectrum, (c) Cross-sectional view of the sensor, inset is the enlarged Pd-TiO_2 film. 94

Figure 45. (a) Time-dependent cavity length and (b) the slope of the cavity length change in response to varied hydrogen gas exposure, (c) response of the sensor to multiple cycles of hydrogen gas of 3%. 96

Figure 46. (a) Characterization of the sensor cavity through OFDR, (b) interference spectrum of the sensor, (c) demodulated cavity spectrum. 98

Figure 47. (a) time-dependent response and (b) cavity length change of the sensor to various methane concentrations, response of the sensor to multiple cycles of methane exposure with concentration of (c) 50% and (d) 100%. 100

Figure 48. Schematic of experimental setup. 103

Figure 49. (a) Top view of sensor, inset is the enlarged image, (b) cross-sectional view of the sensor. 103

Figure 50. Distributed response of the sensor to various hydrogen concentrations. 104

Figure 51. Distributed response of the sensor to (a) 4% hydrogen and (b) 1% hydrogen, nitrogen resetting process after the hydrogen exposure of (c) 10% and (d) 1%. 105

Figure 52. Response of sensor to various hydrogen concentrations at (a) 750 ℃, (b) 700 ℃, (c) 600 ℃, (d) 500 ℃ 106

Preface

The journey of pursuing PhD has been one of the most exciting and challenging experience in my life. Without generous support and guidance from many great people, none of the work accomplished in the dissertation would be possible.

First and foremost, I would like to thank my advisor Dr. Kevin P. Chen for his significant contributions of insightful ideas and guidance to my PhD study. I also appreciate Dr. Chen for his efforts of creating an open-minded lab environment so that various ideas can be fully expressed, exchanged, and discussed, which helps to cultivate significant collaboration in the lab.

Many thanks to Dr. Guangyong Li, Dr. Susheng Tan, Dr. Feng Xiong, and Dr. Paul R. Ohodnicki for their time and advice as the committee member.

I would also acknowledge the collaborates: Dr. Paul Ohodnicki，Dr. Ki-Jong Kim, Dr. Hangjun Ding, Dr. Guanquan Liang, and Yang Yang for their support and suggestions.

The members of our group have also inspired me both professionally and personally, which deserved to be acknowledged: Dr. Rongzhang Chen, Dr. Aidong Yan, Dr. Shuo Li, Dr. Sheng Huang, Dr. Mohamed Zaghloul, Ran Zou, Mohan Wang, Zhaoqiang Peng, Jingyu Wu, and Xinruo Yi.

Lastly, I would also like to say a heartfelt thank you to my family for always loving, supporting, and believing in me.

1.0 Introduction

Petroleum and coal have been the dominated energy source for more than half a century and increasing consumption of those materials introduces tremendous ongoing environmental, health, and economic problems. The demand for vast deployment of clean energy with less pollution and lower greenhouse emission gradually acknowledged worldwide as a common interest in economy development. Abundant as the fossil fuel, natural gas now ranks as the second largest consumed energy source in the United States with affordable price, accounting for more than 1/3 of total energy consumption. In recent decades, a large number of infrastructures for natural gas harvest, storage, transportation has been built for both energy generation and chemical synthesis.

Methane gas (CH_4), known as the major constituents of natural gas, also contributes to global warming as potent greenhouse gas. The large-scale extraction and utilization of the methane gas impose significant challenges on gas leakage detection, which is further exacerbated by the aging issue of infrastructures, for instance, the high-pressure pipeline (figure 1) requires extensive gas monitoring system utilizing low-cost gas sensors at every stage of the applications. Electrical gas sensors had already been widely investigated, mostly as point sensing schemes with high sensitivity and rapid response. However, the recent development of energy industry requires the sensor to operate under more complex environmental conditions with upscaled functionality including longer-distance sensing, real-time and distributed monitoring, high-temperature and electromagnetic resilience, most of those are far beyond the limits of current electrical sensor. Moreover, the existing sensing practices utilize abrupt temperature variation as the indicator at the

localized leakage points, which is only applicable to incident with severe leakage, and the gradual gas leak and degradation of the pipeline structural health, instead, cannot be effectively monitored.

Fiber optics, initially utilized in telecommunication industry for the distinguished properties of large bandwidths and low loss, have drawn increasing attention recently for chemical sensing schemes. Unlike the electrical counterpart, most of the optical fibers is made of silicon dioxide with light doping, allowing it to be fully functional even under high temperature up to 1000 ℃. Besides, the small form factor (< 200 μm) and flexibility of the optical fiber facilitate its accessibility for applications with serious limitation of spacing, for instance, the applications of structural health monitoring. Meanwhile, the low attenuation loss during light transition in optical fiber has also been considered as an overwhelming advantage for the development of remote and distributed sensing applications.

Figure 1. Pipeline structure for gas transportation.

In addition, optical fiber provides another significant merit for pipeline leakage monitoring: the multi-parameter measurement. The detection of single physical condition along the pipeline

such as temperature usually compromised by other parameters including the applied strain. Based on different light scattering phenomenal within the optical fibers (Rayleigh, Brillouin, and Raman), optical fiber can be utilized for real-time, multi-parameter and distributed measurement including direct measurement of methane gas concentrations across long interrogation distance. One challenge of utilizing optical fiber for sensing purpose is its inert nature since most of the commercialized fiber is made from glass or even sapphire crystal. Meanwhile, the incident light is also well-confined in the small fiber core, limiting its interaction with chemicals in the surrounding environment. To address this issue, optical fiber needs to be engineered. The typically approach is to utilize evanescent wave interaction and interferometers.

Most of the optical methane sensors is based on evanescent light coupling and absorption by functional coating materials that the light properties including its intensity, wavelength, and polarization have been tuned as a result of gas interaction with sensory materials. Semiconductor materials such as SnO_2 thin film [1] and graphene [2] have been widely reported in gas sensing applications. However, those sensors are not the ideal candidates for long-distance gas monitoring scenarios due to multiple reasons, for example, the tremendous loss introduced by large refractive index mismatch between SnO_2 and fiber core prevents it from long-distance usages. Meanwhile, the high cost of semiconductor materials such as the graphene also causes the economic problems for large scalable deployment. Moreover, the proper packaging of those sensors for harsh environmental usage without jeopardizing its sensitivity and stability still remains an issue.

To address those challenges, we functionalized polymeric material with metal-organic framework (MOF) and coated it on the pre-etched multimode optical fiber as the new fiber cladding. The coated sensing film was further cured under the UV lamp to form a rigid polymer coating. MOF has been specifically engineered to physically capture the methane molecules. The

refractive index of the MOF-Polymer mixtured film was further optimized by adjusting its weight ratio to minimize the refractive index mismatch between polymeric cladding and fiber core. The optimization and characterization of the optical methane sensor were presented in chapter 3. High detection limit and good repeatability of the sensor were achieved. The underlying principle of this sensor is based on the refractive index mismatch variations upon methane absorption that determines the light coupling and transmitted light intensity. The polymer cladding serves as the sensing film and the protecting coating of the sensor as well in this case. The same coating was further applied to D-shaped single mode fiber, a very similar response was obtained, which indicates the universal of this method across different fiber platforms. Moreover, UV curing process of the functional material on top of the optical fiber is also compatible with existing fiber drawing process, making the large-scale fabrication of this device possible.

Clean energy such as hydrogen gas has also been considered as a great candidate in reshaping the current energy form towards zero emission and it has been utilized in a wide range of applications including the electricity generation for power grids, fuel cell-based vehicles, security equipment, and fertilizer synthesis. A total production of 10 million metric tons of hydrogen gas was reported per year in the United State, most of which is utilized in the energy industry. The hydrogen production line is scattered in almost every state and more than 1000 miles of pipeline was specially built for the gas delivery across the whole nation. Meanwhile, a large number of corresponding infrastructures was also deployed for gas production and storage. The large-scale deployment of hydrogen gas facilities requires close monitoring of gas leakage due to its low flammable point, demanding the sensor to be highly functional in terms of the response speed and sensitivity.

The low ignition energy of the hydrogen gas introduces safety concerns when utilizing electrical sensor for gas monitoring due to the generation of sparks. Sensors based optical fiber can provide an alternative solution. Most of the existing optical sensor is functionalized by pure Palladium coating due to its large hydrogen solubility. However, the sensor suffers from slow phase transitions from α-PdH to β-PdH when exposed to hydrogen gas with concentrations ranging from 0.1 to 2%, limiting its response speed. Moreover, it also undergoes the signal saturation issue when the gas concentration is increased to 3%.

In this dissertation, we presented our work of developing fiber optic hydrogen sensor with the response time being shortened by 3-4 times on average in chapter 4. Nanostructure-textured optical fiber was utilized as the foundation of the sensor followed by the palladium (Pd) alloy thin film coating through vacuum chemical deposition. The working principle of the sensor is based on the evanescent wave absorption. Nanostructures fabricated on the optical fiber through VLSI microfabrication schemes help to reduce the refractive indices mismatch between the sensory film and fiber core, effectively mitigates the coupling loss of the sensor. Meanwhile, the enlarged surface-to-volume ratio in combination with the alleviated internal stress of the sensory film dramatically improves the sensor behavior in terms of the response speed, reversibility, and stability upon hydrogen exposure with various concentrations, providing an easy solution of fast hydrogen sensing for energy usages.

In addition to point sensing applications, sensors with distributed measurement capability is also crucial for infrastructure monitoring. For instance, the large-scale hydrogen pipelines require significant amount of point sensors for the comprehensive understanding of whole pipeline structural health status, which dramatically increases the cost of the whole project. Optical fiber has already been deployed in the structural health monitoring in the past decades to measure the

physical parameters such as the temperature or stress, demonstrating reduced sensing cost and improved resolutions. However, few chemical sensors especially hydrogen sensor have been reported with the distributed and real-time monitoring capability.

In chapter 5, a distributed optical sensor was developed utilizing Fabry-Perot interference metrology to monitor the hydrogen gas distributions at room temperature. The sensing cavities were formed by two highly reflected Rayleigh scattering point inscribed through ultrafast laser irradiation, and their distance ranges from several hundred micrometer to around 1 millimeter. Multiple cavities were introduced to the fiber core with specific separation distance followed by functional coating. The interaction between functional materials and the targeted gas generates a tensile strain and transfers to the optical fiber, expanding the length of sensing cavities in nanometer scales. The tensile strain is proportional to gas concentrations and can be utilized as an indicator of the gas levels. In this dissertation, we reported the deployment of optical sensor with 7 sensing cavities for hydrogen monitoring, delivering a distributed sensor with detection limits of 1% and spatial resolution of 5-mm.

In addition to basic infrastructures, hydrogen gas has also been utilized for the generation of energy forms such as electricity. The most commonly deployed scheme is the solid oxide fuel cells, which is a high-efficiency and versatile energy production device and being utilized for the automobiles and electric power production. A typical schematic of the solid oxide fuel cell is shown in the figure 2(a) with the real image shown in the inset, in which there is very limited space for the implement of traditional sensors. The transformation of hydrogen gas into useable energy momentum usually involves the combusting process, which, in most cases, operates at extreme high temperatures. The fuel cell works at temperature over 700 ℃, which is very challenging for the electrical sensor to survive.

Meanwhile, the hydrogen gradient is generated at the anode of the fuel cell due to gas consumption as observed in the figure 2(b), generating a temperature variation inside the fuel cell assembly. The internal temperature variation is detrimental to the fuel cell material and structural health of the device by introducing thermal stress, degrading its lifetime. Moreover, the non-uniformity distribution of the hydrogen gas along the anode also reduces the energy conversion efficiency and fuel consumption profile, further deteriorates the performance. Therefore, the accurate monitoring of the gas distribution along the anode is very crucial for the comprehensive understanding of fuel cell behavior in order to improve the long-term performance and economic viability of the solid oxide fuel cell.

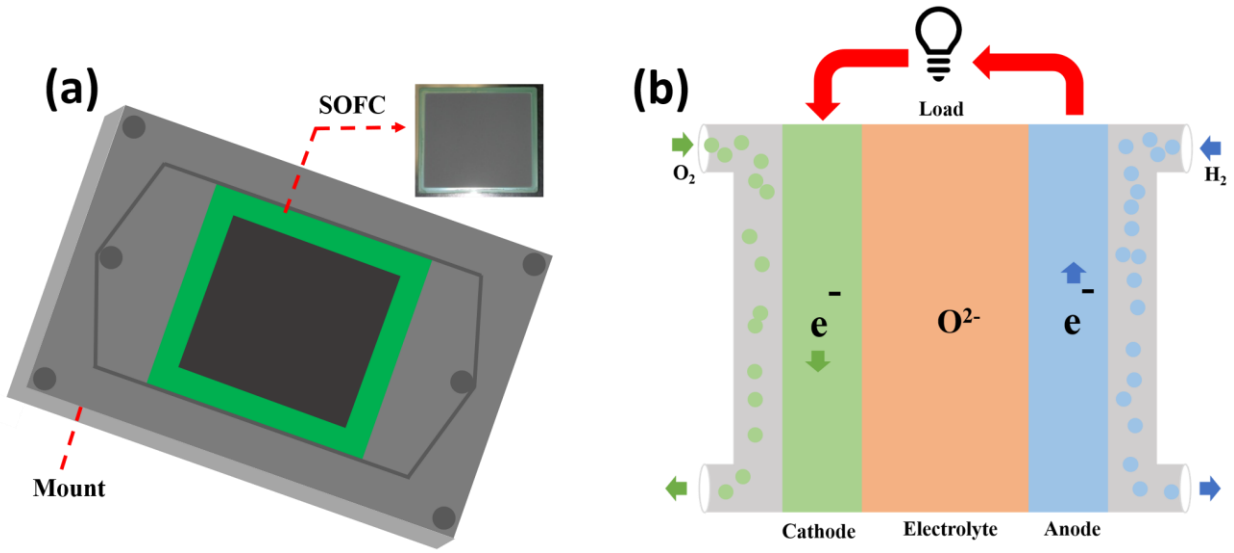

Figure 2. (a) Schematic and real (inset) image of solid oxide fuel cell, (b) the schematic of underlying principle.

In chapter 5, we address this issue by combining Pd-doped nanocomposite metal oxide with intrinsic Fabry-Perot interferometer. The sensor operated at 750 ℃ and the expansion of functional coating generates a tensile strain and transfer onto optical fiber, which serves as the fundamental principle of this sensor. Unlike sensor operating at room temperature, the cavity

length of this sensor continuously increases as long as it is exposed to hydrogen gas, indicating an unbalanced tensile strain by the shear force of the fiber. However, the slope of cavity length variation is quite repeatable and can be utilized as the indicator for the gas levels. With the implementation of a series of cavities, a multipixel sensor can be manufactured for multi-point as well as multiple parameters monitoring including both gas concentration and local temperature to fully understand the operational status of solid oxide fuel cell.

Followed by the above efforts, another intrinsic Fabry-Perot sensor was developed based on polymeric functional coating. The polymeric coating and the measurement scheme are the same as described in the chapter 3. The sensor demonstrates a responsive behavior as the cavity length increases upon methane gas exposure with the detectable gas concentration of 40% at room temperature. The low detection limit is associated with the small Young's modulus that cannot effectively produce and transfer reasonable amount of tensile strain to the optical fiber. The reversibility and repeatability of the sensor, however, were confirmed in the experiment for the fully investigation of the sensor behavior.

Though hydrogen sensor with a high spatial resolution of 5-mm was developed in our experiment through Fabry-Perot interferometer, a truly distributed measurement with concept of monitoring each and every localized event occurring within specific range is still worth investigating. Optical time domain reflectometry based on the Brillouin scattering is initially developed to address this requisition. However, there occurs a tradeoff between the spatial resolution and the dynamic range in this approach, limiting its implementations for application with very localized events.

In chapter 6, optical frequency domain reflectometry (OFDR) based on elastic Rayleigh-scattering were adopted for the distributed hydrogen measurement at high temperature. The

monitoring of the localized events is performed by measuring the intensity of Rayleigh backscattered signal, in which, the OFDR system actually maps the spatial distance into frequency domain. The OFDR system demonstrates a high spatial resolution of 10 μm with dynamic range of 2 Km. When utilized for temperature and strain measurement along the optical fiber, OFDR can also perform a very high resolution of 0.1 ℃ and 1με, respectively, while the optical fiber is treated as a series of fiber Bragg gratings. In this experiment, Pd doped TiO_2 thin film prepared through sol-gel process was coated on the fiber. The significant light absorption variations of the functional coating introduced by the electron transferring process upon hydrogen exposure generates a corresponding Rayleigh backscattering signal fluctuation, serving as the indicator for the gas levels along the fiber. Nanostructure-textured optical fiber was also utilized in the experiment to prevent the collapse of sensory film at high temperature that jeopardizes the sensor performance. Meanwhile, the large surface-to-volume ratio of the functional coating introduced by the nanostructures also yields more significant response of the sensor. The Pd concentration in the sensory film was also adjusted to further optimize the sensor.

2.0 Sensor Design

To utilize optical fiber as the sensing platform, the inertness of glass fiber needs to be modified in order to introduce variations of light property when exposed to the environmental variations or targeted chemicals. Multiple approaches have been adopted by the researchers to functionalize optical fiber for sensing purpose, for example, the utilization of functional coating, structural modification of optical fiber, and the introduction of interferometers. In this chapter, a detailed discussion of those approaches utilized in our works for the sensor designing including the utilization of textured fiber, metal-organic framework-based functional materials, Fabry-Perot interferometer, and optical frequency domain reflectometry will be covered.

2.1 Fabrication of Nanostructure-Textured Surface

2.1.1 Overview

The development of nanotechnology especially nanostructures has promoted the emergence of new devices with exceptional properties such as solar cell [3, 4] and light emitting diodes [5-7]. Nanostructures have also been considered as great candidate to improve the performance of chemical sensing, which has already been utilized in various sensors in recent decades, for example, plasmonic sensors for bio-chemical sensing [8], gas sensor functionalized by nanostructured oxide [9, 10] and noble metal [11].

To utilize nanostructures in the device, one of the major issues needs to be addressed is its fabrication process. Various approaches have been developed to manufacture nanostructure with customized dimensions and spacings. The most well-established method is photolithography, which consists multiple steps including photoresistor coating, UV light exposure, and pattern developing process. Although photolithography provides the most sophisticated tool for nanoarray fabrication, it has the most restrict requirement for the substrates among all the approaches. Meanwhile, feature dimension is also limited by the diffraction of the UV light and cannot be scaled down to the size within light wavelength. To overcome those limitations, e-beam lithography was invented, in which, the exposure of the photoresistor is fulfilled utilizing the electron beam instead of UV light. However, this process has the limitation for large-scale applications since it is a point-by-point process that the slow writing speed cannot be overcome. A recent approach capable of rapid developing is the nanoimprint, which transfers the nanostructure pattern from designed mask to a polymer film on top of the target substrate. Nonetheless, the design of three-dimensional mask and thermal mismatch between polymer and inorganic substrate remain an issue for the further development of this technology. Another solution is to utilize masking layer as sacrifice layer followed by the plasma or wet etching to form the nanostructures on top of the substrate. The commonly used mask is the nanoscale metal particle created by thermal annealing of the thin metal film [12, 13]. Self-assemble polymer sphere mask has also been investigated [14]. However, the complicated process also prevents this technology from mass production. Recently, self-masking process has been reported on fused silica and customized glass which involves a single step of reactive ion etching (RIE), significantly simplifies the whole manufacturing process as well as dramatically reduced the cost [15, 16]. Herein, we will present our work of fabricating nanostructures on top of optical fiber through maskless etching

process. The processing time and power were also optimized to form different types of nanostructures during the experiment. Detailed explanation of the underlying mechanism will also be presented.

2.1.2 Nanostructure Fabrication on Optical Fiber

D-shaped fiber utilized in the experient was specially made by Corning Inc. The fiber consists of a rounded core with diameter of 8.5 μm (outlined red circle). The distance between core center to upper flat cladding surface is 8 μm as shown in figure 3. The fiber was first cleaned thoroughly in solvent using acetone and methanol followed by dionized water rinse and air drying process. The cleaned D-shaped fiber was further attached onto a silica glass wafer as rounded cladding surface facing downwards. The sample was then transfered into a RIE system (Phantom). The etching process was carried out by mixed gas of SF_6 (10 sccm), CHF_3 (40 sccm), and inert Ar (80 sccm). The radio frequency power of the process was varied from 100 W to 300 W while the chamber pressure and etching time were fixed to 200 mT and 45 min, respectively.

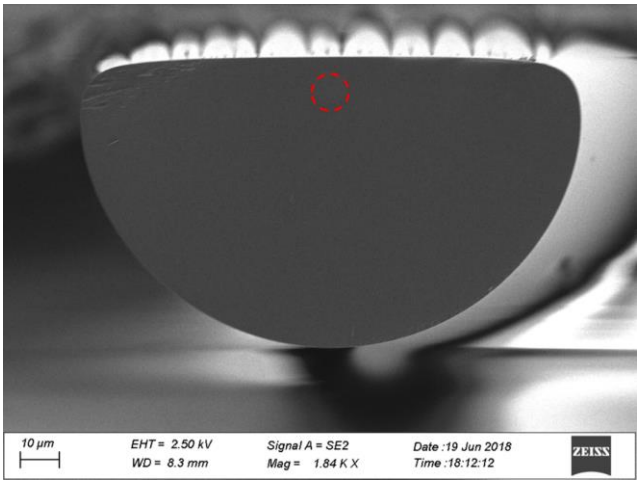

Figure 3. Cross-sectional view of D-shaped fiber.

To evaluate the surface and cross-sectional morphology after plasma etching, scanning electron microscopy (SEM) from Zeiss (Sigma 500VP) with an optimized accelerating voltage of 3 KV was employed. A thin layer of PdAu alloy was pre-deposited onto the sample surface by the sputter coater (Hummer) before imaging to avoid the electron accumulation for better resolution, and results are shown in figure 4.

Small nanocones were formed on top of the fiber surface under lower RIE power of 100 W as shown in figure 4(a). The densely-pack nanocones has the dimension of 50-nm and height around 70-nm. The average spacing between nanocones are about 30 nm. Once increasing the radio frequency power to 150 W, a mixture of nanograss and nanocone was formed as a result. The nanograss in figure 4(b) is randomly distributed on the fiber surface with no obvious pattern. The nanocone structures were totally replaced by the nanograss when exposed to the plasma with the maximum power of 300 W. The height of nanograss was about 2 μm and separating distance between nanograss increased to about 500 nm. By controlling the input plasma power and related processing time, we can customize different types of nanostructures on top of the fiber surface with various height.

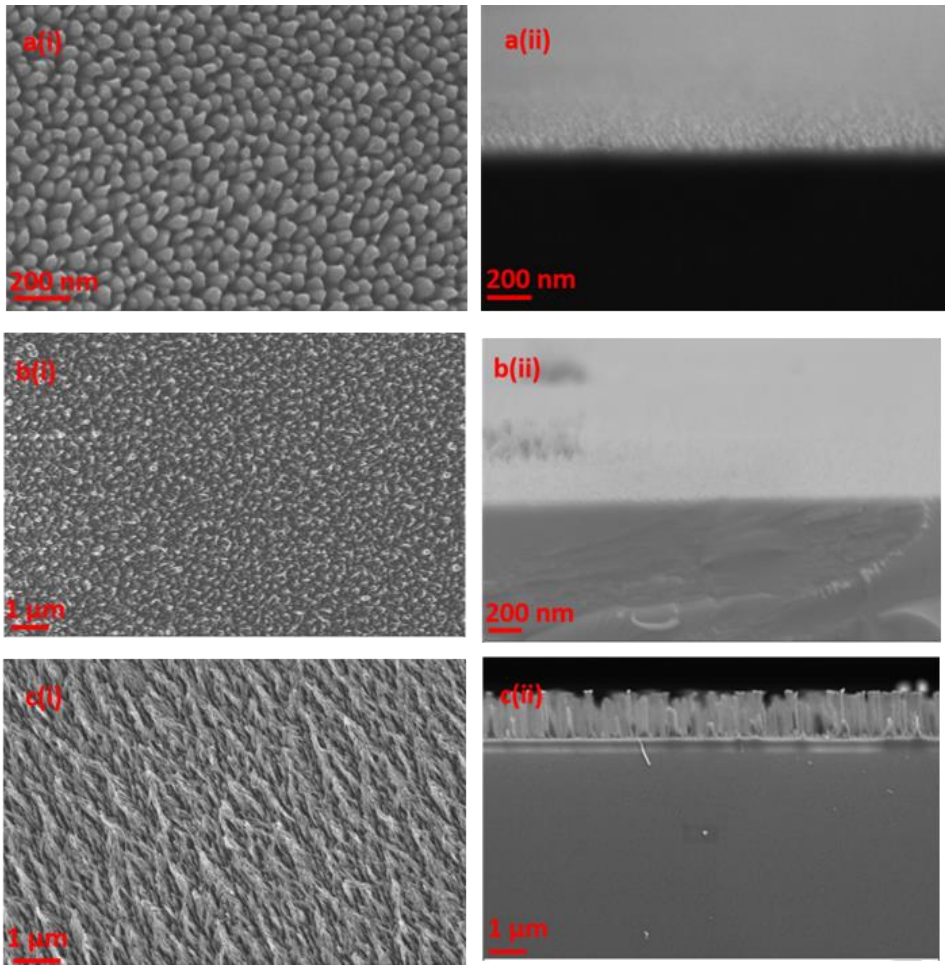

Figure 4. SEM top-view (left) and cross-sectional view (right) of the etched sample with the etching power of (a) 100 W, (b) 150 W, and (c) 300 W.

The underlying principle of nanostructure formation upon plasma etching can be explained in figure 5. The initial irradiation of the optical fiber by fluorine plasma generates carbon-fluorine based polymer byproducts on top of the fiber surface, which serves as the masking layer and preventing the further etching [15, 16], and the other areas without polymer coverage were etched away instead. As the polymer was gradually consumed during the etching process, cone structures formed as a result.

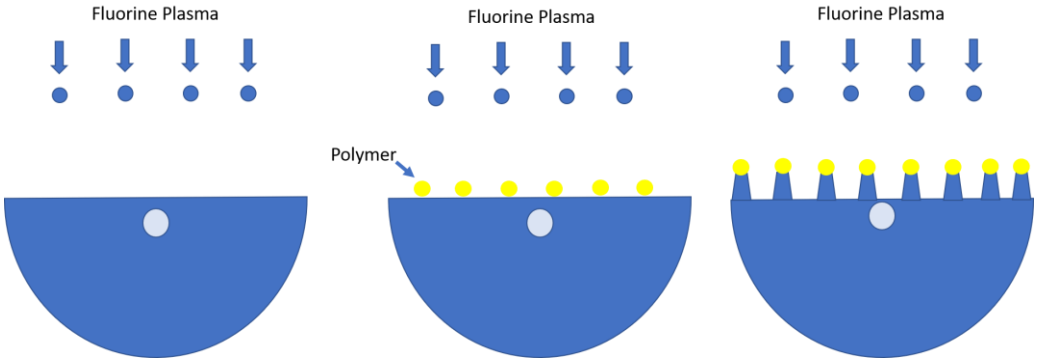

Figure 5. Schematic of nanostructure formation.

The chemical composition of the etched surface was studied to better understand the process by performing the energy-dispersive X-ray (EDX) analysis. The measurement was fulfilled with detectors equipped in Zeiss system and the result is shown in figure 6.

Fluorine and carbon element line were detected in the EDX spectrum, indicating the existence of the polymer byproducts on top of the optical fiber after etching. Meanwhile, pallidum and gold alloy introduced by the chemical evaporation deposition were also confirmed in the spectrum.

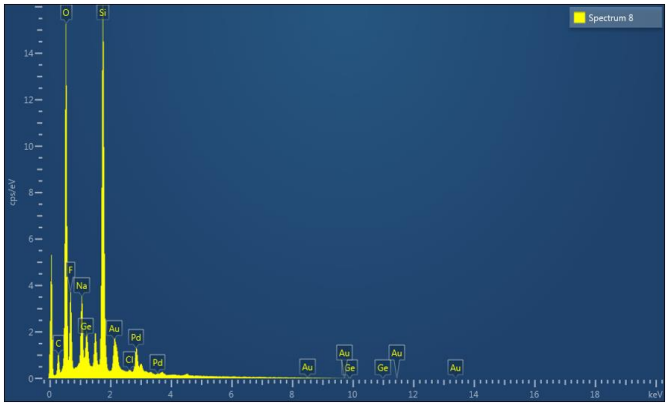

Figure 6. SEM-EDX spectrum of the etched fiber surface.

The method discussed above provides an effective approach which is also compatible with current VLSI manufacturing schemes in fabricating nanostructures on top of optical fiber. The nanocone structures were utilized in the chapter 4 as the textured-surface to improve the sensory response of hydrogen gas at room temperature. In addition to small nanocones, the nanograss structure with proper dimension can be used to engineer the refractive index of the functional coating materials for chemical sensing, for example the palladium-doped metal oxide for hydrogen gas sensing at high temperature. However, the large separating distance of nanograss fabricated through above approach could be problematic. To address this issue, we adjusted the RIE gas composition by replacing CHF_4 with O_2 during the etching process without changing other parameters. The oxygen flow was fixed at 5 sccm, and the resulted structural topography of optical fiber are shown in the figure 7.

As compared with the structures in figure 4(c), a more uniform nanograss array was achieved on top of fiber surface when oxygen was introduced into the reactive chamber. Meanwhile, the distance between nanograss shrunk from 500 nm to around 200 nm. The height of the nanograss can also be easily adjusted from around 100 nm to a few micrometers by simply controlling the etching time. These nanograss structures was utilized as the textured fiber surface

in the experiment followed by the functionalized material coating to increase the surface-to-volume ratio of the sensory film for improved hydrogen gas sensing at high temperature of 750 ℃ in chapter 6.

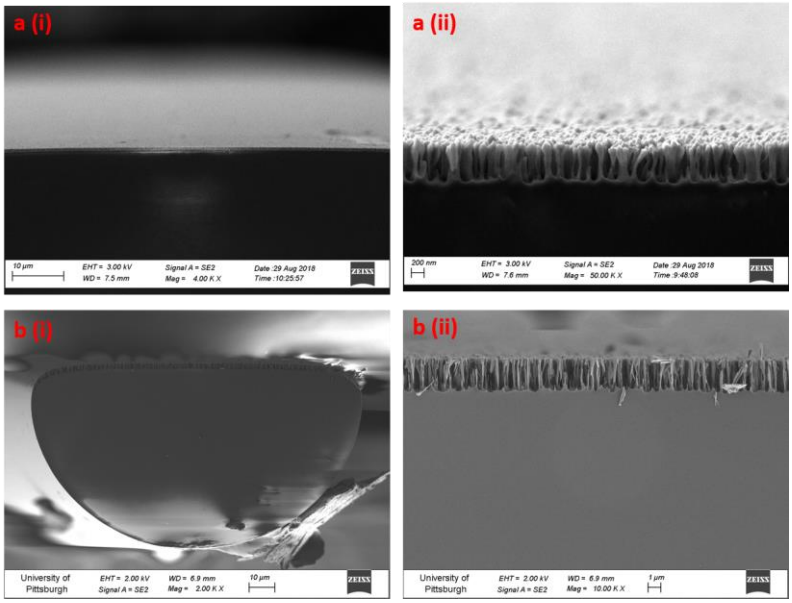

Figure 7. Cross-sectional view of the nanograss on top of the optical fiber with height of (a) 600 nm, (b) 2.5 μm; a(ii) and b(ii) is the enlarged image of the structure.

2.2 Sensory Film Coating on Nanostructures

2.2.1 Overview

The demand for reliable, compact, and low-cost chemical sensors, particularly gas sensor, is continuously increasing due to the large deployment of energy industry such as natural gas and clean energy. The complex environmental conditions require the sensor to behave in a more significant manner with quick response. The sensitivity and response speed of the sensor are

mainly associated with extent of the light interaction with sensory materials on top of the fiber, which is determined by the refractive index and light absorption coefficient of sensing materials. The conductometric semiconducting metal oxide are one of the most investigated functional materials for chemical detection due to its distinguished merits of large-scale capability, high efficiency, and low cost. The commonly used metal oxide is NiO, TiO_2, Fe_3O_3, Ta_2O_5, and Cr_2O_3. The conductivity change of the metal oxide film introduced by the trapped electrons upon molecules absorption are considered to be the underlying principle in the process [17]. The variation of material conductivity in response to the gas exposure is mainly affected by the catalytic reactions. The pure semiconductor oxide was proved to be very inefficient in chemical response at high temperature due to the lack of catalyst [18]. The problem can be solved by introducing noble metal into the oxide as the dopant. Nobel metal such as Pd and Pt are oxidation catalyst with high efficiency in electron transferring. Multiple approaches had been adopted in incorporating noble metal into semiconductor materials, for example, sol-gel, sputtering, and thermal evaporation [19]. The approach involved in our experiment was solution-based sol-gel process. Palladium chloride was introduced as the Pd source and mixed with titanium isopropoxide to form a Pd doped TiO_2 sol-gel solution and being applied on the optical fiber as the functional coating. The detailed preparation process of sensory material can be referred to the previous literatures [20, 21].

Nano-scaled porous sensory film were fabricated through polymer calcination at high temperature [20]. Porous structures were introduced in this work to tune the effective refractive indices mismatch between the sensory film and the fiber core so that the light coupling to functional cladding is optimized in terms of the attenuation loss for long-distance applications. However, the porous nanostructure cannot survive under high temperatures and will collapse in

the end, limiting the stability and repeatability of the related sensors for harsh environmental usage such as the fuel cells. Nanostructure-textured optical fiber surface discussed in the previous section could be utilized to engineer the effective refractive index of sensory material with exceptional resilience at high temperature around 1200 ℃. A good understanding of the sensory film distribution on top of the textured surface could be very beneficial for sensor optimization.

2.2.2 Sensing Film Distribution on Nanostructure-Textured Surface

The stability of the nanostructures at high temperature was investigated by introducing the annealing process at 750 ℃, and the results are shown in the figure 8. A dramatic reduction of the nanograss dimension was confirmed in figure 8(b). The densely-packed nanograss array disappeared and turned into sparsely-separated shadow wavy pattern with the average structural height around 70 nm. The underlying mechanism is still unclear right now and further investigation is needed to explain this phenomenon. However, the dramatic topographic change of the fiber optics surface at high temperature could be problematic for fiber optical gas sensor since the tuning capability of refractive indices and corresponding light couplings of the metal oxide film was significantly jeopardized.

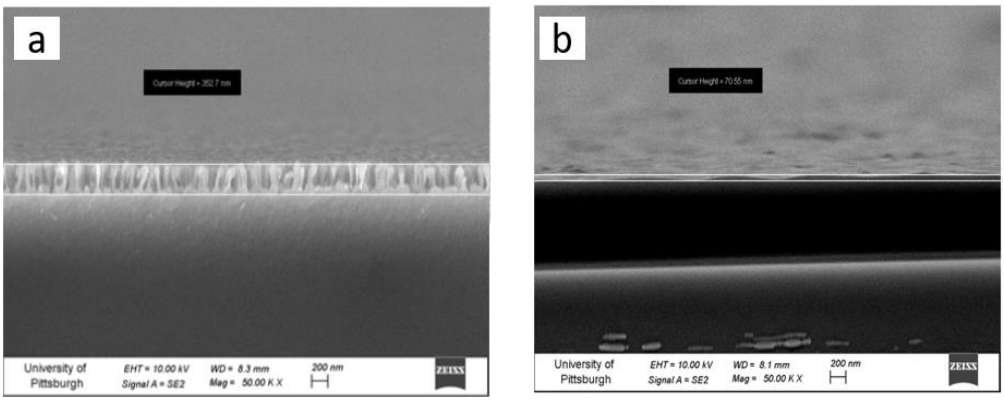

Figure 8. Cross-sectional topography of nanostructure (a) before and (b) after annealing.

To address this issue, HfO_2 thin film was deposited on top of the nanostructure-textured fiber surface as a protecting layer by plasma enhanced atomic layer deposition (PE-ALD) process. The thickness of the HfO_2 film was chosen to be 5-nm with 35 cycles of ALD to avoid the tremendous coupling loss between the fiber core and thick coating films. The sample was then inserted into a furnace and annealed at 800 ℃ for 1 h, and the topography and chemical composition of the structures were characterized by SEM and EDX, respectively, and the results are shown in the figure 9. From figure 9(a) and (b), it is easy to notice that no apparent surface topography variation of the etched fiber surface was observed in terms of the nanograss height and density with HfO_2 protection layer when compared with samples without protection in figure 8, which confirms the functionality of HfO_2 film in protecting the nanostructures from high temperature. The EDX spectrum of the sample was also illustrated in the figure 9(c). A significant amount of Hf element was detected in the sample, which was mainly resulted from the limited penetration depth of the accelerated electrons during the measurement that prevented it from gathering chemical information beneath the fiber surface.

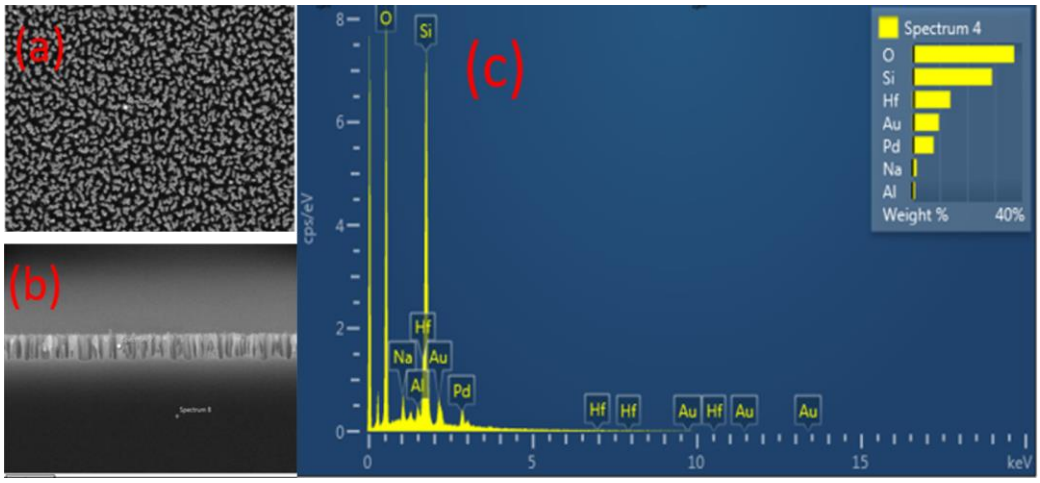

Figure 9. Top-view (a) and (b) cross-sectional view of the HfO_2 protected nanograss, (c) EDX spectrum of the nanostructure.

Once the stability issue of the nanostructures at high temperature is resolved, it is also crucial to investigate the distribution of sensory film on top of the nanostructure-textured fiber surface. Functional coating solution was prepared through sol-gel approach by adding palladium chloride ($PdCl_2$) dopant into titanium isopropoxide ($Ti(OCH(CH_3)_2)_4$) to form the functional mixture [21]. Nanostructure-textured optical fiber was fabricated by RIE etching with processing time of 4, 6, 7, and 10 min respectively. The processed fiber sample was further protected by the HfO_2 thin film through chemical deposition. The sensing film was formed on top of the fiber through drop-coating method at room temperature and dry in air for 12 hours for the hydrolyzing process. The coated sample was then annealed at 750 ℃ for 1 h, and the topography of the sensory film distribution is shown in figure 10.

A smooth and continuous film surface was observed in figure 10(a) and (b) when the dimension of fabricated nanograss is less than 200 nm. Samples with longer etching time appears to have more cracks after annealing, which can be explained by the separating gaps in those cases. When the dimension of nanograss is relatively small, the separating distance between

nanostructures are very tight, which traps less moisture during coating process as compared with sample of large nanograss dimension. Once sample is exposed to high temperature, the trapped moisture undergoes expansion and evaporation process, creating voids in the sensory film.

Another possible reason might be associated with the thermal expansion coefficient mismatch between the sensory film and nanostructures. When sensory film was coated on top of fiber surface covered by large nanostructures, a relative thin and continuous layer of sensory film was formed compared with thick layer of sensory film on top of the small nanostructures as shown in figure 10(d). The increasing temperature introduced the accumulated internal stress mismatch between sensory film and the nanostructure on top of the fiber surface, which could be released through the formation of cracks. The small internal stress of the sample with short nanostructure required relative short cracks to fully release while the thick continuously sensory film provided enough space for the formation of crack, preventing the propagation of cracking onto top surface of sensory film. However, in terms of the sample with large nanostructures, the relatively large internal stress mismatch needs to be released through longer cracks, which, as a result, propagates onto the fiber surface. However, compared with sample covered by small nanograss, the wider gaps between large nanostructures allow deeper penetration of the sensory film, producing a more effective refractive index tuning.

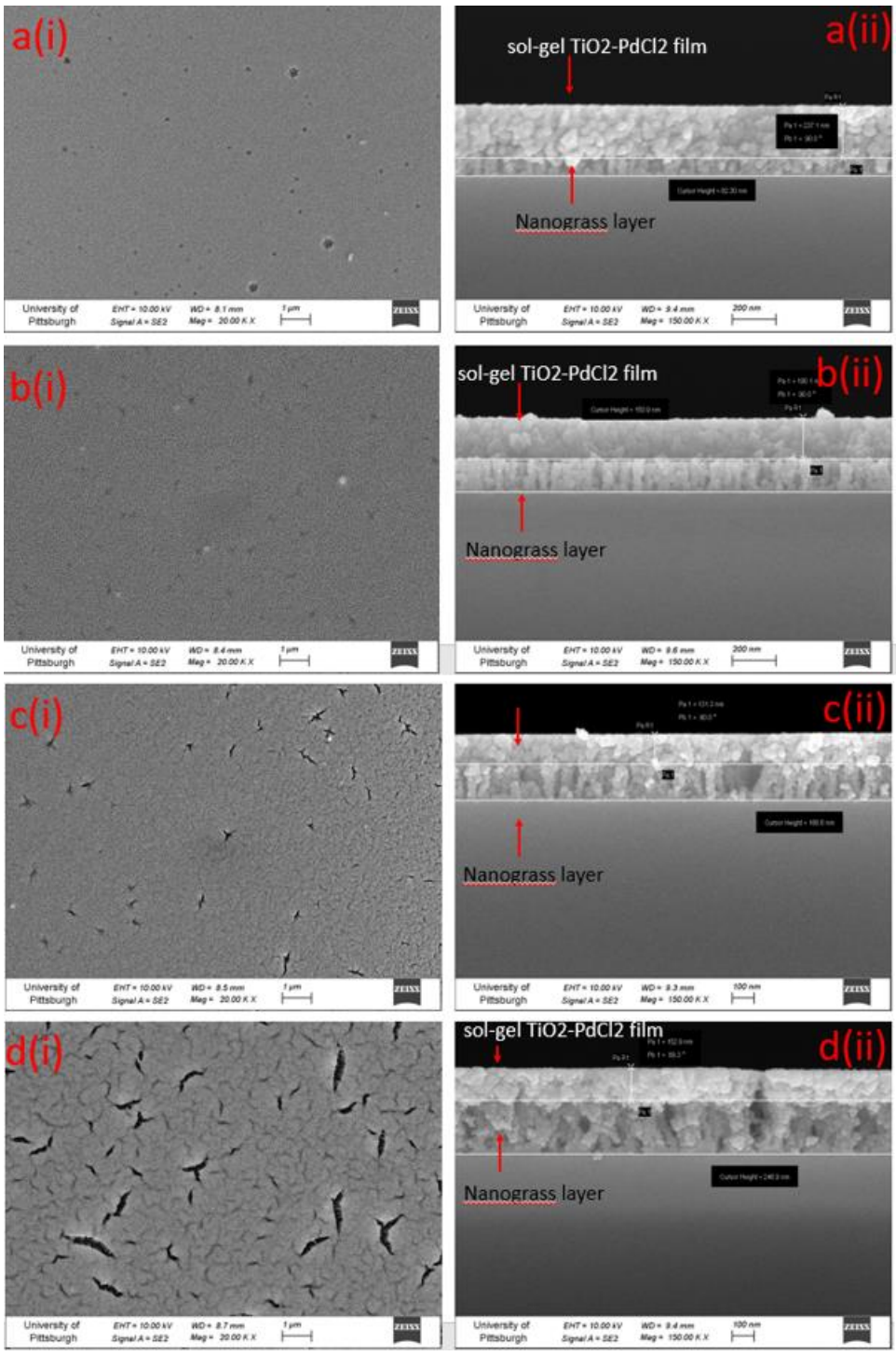

Figure 10. The top (left) and cross-sectional (right) view of the sensing film on nanograss with (a) 4 min, (b) 6 min, (c) 7 min, (d) 10 min etching.

2.3 Metal-Organic Framework Functionalized Polymer

2.3.1 Metal-Organic Framework

Natural gas, compared with fossil fuel, generates less greenhouse byproducts due to the high hydrogen carbon ratio, and has been deployed in the automobile industry to replace the combustion engine. One fundamental issue remains before the extensive implementation of the natural gas industry is high-volume gas storage at room temperature within the moderate pressure. Metal-organic framework (MOF), benefiting from its large pore-spacing and extended surface area, has been considered as a great candidate in gas storage applications.

MOF is a multidimensional structure which consists of organic ligands correlated with metal ions or clusters. Nowadays, MOF has been intensively investigated as a new porous material [22]. One of most commonly investigated MOF is three-dimensional based framework with the geometry of crystals. Meanwhile, a large number of potential organic linkers in combination with various metal ions leads to a wide variety of porous materials with distinguished surface and chemical properties specialized for different types of gas storage. Typically, the interaction between the gas molecules and MOF crystals are based on physical absorption process induced by dispersive and repulsive process [23] as shown schematically in figure 11 where the gas molecules are being trapped in the cages of the crystals. There are also other circumstances that the gas molecules were captured and attached outside the MOF cage structures depending on the types of the metal ions and organic ligands.

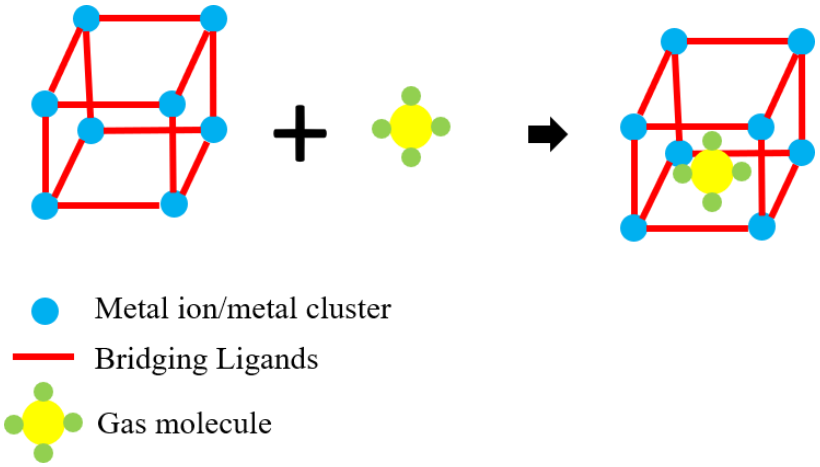

Figure 11. Schematic of gas absorption process by MOF.

The MOF used in our work is ZIF-8 (2-methylimidazole zinc) MOF synthesized by the National Energy Technology Laboratory [24]. The MOF and methanol mixed solution was drop coated on top of silicon wafer and the topography of the structure was characterized by SEM. The MOF appears to be cubic geometry with dimension ranging from 66 to 100 nm as shown in figure 12.

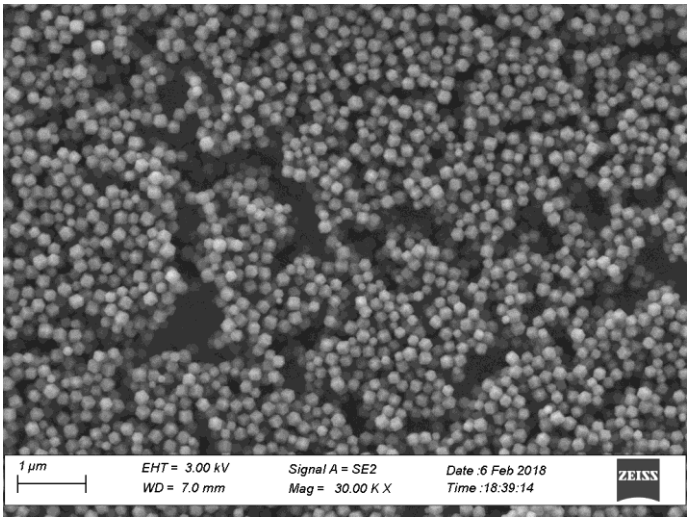

Figure 12. SEM image the ZIF-8 MOF.

2.3.2 UV-Curable Polymer

The most common approach to fabricate MOF-based fiber optical sensor is through layer-by-layer in-situ deposition process. The complicated fabrication process dramatically increases the cost of the optical sensor, which prevents it from large-scale applications including the gas pipeline monitoring. To overcome this issue, UV-curable polymer was introduced to provide a matrix for the MOF crystal to disperse, and the mixture solution could act as the functional coating.

Poly (dimethylsiloxane) (PDMS) was introduced as the major component in the polymeric solution due to its relative lower refractive index mismatch with the fiber core, which prevnets high coupling loss introduced by the light interaction with the functional coating. Darocur 1173 was utilized as photoinitiator, and detailed preparation process can be referred to previous literature [25]. The optimized chemical composition is listed in the table 1 as recipe b-2.

Table 1. The composition of the UV-curable polymer.

Sample name	*Pre-polymer*				*Active solvent*			*Assistant agent*	*1173*	*Refractive index*	*The formation of the film*
	V-PDMS	M-MA-PDMS	MA-PDMS	TFMA	V21-PDMS	V22-PDMS	APTMS	MCP-M-PDMS			
a-1	83	-	-	1	-	-	-	14	2	1.4107	-
a-2	-	83		1	-	-	-	14	2	1.4229	-
a-3	-	-	83	1	-	-	-	14	2	-	-
b-1	-	-	83	-	1	-	-	14	2	1.4206	strong, bubbles
b-2	-	-	83	-	-	1		14	2	1.4212	strong, good
b-3	-	-	83	-	-	-	1	14	2	1.4184	strong, bubbles
c-1	-	-	80	18	-	-	-	-	2	1.4065	weak
c-2	-	-	90	8	-	-	-	-	2	1.4064	weak
c-3	-	-	95	3	-	-	-	-	2	1.4058	weak

2.4 Evanescent Wave Absorption

2.4.1 Evanescent Wave

The evanescent wave-based optical sensor benefiting from its large signal-to-noise ratio has been extensively deployed as the reliable sensing system with high performance for chemical sensing [26-28] and environmental monitoring [29-31]. Evanescent wave is formed when the mismatch of refractive index between the fiber core and cladding is within the range of wavelength. The optical field in the fiber core will decay exponentially towards the fiber cladding, enabling a small portion of light propagating in the cladding as indicated by the red circle in figure 13. Two parameters associated with evanescent wave need to be carefully evaluated when designing the corresponding optical sensor: penetration depth (d_p) and the evanescent power.

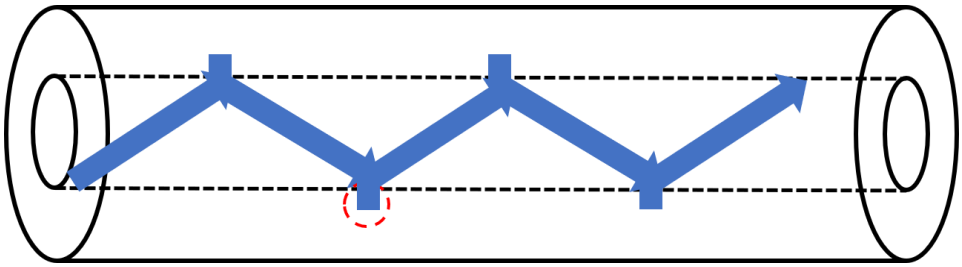

Figure 13. Schematic image of evanescent wave in optical fiber.

The penetration depth of evanescent field can be defined as the distance that light couples outside the fiber core when the amplitude of electrical field decreased to 1/e of its original level at the interface, and it can be summarized by the following equation:

$$d_p = \frac{\lambda}{2\pi\sqrt{(n_{core}^2 sin\theta^2 - n_{clad}^2)}} \tag{2.1}$$

where λ and θ denotes the wavelength of incident light and light incident angle, respectively. n_{clad} and n_{core} are refractive indices of the corresponding fiber cladding and core. It is worth noting from the equation that penetration depth of the evanescent wave is in reverse proportional to the refractive index mismatch between the core and cladding. To achieve more significant light interaction, the refractive index of the polymer should be as close to the fiber core as possible to maximus the evanescent wave penetration depth.

Meanwhile, the power of evanescent wave presented in the fiber cladding is usually noted as its fractional power to the total power in the optical fiber [32]:

$$\frac{P_{clad}}{P} = \frac{4\sqrt{2}}{3\sqrt{V}} \tag{2.2}$$

where V is the dimensionless parameter that relates to the frequency of the light and fiber dimensions:

$$V = \frac{2\pi}{\lambda}\rho[n_{core}^2 - n_{clad}^2]^{1/2} \tag{2.3}$$

where ρ stands for the radius of the optical fiber core. According to the above equations, the power of the evanescent wave is in reverse proportional to the fiber core diameter. Multiple approaches have been investigated to enhanced the evanescent field for the improvement of sensor performance by scaling-down the dimension of fiber core [33, 34].

2.4.2 Evanescent Wave Absorbance

Most of the evanescent wave based optical sensor utilizes intensity attenuation introduced by the light interaction with sensory material as an indicator for the sensing measurement. The light absorption by the sensing material differs when exposed to the targeted chemical or

environmental conditionals, which affects the transmitted light intensity as a result. The coating length of sensory material can introduce exponentially attenuated transmission power:

$$P_L = P_0 e^{-\gamma L} \tag{2.4}$$

where L denotes the coating length and γ is the absorption coefficient of the sensory film which relates to the sensory material properties. P_0 is the optical power before the light interaction with sensory film.

According to Beer-Lambert Law [35], the equation of evanescent wave absorbance can be given as:

$$A = 4\,\frac{\sqrt{2}}{3}\frac{\lambda}{2\pi r\sqrt{n_{core}^2 - n_{clad}^2}}\frac{\alpha CL}{2.303} \tag{2.5}$$

where, C is the concentration of the molecule, α is the absorption coefficient.

From the above equations, we notice that the longer coating length would introduces more significant response as more light is attenuated by the functional coating. However, as the attenuation increases, the detectable output signal would decrease dramatically. A good balance of those two factors needs to be considered each time during the sensor development. Besides, the light attenuation by the sensory film is also a function of the refractive index mismatch. In most cases, the fiber cladding is replaced by the functional material as the new cladding. So, it is ideal for the sensory film to have a refractive index as close to the fiber core as possible to the maximize the light interaction and improve the sensor performance. The similar ideology of balancing the sensory performance and sensing range is applicable in this situation too for various application purposes.

2.5 Fabry-Perot Interferometer

2.5.1 Principle of Fiber Fabry-Perot Interferometer

Fiber-optics sensor based on Fabry-Perot interferometer (FPI) has been widely deployed in structure health monitoring applications through the measurement of strain, temperature, and pressure [36-40]. The distinguished characteristics of fast-response, resilience to the electromagnetic interference, and high-sensitivity make it a promising candidate for the chemical measurement too. Depending on the cavity configurations, there are generally two types of FPI sensor: EFPI and IFPI which is short for extrinsic and intrinsic FPI interferometers, respectively. An EFPI was formed when the cavity of the sensor was constructed by two fiber ends with air gap while an IFPI was usually fabricated through fiber Bragg grating inscribed into the core region with cleaved fiber tip serving as a mirror or two mirrors as both reflective surfaces were fabricated through laser processing. In this work, the IFPI cavity was formed by the two enhanced Rayleigh scattering point fabricated by femtosecond laser writing.

Optical interference servers as the underlying principle of FPI sensors, in which the optical beam is usually split into two separated optical signals with different optical path severing as the cavity length. The recombined light property such as the intensity is a function of the cavity length which could be modified when exposed to the environmental change. By analyzing and demodulating the recombined interference patterns, the variation of cavity length will be extracted, which serves as an indicator of targeted chemicals or environmental variations. Mathematical calculations can be deduced referring to the configuration of figure 14.

In the figure, two points in optical fiber with specific separating distance (from 200 nm to 1 mm) were inscribed by femtosecond laser to form nanograting structures for the enhancement of

the Rayleigh backscattering, which behaves as two mirrors inside the optical fiber [41]. The Rayleigh enhancement of the background signal is around 45 dB. To eliminate the Fresnel reflection from the fiber end that interferes with the Rayleigh backscattered signal generated from the cavity, the optical fiber was physically coiled to form multiple small cycles with diameter less than 0.5-cm to maximus the loss at the fiber end, and the total reflected light becomes the sum of the light reflected from R_1 and R_2 interface, when neglecting the relative small signal of the Rayleigh scattering from unenhanced areas.

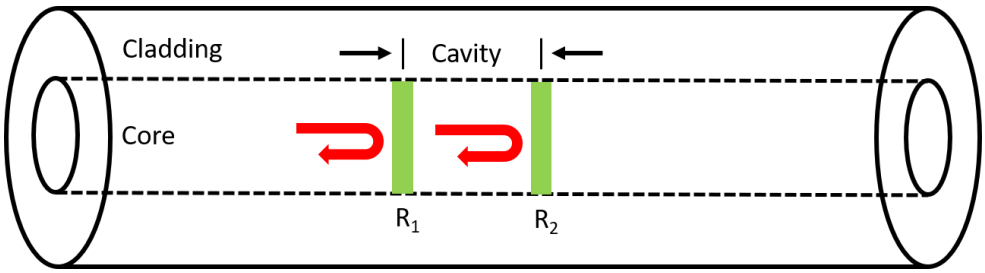

Figure 14. Schematic of the intrinsic FPI structure.

The intensity of the Rayleigh backscattered light can be calculated as [42]:

$$I_{rtotal}(\lambda) = I_{1ref}(\lambda) + I_{2ref}(\lambda) + \sqrt{I_{1ref}(\lambda) I_{2ref}(\lambda)} \cos(\phi) \quad (2.6)$$

where λ is the input light wavelength, I_{1ref} and I_{2ref} stand for the reflected light intensity from Rayleigh enhanced point 1 and 2, respectively. ϕ denotes the phase difference between the back-reflected light introduced by the optical path difference (cavity length) when the phase shift caused by the material is neglected. The phase difference can be described as:

$$\phi = 2kn_{eff}Lcos(\theta) \quad (2.7)$$

where k denotes the wave vector, n_{eff} stands for the effective refractive index, θ is light incident angle, L is cavity length. Cos(θ) approaches to 1 for optical fiber due to the small incident angle and will be neglected during following discussions.

Assuming that the laser enhanced points have the same reflectivity, and the total reflected light intensity can be rewrite as:

$$I_{rtotal} = I_{input} \frac{2R(1-cos\phi)}{1+R^2-2Rcos(\phi)} \tag{2.8}$$

where R is the reflectance of the Rayleigh enhanced surface. By introducing the term of finesse F, the transmitted output power ratio can be calculated as:

$$\frac{I_{trans}}{I_{input}} = \frac{1}{1+Fsin^2(\phi/2)} \tag{2.9}$$

where the finesse is:

$$F = \frac{4R}{(1-R)^2} \tag{2.10}$$

It can be noted from the equation that the output power change is a related to the cavity length. By demodulating the output light power spectrum, the cavity length variation can be calculated. This equation is defined as the Airy function. MATLAB was utilized to quantify the relationship between the phase shift and the transmitted or reflected light power, and the results are plotted in figure 15. The phase shift ranges from -6π to 6π, and the fitness was adjusted from 0.5 to 5. As can be seen from the simulation, large fitness results enhanced reflected light, which is in consistent with the increased reflectance in equation 2.10. In our case, the enhancement of the backscattered light introduced by laser irradiation is more than 40 dB compared with random Rayleigh scattering caused by the fiber density fluctuation, which could significantly improve the signal-to-noise ratio and results better resolution for chemical sensing.

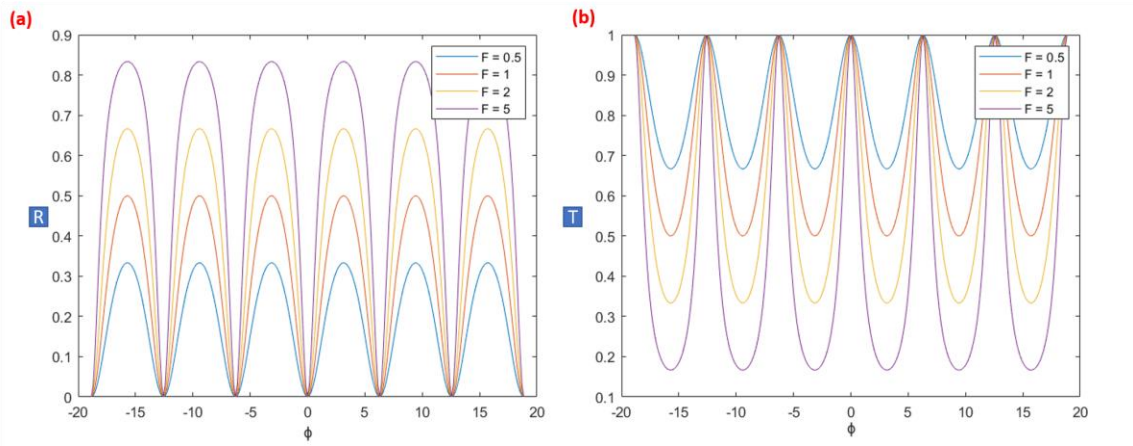

Figure 15. Reflected (a) and transmitted spectrum (b) of Airy function.

The resulted interference spectrum of intrinsic FPI sensor with 1 sensing cavity fabricated by femtosecond laser writing is shown in the figure 16, and a well-defined fringe with good contrast was observed in the figure.

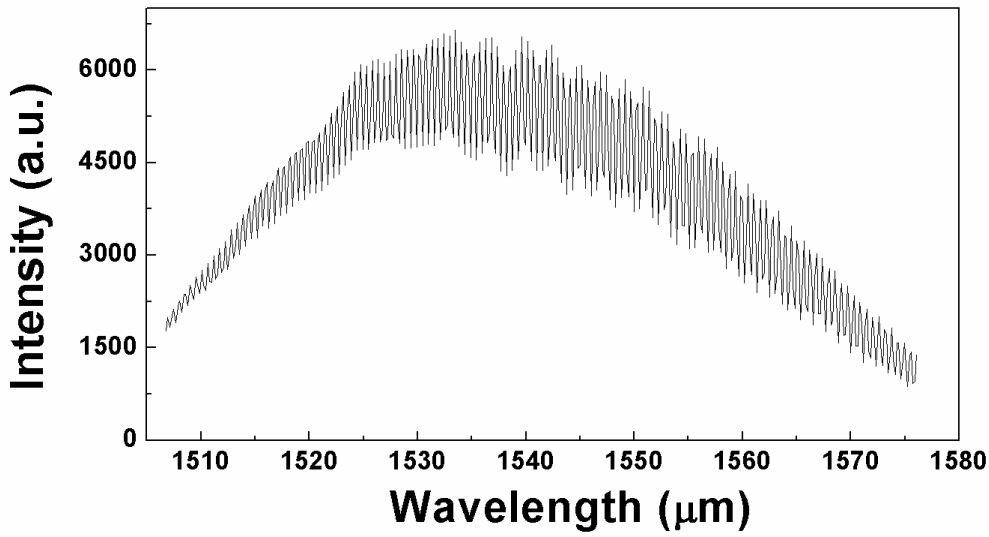

Figure 16. FPI sensor interference spectrum.

2.5.2 Fabrication of Fabry-Perot Cavity in Optical Fiber

The sensing cavity of fiber FPI sensor was fabricated through ultrafast laser writing. The experimental setup is shown in figure 17(a). The laser source utilized in the experiment is a femtosecond laser with pulse width of 300-fs and operating wavelength of 800-nm. The Coherent RegA laser system operates at 250 kHz, and the laser beam with 80 nJ energy was reshaped to form a symmetrical beam with the dimension between 2 μm to 7 μm, and further focused to the fiber core through an oil emersion objective with NA of 1.25 to eliminate the spherical aberration. Once finishing the laser irradiation on the first point of optical fiber, the moving stage would roll the fiber another position with specific distance for the second point writing. Those two enhanced points form a cavity that reflects the optical light inside the glass fiber, and the separating distance between those points are defined as the cavity length.

OBR 4600 (Luna) system based on the principle of optical frequency domain reflectometry (OFDR) was utilized in the experiment to quantify the reflected light distribution along the optical fiber. The detailed OFDR mechanism will be covered in next section of this chapter. The OFDR spectrum of enhanced fiber is shown in the figure 17(b). A highly reflective peak with the enhancement of over 50 dB was observed. The zoomed-in image of the reflected points is shown in the inset. The single reflective peak actually consists two reflection points with the separating distance less than 1 mm. Those two peaks correspond to the Rayleigh enhanced points by the femtosecond laser irradiation in the optical fiber core, and distance between them are the resulted cavity length.

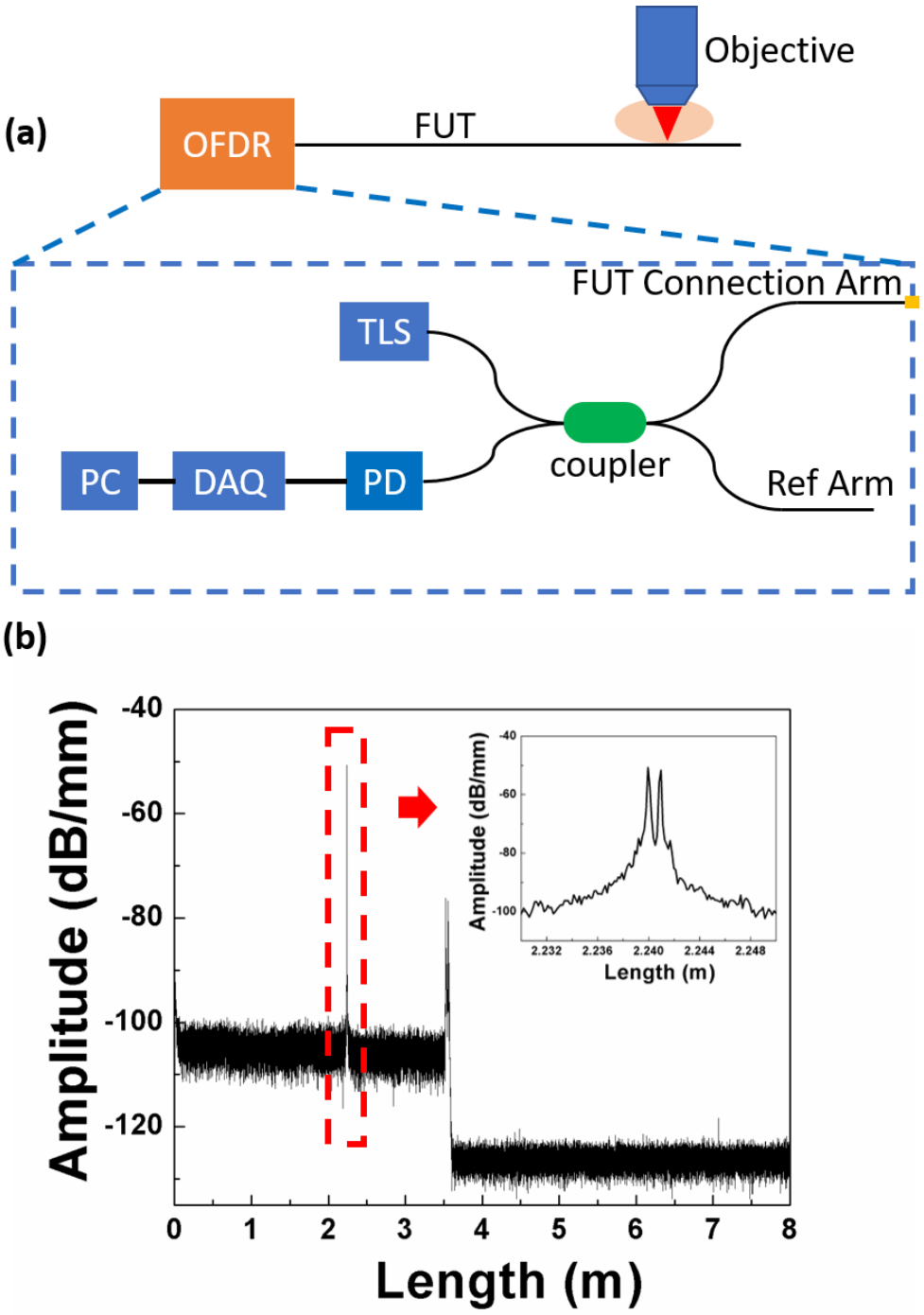

Figure 17. (a) Schematic of the cavity fabrication by femtosecond laser writing, (b) OFDR spectrum of the enhanced fiber with 1 cavity, inset is the enlarged figure of the enhanced points.

2.6 Rayleigh Optical Frequency Domain Reflectometry

2.6.1 Overview

Optical fiber, benefiting from low transmission loss (0.2 dB/km), small form factor (< 200 μm) and large bandwidth (> 100 Tbits/s), has been widely deployed to replace the traditional copper cord cable for long-distance communication applications. Moreover, with slight modification, fiber optics was found to be quite responsive to environmental variations such as the temperature, strain, chemical, and humidity, etc. The inert nature of the glass fiber also enables it to operate under harsh environmental conditions such as the elevated temperatures, strong electromagnetic interference, where the electrical counterpart cannot survive. Those merits promote the extensive implementation of optical fiber sensors in recent decades.

The most common and well-established optical sensor is used for point sensing applications, which monitors the collected signals along the sensing region, for example, the transmitted light intensity variations responding to hydrogen change at high temperature actually reflect the accumulated response of the 10-cm sensory film [43] where the behavior of each point along the sensing region remains unknown. Another approach to fabricate point sensor is through the structural modification of the optical fiber, and the most commonly methods are fiber Bragg Grating (FBG) and interferometers. FBG is fabricated when the refractive index of the fiber core is periodically modified through UV interference light writing, generating a reflected signal with specific wavelength determined by the period of structures. The wavelength shift can be used to quantify the environmental variations [44]. Interference based optical sensor such as Fabry-Perot interferometer has also been proved to be versatile in the vibration, strain, and temperature measurement in recent years [45, 46].

In addition to point sensing, sensor with the capability of monitoring signal change along the optical fiber with high spatial resolution has great potential in many applications such as the structural health monitoring, pipeline leakage detection, etc. Those sensors are usually being referred as distributed sensors. A series of FBG sensors resonated at different wavelengths can be utilized in distributed sensing applications [47, 48]. However, FBG series is not the best option for the scenarios with high demand of spatial resolutions since it can only record the event that occurs around the FBG where the events happen between those FBGs cannot be detected, and the spatial resolution is also significantly limited by the fabrication process of grating.

A distributed sensor capable of recording every event along the optical fiber can be very innovative as well as challenging in optical sensing research. In previous decades, multiple approaches have been investigated for the development of distributed sensor, most of them are based on the light interaction with optical fiber through scattering mechanism including Rayleigh [49], Brillouin [50], and Raman scattering [51].

Rayleigh scattering is an elastic scattering process introduced by the light interaction with the irregular microscopic structures of optical fiber caused by the random density fluctuation introduced by the fiber drawing approach. The most investigated sensing technologies based on Rayleigh scattering are optical time domain reflectometry (OTDR) and optical frequency domain reflectometry (OFDR), of which the intensity of Rayleigh scattering is related to environmental conditions such as temperature and strain so that it could be used to extract the local information after demodulation. A pulse laser is utilized as the light source to interact with the optical fiber during the OTDR measurement. The Rayleigh backscattered light from optical fiber combines with Fresnel reflection resides at the fiber tip are recorded by photodetector, and distance of the scattered events in referring to the starting position can be determined by multiplying the time

difference between the input signal and the received backscattered signal with light speed in the optical fiber. The performance of the OTDR system is evaluated by the tradeoff between the pulse width and dynamic range of the sensor. The short pulse width can potentially increase the spatial resolution by avoiding large deadzones, however, the dynamic range of the system will be compromised. The sensing range can be extended up to 120 km with the tradeoff of spatial resolution. By modulating of the pulse width and sensing range, the spatial resolution of the OTDR can be adjusted from 4-cm to multiple meters, which is still not high enough for chemical sensing and structural monitoring applications.

OFDR system was then being developed to address the applications with high resolution and large dynamic range requirement. The first model of OFDR involves the frequency modulated continuous wave Radar [52]. The Rayleigh backscattered signal is collected by the photodetector which further maps into spatial information through Fourier transform. The maximum spatial resolution of OFDR system is determined by the laser spectrum width: large wavelength spectrum range usually yields improved spatial resolution. OFDR can also be treated as a series of FBGs in the optical fiber when utilized for chemical and environmental sensing. Multiple approaches have been adopted using OFDR for distributed measurement of temperature [53] and strain [54]. The OFDR system utilized in this dissertation is from Luna (OBR 4600) with a sensing resolution of 1 με and 0.1 ℃ for strain and temperature, respectively.

2.6.2 OFDR System and Principle

Rayleigh based OFDR system has been studied and deployed by multiple groups [55-57]. The schematic diagram of typically OFDR system is shown in figure 18. Tunable laser source (TLS) was utilized to provide the input light, and the system also consists the auxiliary

interferometer, reference beam, fiber under test (FUT), and signal detection and processing components. Auxiliary interferometer consists of multiple fiber couples (FC) and a delay line. The polarization of the reference beam is tuned by the polarization controller (PC). Polarization beam splitter (PBS) was utilized to decouple optical beam into two orthogonal portions recorded as the P and S part. Photodetector (PD) and data acquisition card (DAQ) collect the output signal and perform the AD (analog to digital) transition.

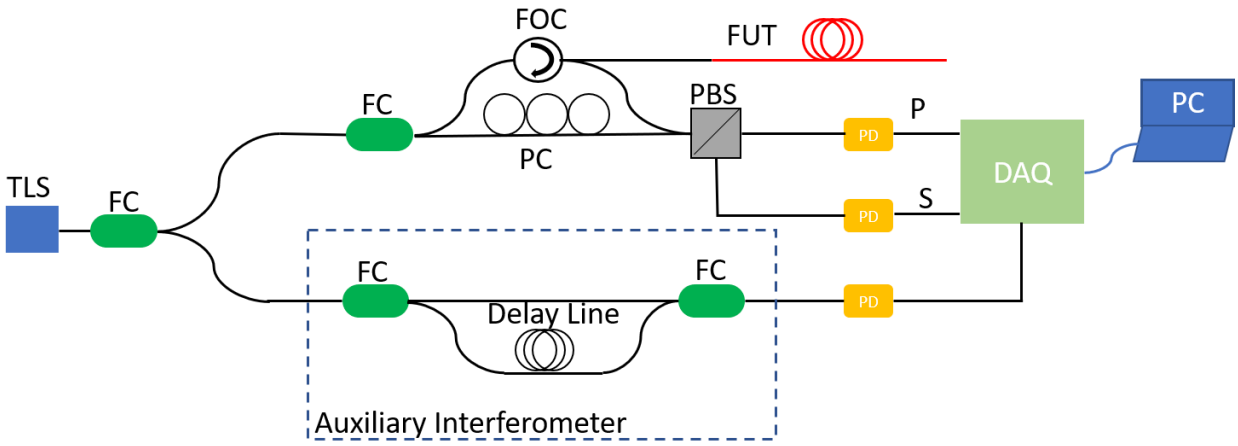

Figure 18. Schematic of OFDR system.

The light from the tunable laser source is initially split into two branches: the lower auxiliary branch and the upper measurement branch. Only 1% of the initial power is coupled into auxiliary interferometer, which was utilized to eliminate the nonlinearity of the laser tuning. Optical beam on the top branch was further divided into two arms: a reference arm with the adjustable polarization and the tested arm with targeted optical fiber. The backscattered light passes through a fiber optical circulator (FOC) and recombined with the reference beam. The beam was further split by PBS and captured by the photodetector. The electrical field of the light source is given as [57]:

$$E_{input}(t) = E_0(t)e^{i\varphi(t)} \tag{2.11}$$

where $\varphi(t)$ is the phase of the light and can be written as a function of the optical frequency:

$$\varphi(t) = \int_0^t \omega(t)\, dt \tag{2.12}$$

when laser source is linearly tuned: $\omega(t) = \gamma + \omega_0$ and equation 2.12 can be rewritten as:

$$\varphi(t) = \int_0^t \gamma + \varphi_0\, dt = 0.5\gamma t^2 + \omega_0 + \varphi_0 \tag{2.13}$$

where $\gamma, \omega_0, \varphi_0$ stand for frequency tuning speed, initial frequency and initial phase of the input light, respectively. The light intensity traveling at point z in the FUT can be written as:

$$E(\tau_z, t) = \frac{A_Z}{\sqrt{2}} E_{0(t-\tau_z)} e^{-\alpha l_z} e^{i\varphi(t-\tau_z)} \tag{2.14}$$

where l_z is the distance that light travels to reach position z, α is the attenuation coefficient. The electrical field of backscattered Rayleigh light is defined as:

$$E(\tau_z, t) = \frac{A_Z}{\sqrt{2}} r(z) E_{0(t-2\tau_z)} e^{-2\alpha l_z} e^{i\varphi(t-2\tau_z)} \tag{2.15}$$

where $r(z)$ is the Rayleigh backscattering coefficient. The backscattered light along the whole fiber can calculated as the sum of all the reflections:

$$E_a(t) = \frac{A_a}{\sqrt{2}} \sum_z \left(r(z) E_{0(t-2\tau_z)} e^{-2\alpha l_z} e^{i\varphi(t-2\tau_z)} \right) \tag{2.16}$$

where A_a is the total phase shift introduced by the FUT. The backscattered light recombines with the light from reference arm, and the total electrical field is:

$$E(t) = E_a(t) + E_a(t)$$
$$= \frac{A_a}{\sqrt{2}} \sum_z \left(r(z) E_{0(t-(2\tau_z+\tau_a))} e^{-2\alpha(l_z+l_a)} e^{i\varphi(2\tau_z+\tau_a)} \right) +$$
$$\frac{A_b}{\sqrt{2}} i E_{0(t-\tau_b)} e^{-\alpha l_b} e^{i\varphi(t-\tau_b)} \quad (2.17)$$

The recombined light was then split to P and S part by PBS, and each portion can be described as the following equations:

$$E_p(t) = \frac{p_v T_p e^{i\varphi_p} A_a}{\sqrt{2}} \sum_z \left(r_p(z) E_{0(t-(2\tau_z+\tau_a))} e^{-2\alpha(l_z+l_a)} e^{i\varphi(2\tau_z+\tau_a)} \right) +$$
$$\frac{A_b}{\sqrt{2}} i E_{0(t-\tau_b)} e^{-\alpha l_b} e^{i\varphi(t-\tau_b)} \quad (2.18)$$

$$E_s(t) = \frac{s_v T_s e^{i\varphi_s} A_a}{\sqrt{2}} \sum_z \left(r_s(z) E_{0(t-(2\tau_z+\tau_a))} e^{-2\alpha(l_z+l_a)} e^{i\varphi(2\tau_z+\tau_a)} \right) +$$
$$\frac{A_b}{\sqrt{2}} i E_{0(t-\tau_b)} e^{-\alpha l_b} e^{i\varphi(t-\tau_b)} \quad (2.19)$$

where p_v and s_v stand for the vector component of p and s, respectively. T_p and T_s stand for the split part of PBS, φ_p and φ_s denote the phase shift introduced by PBS, r_p and r_s are the Rayleigh backscattering coefficients.

Taken the linearly tuned laser source (equation 2.13) into consideration, the final output power at photodetector is the sum of the P and S component, and can be summarized as:

$$I^{AC}(\mathrm{t}) = \sum_z m(z).\cos(2r\tau_z) \quad (2.20)$$

where m(z) is amplitude of the constant parameters:

$$m(\mathrm{t}) = |m(t)| e^{i\theta(t)} \quad (2.21)$$

m(t) is time invariant so that m(t, z) = m(z).

Apply Fourier transform to equation 2.20, and the equation can be transformed into frequency domain:

$$I^{AC}(\omega) = \frac{\sqrt{2}\pi}{2}\sum_{z} m(z).e^{i\varphi(z)}\delta(\omega - 2r\tau_z) \tag{2.22}$$

In this equation, the frequency response is associated with specific position of z, which, in turn, could be used to extract the local information. Moreover, the intensity of the signal at specific frequency corresponds to Rayleigh backscattered signal amplitude at that location.

Rayleigh backscattering, similar as FBGs, encounters a frequency shift when the sensor is responsive to the environmental variations such as the length variation of optical fiber caused by the strain and temperature, which could be modeled by a weak FBG [58]. The wavelength shift can be described as the following equation:

$$\frac{\Delta\lambda}{\lambda} = C_T\Delta T + C_\varepsilon\varepsilon \tag{2.23}$$

where C_T is the thermal expansion coefficient related to both effective refractive index and grating period variations, and C_ε is the strain coefficient.

Spatial resolution is a fundamental factor in evaluating the performance of the OFDR system, and it can be refer as [59]:

$$\Delta Z = \frac{c}{2n_g\Delta v} \tag{2.24}$$

where Δv is the bandwidth of tunable laser source. It is easy to notice that in order to achieve high spatial resolution, laser with larger wavelength tuning range is desirable. The maximum detection length can also be described as:

$$L_{max} = \frac{c\tau_g}{4n_g} \tag{2.25}$$

where τ_g is the differential delay for auxiliary interferometer. Noting that although the sensing length is proportional to the differential delay, the coherence length of the tunable laser source is still the predominate factor in determining the maximum probing distance.

3.0 Optical Methane Sensor Based on Metal-Organic Framework Functionalized Polymer Coating

Methane sensor with the merits of large-scale application, real-time monitoring, and low cost has great potential for energy usage including gas storage, pipeline monitoring, which draws ongoing research efforts. This chapter presents two fiber optical methane sensors based on functionalized material coating. Functional film is optimized by adjusting the MOF and polymer composition. The performance of the sensor was characterized in terms of the sensitivity, response speed, and repeatability.

3.1 Overview

Natural gas has been widely deployed as an alternate for fossil fuel to address the pollution and global warming issues. In recent years, vast investment has been made for the establishment of the infrastructure to prompt the implementation of natural gas in energy usage. At the meantime, the real-time gas monitoring system capable of addressing the growing concerns of safety, greenhouse gas emission is becoming increasingly crucial, which requires better sensing metrologies. Fiber optics methane sensors have been investigated as a scalable and versatile solution due to its superior property of low-cost, low-loss, remote-sensing, and resilient to the environmental disturbance. Customized optical fibers [2, 60-62] and sensors based on fiber grating [63-66] have been developed for methane gas monitoring in the past few years with good sensitivity and selectivity.

The properties of evanescent wave such as penetration depth and intensity, to very large extent, corresponds to the refractive index mismatch between fiber core and cladding. A minor change of the cladding-core refractive index could produce significant modification of the evanescent wave attenuation, which serves as the basic principle of evanescent wave based sensor for chemical sensing including methane gas [67-70]. The recording of attenuated output light intensity and absorption spectrum are among the most common approaches for evanescent-wave based sensor characterization.

Functional sensory coatings including both organic and inorganic materials have been introduced for methane detection, for example, 2-dimensional graphene [68] and Cryptophane-A [69, 70]. Although a well-defined sensory behavior was observed for both sensors, the high cost of the material and the incompatibility with current fiber manufacturing process prevent them from large-scale applications. To address this issue, the functional coating needs to be engineered according to current fiber drawing process while maintaining its functionality. In this work, fiber coating is achieved through integration of UV-curable polymer with low refractive index and metal-organic framework (MOF). Optical sensor based on in-situ Cu-BTC (benzene-1,3,5-tricarboxylic acid) MOF film has been developed for carbon dioxide detection, and a repetitive and rapid response with high sensitivity is obtained in previous literature [71]. However, the in-situ layer-by-layer method for MOF integration on optical fiber is a time-consuming and over-complicated process that cannot be utilized for long-distance monitoring at reasonable cost.

To address this issue, we developed an UV-curable polymer system and integrated MOFs into the polymeric coating films as functional element to monitor the environmental change. The coating process is compatible with the current fiber polymeric jacket fabrication process and can be easily applied to the current coating system with minor adjustment. To form a rigid sensory

film on top of the optical fiber with good performance, the polymer must meet mechanical and optical requirements. The reflective index of the polymer should be slightly lower than the fiber core to reduce the light attenuation for long-distance applications. Besides, to avoid the light scattering and huge-absorption, a good transparence of the sensory film must be achieved for the measurement. Besides, the functionalized coating after UV curing must be rigid yet flexible enough to respond to geometrical change introduced by the methane gas. The adhesion of the polymer should also be optimized to prevent the detachment of the sensory film at the interface after gas exposure.

3.2 Sensory Film Optimization

The chemicals utilized in the experiment for the synthesis of UV-curable system is shown in figure 19. The detailed polymer optimization process can be found in table 1. Poly (dimethylsiloxane) (PDMS) acts as the pre-polymer in the mixture solution due to its lower-cost, flexibility, resilient long-chain, and low refractive index. Mercapto-functional PDMS was also introduced into the coating system to increase the adhesion between the polymer mixture and optical fiber. Moreover, Darocur 1173 was utilized in solution as photo-initiator to accelerate polymerization process of the functional coating when exposed to UV light. Vinyl terminated PDMS was also added into the polymeric system to improve the light sensitivity of the coating for the formation of strong film during UV exposure.

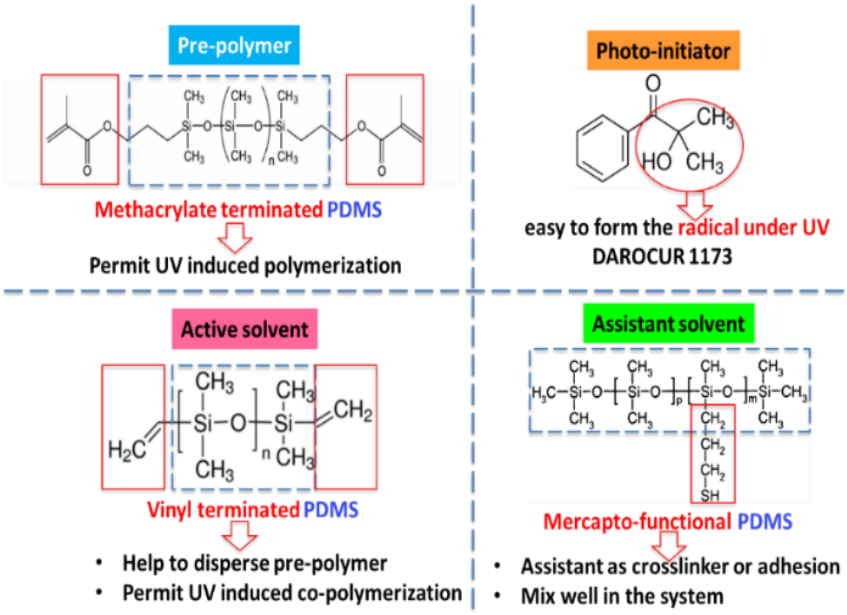

Figure 19. Chemicals used in the UV-curable polymeric system.

ZIF-8 MOF was utilized as the methane absorption agent in the system. It was synthesized in solution-based environment with mixture of methanolic solution and zinc nitrate hexahydrate at room temperature followed by centrifuge at 11000 rpm for 5 min. Methanol was used as the solvent to disperse MOF crystals to form a MOF-methane suspension after the supernatant was discarded. The above process was repeated multiples times to extract the pure MOF crystals.

The MOF-Polymer mixture coating system was then prepared by adding the MOF-methanol suspension into the pre-polymer drop by drop. The mixture solution was stirring for 48 h until the MOF crystal dispersed into the polymer solution to form a uniform milky emulsion without the existent of the white power cluster. The MOF-Polymer system was cured under UV lamp for 1 min. The coating system was further optimized in term of the refractive index, mechanism strength, and flexibility by adjusting the MOF concentrations. Prism coupler (Metricon Inc) was utilized to characterize the refractive indices of the film. A rheometer (Anton parr MCR 302 Instruments) was utilized for the sear rate-dependent viscosity measurement. Tensile test

(Instron 5943 equipped with Bluehill 3 software, Norwood, MA) was performed using a load cell of 10 N. Samples were stretched uniaxially with the rate of 5 mm/min until failure. The Young's modulus was calculated with the stress-stain curves slope less than 5%.

The refractive indices of the sensory coating affect the light coupling at the fiber sensory film interface, which determines the performance of evanescent wave-based sensor. Fiber core of standard SMF-28 has a refractive index of 1.45, which requires the refractive indices of the MOF-polymer solution to be slightly less than that value. To adjust the refractive index of the coating system, MOF-Polymer solution with MOF/Polymer weight ratio ranging from 0 to 1.6 was prepared for comparison, and the refractive index of the UV cured film was also measured as shown in figure 20(a).

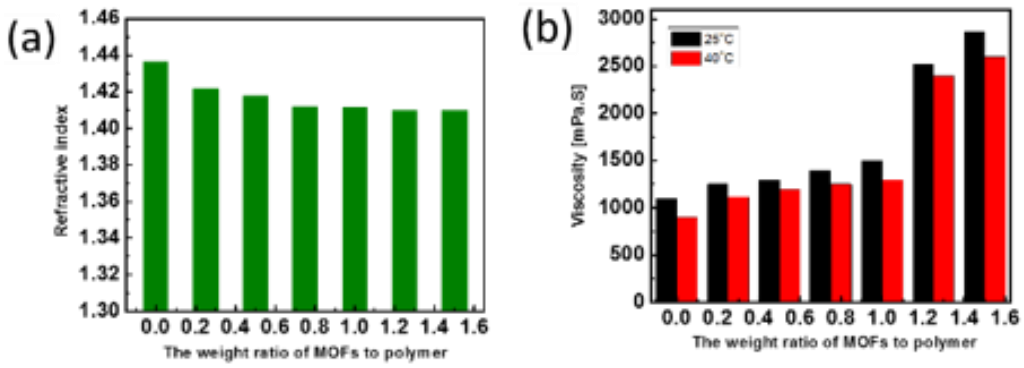

Figure 20. (a) Refractive indices of the mixture, (b) viscosity at different temperatures with the increase of ratio of MOFs.

The refractive index of the pure PDMS is around 1.44 as indicated in the figure. A continuously decrease of refractive indices was confirmed with increasing MOF ratio, which is due to the relative lower MOF refractive index of 1.33 [71]. The initial sharp drop of refractive index gradually mitigates and statures as the MOFs/Polymer ratio increase to 200%. It is also worth

noting that the refractive indices of all the samples are less than 1.45, which will prevent the huge loss during the transmission.

The viscosity of the solution was also investigated with varied MOF weight ratio through shear rate-dependence to study the Rheologic properties of the UV-curable coating films, and the result is shown in figure 20(b). In the figure, the viscosity of the solution initially increases slowly with small weight ratio, a dramatic bump is observed after raising the ratio to more than 1. The increased MOF concentrations in the coating produces stronger interaction of dispersion and emulsion. In addition, the elevated temperature of coating film resulted in more active polymeric chain which in turn reduces the friction force and viscosity.

The MOF crystals in the coating system is supposed to expand once traps the methane molecule, generating a swelling of polymeric film. In order to quickly response to the physical expansion upon methane exposure, the MOF-Polymer film needs to be elastic with good flexibility. To quantify the mechanical properties of the sensory film, the stress-stain curves of sensory film was measured by adjusting MOF ratios and the result is plotted in figure 21.

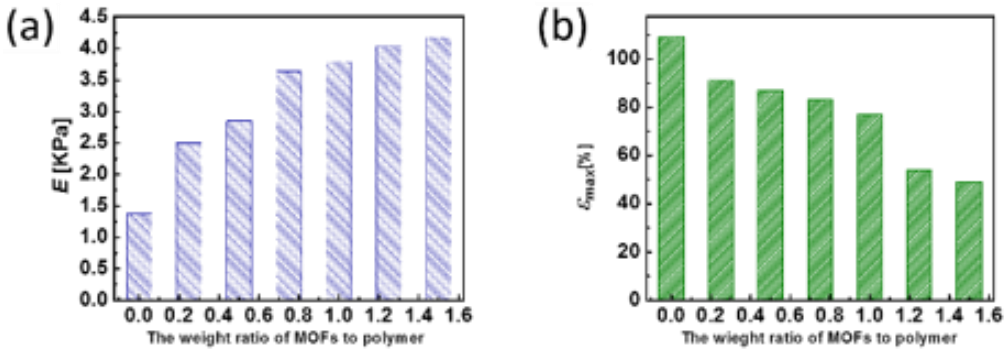

Figure 21. Young's modulus (a), and maximum elongation at break (b) of the sensory film with various MOF ratios.

In figure 21, small Young's modulus value was initially observed when few MOF is added to the coating system, coordinating maximum elongation of 109% with the elastic property of the pure prepolymer. When further improving MOF concentrations in the polymer mixture, the Young's modulus gradually increases while the elongation length of the film decreases, indicating the increased stiffness of the sensory film in this case. To balance the mechanical properties and the refractive index of the sensing film for the sensory performance, the MOF/Polymer weight ratio was chosen as 100% for the initial sensor fabrication.

3.3 Sensor Fabrication

Multimode fiber (MMF) with the core diameter of 105 μm was purchased from Thorlab and introduced in the experiment. Single mode D-shaped optical fiber was special made to remove half of the cladding by Corning Inc. 15-cm section of MMF was initially etched in acid (buffed oxide etchant) at room temperature to remove the fiber cladding and part of the fiber core. The MOF mixed emulsion was drop-casted on the optical fiber and then being transferred under the UV lamp for 1 min illumination to form a uniform coating film as the new fiber cladding. The ZIF-8 MOF and methanol dispersion solution were first drop-coated on top of the silicon wafer followed by the PdAu deposition before the topography characterization by SEM, and the result is shown in the figure 22(a). In the figure, the MOF cluster appears to be highly crystallized structure with cubic geometry. The dimension of the MOF crystal ranges from 60 nm to 100 nm as observed in the figure.

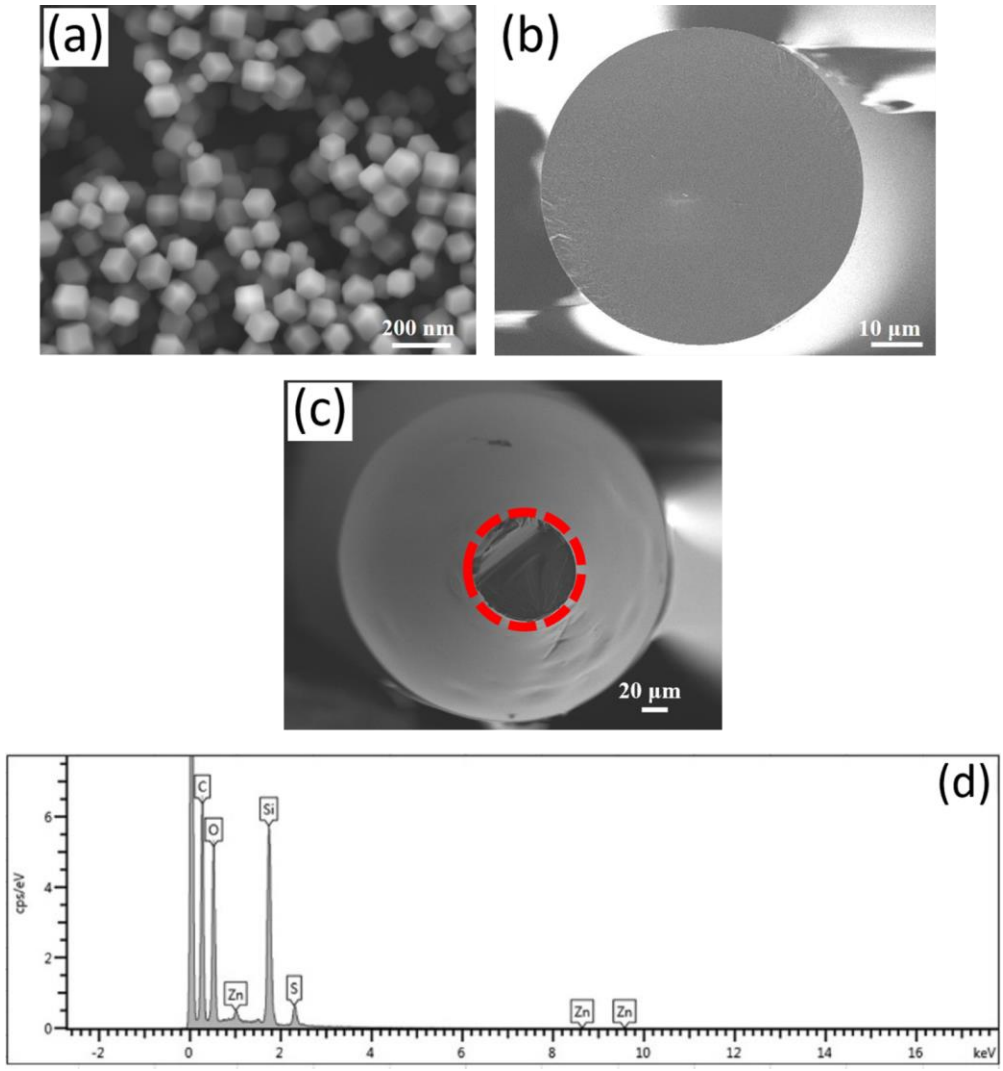

Figure 22. (a) SEM image of ZIF-8 MOF, (b) Etched multimode fiber, (c) Cross-sectional view of coated sensor, (d) EDX result of the sensor polymer cladding.

MMF was etched from 125 μm to 80 μm to enhance the evanescent wave interaction with the functional film as shown in figure 22(b) since the evanescent field power is in reverse proportional to the fiber diameter. Cross-sectional view of the fabricated sensor with optical fiber being outlined by the red cycle is shown in figure 22(c). The polymer mixture was cured by a UV lamp to form a uniform coating outside the fiber core, which serves as the new fiber cladding. The coating thickness is measured to be around 120 μm. Meanwhile, the Zinc element line located at 1.01, 8.64, and 9.57 eV was detected in the EDX spectrum, confirming the existence of the MOF crystals in the functional coating after UV curing process.

The experimental setup for the sensor performance characterization is shown in the figure 23. A tunable laser source with center wavelength of 1666 nm and adjustable wavelength range of 2-nm was utilized to provide the input light during the test. The light located at non-absorptive wavelength of 1666.5 nm was coupled into the optical fiber. The gas concentrations were adjusted by tuning the flow of the nitrogen and methane gas through a mass flow controller, and the flow remains at constant value of 20 sccm. The nitrogen gas was used as the carrier gas and the experiment was carried out at room temperature. Transmitted power of the sensor was recorded by an amplified photodetector and converted into the digital signal by a date acquisition card.

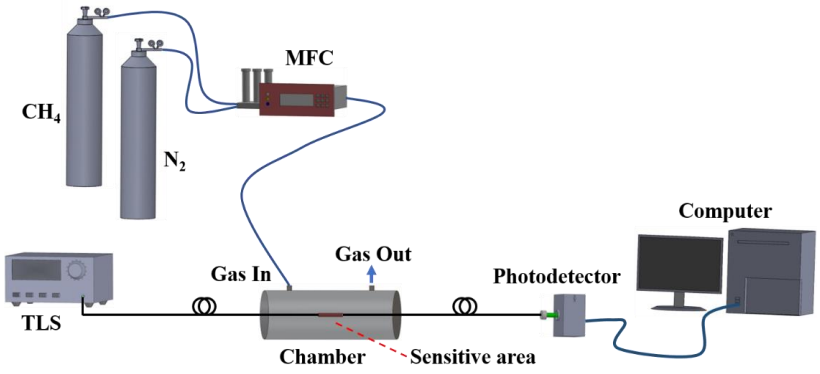

Figure 23. Experimental setup.

3.4 Sensor Characterization

To begin with, the chamber was first purged with pure nitrogen gas for 10 min to create the nitrogen environment. Methane and nitrogen mixture gas with specific ratio was then introduced into the chamber. The sensor was further exposed to the pure nitrogen gas again to reset the status of sensor back to its initial level. The methane gas with the concentration between 1% to 50% was utilized in the measurement. Real-time response of transmitted power variation to gas exposure was plotted and shown in the figure 24.

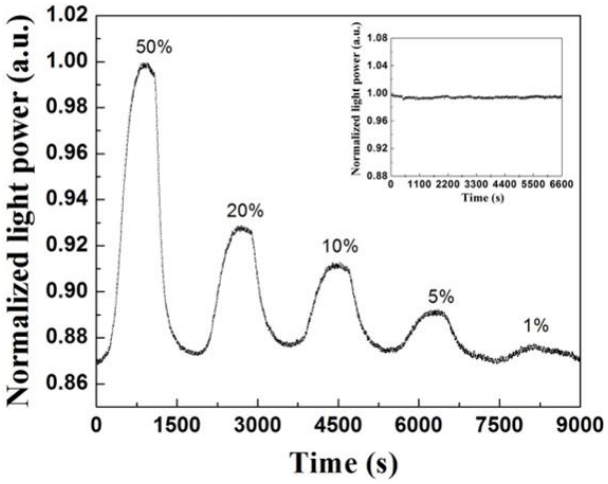

Figure 24. Time-dependent response of sensor in response of methane exposure with various concentrations, inset is the response of the reference sensor without MOFs.

The transmitted power increases when introducing the methane gas into the system. A 13% increase of the fiber output power was observed when exposed to methane gas with the concentration of 50%. As we reduce the methane concentration, the output power decrease as well. However, a sharp power change is initially obtained when the methane gas concentration drops to 20% and the rate of the power change reduces to 10% while less level of the methane was

introduced, indicating a nonlinear response of the sensor. This phenomenon might associate with the nonlinearity of the polymer expansion process due to the gas diffusion process. The output power changes upon 5% methane exposure is 3 times larger than the response of 1% methane, which enables the sensor to response to the gas up to 1%. Moreover, nitrogen gas introduced after methane cycle reduces the output power, which stabilizes at the level comparable to initial status in terms of the light intensity. This phenomenon helps to initiate the optical fiber back to its original status and help to establish the reversibility of the sensor. The inset is the behavior of the sensor with only prepolymer coating without MOF functionalization. The same concentrations of methane and nitrogen gas was delivered into the system and no apparent response was observed during the whole process, which confirms the functionality of MOF crystal in the sensor.

Another factor worth considering for evaluating the performance of optical sensor is the reversibility that response of the sensor can be repeatable under the same environmental conditions. Herein, multiple cycles of methane gas with same concentrations was introduced into the system. The same methane gas ranges from 1% to 50% was investigated in this work. The experiment was carried out with a 10-min methane initial exposure followed by nitrogen resetting for the same time of period, and the experimental results are shown in figure 25.

In the figure, the responsive trace of the sensor can repeat itself for multiple cycles when the methane concentration is over 10%. The power variation during the three cycles of the 50% methane exposure is less than 2%, which gradually increases to 8% in the environment with 5% methane gas. Although there are some fluctuations in the trace within each methane concentration, the minimum transmitted power intensity for 5% is still significantly larger than the maximum power variations during the measurement of 1% methane, indicating the capability of sensor to differentiate hydrogen gas with the resolution up to 1%.

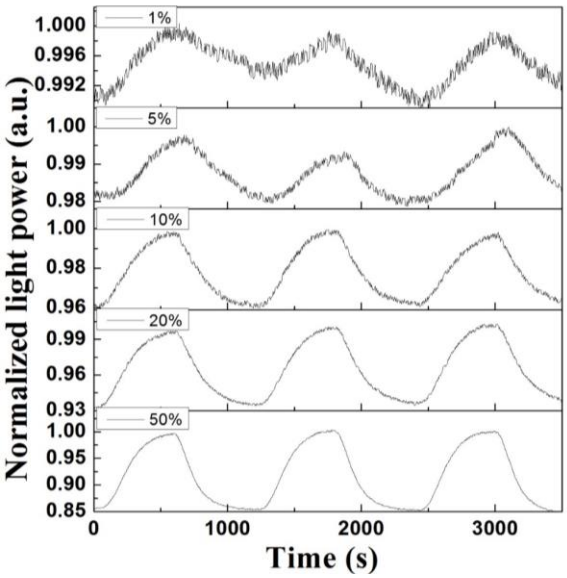

Figure 25. Sensor's response to multiple cycles of methane exposure.

The underlying principle of the transmitted power variations is associated with the evanescent wave change during the methane gas exposure since the sensor is based on evanescent field absorption. As mentioned before, ZIF-8 MOF is highly efficient in capturing methane molecules and has been extensively used for gas storage. In this case, the methane molecule diffuses into the polymer cladding and captured by the MOF crystals. The accumulated methane molecule trapped inside the polymer matrix induces an expansion of the polymer cladding, which will be further confirmed in chapter 6 during the development of the FP sensor for methane detection. The continuously expansion of polymer generates a less densified sensory film, decreasing the refractive indices of the polymer coating. According to the Beer Lambert law [35] and equation 2.5, the refractive index mismatch will be enlarged, decreasing the penetrating depth of the evanescent wave. What's more, the absorption of sensory film is in reverse proportional to the refractive index mismatch, which reduces the light absorption of the sensory film during the transmittance. The less absorbed evanescent field during the light coupling produces an enlarged

transmitted power at the detection end. Besides, the expansion of the polymer cladding is proportional to the amount of captured methane molecules. In fact, the methane gas with higher concentration tends to diffuse into the sensory film in a more significant manner, which will result an increasing number of the molecules being trapped.

To optimize the sensor, adjusting the MOF concentration is worth investigating since it could potentially affect the refractive index of the coating as well as the MOF sites for gas absorption. MOF-Polymer emulsion with the concentrations ranging from 0.1 to 1.5 were prepared followed by the same coating and curing process. The response of the 4 sensors were recorded, and the response time and intensity variation of the sensor under various MOF concentrations are shown in the figure 26(a).

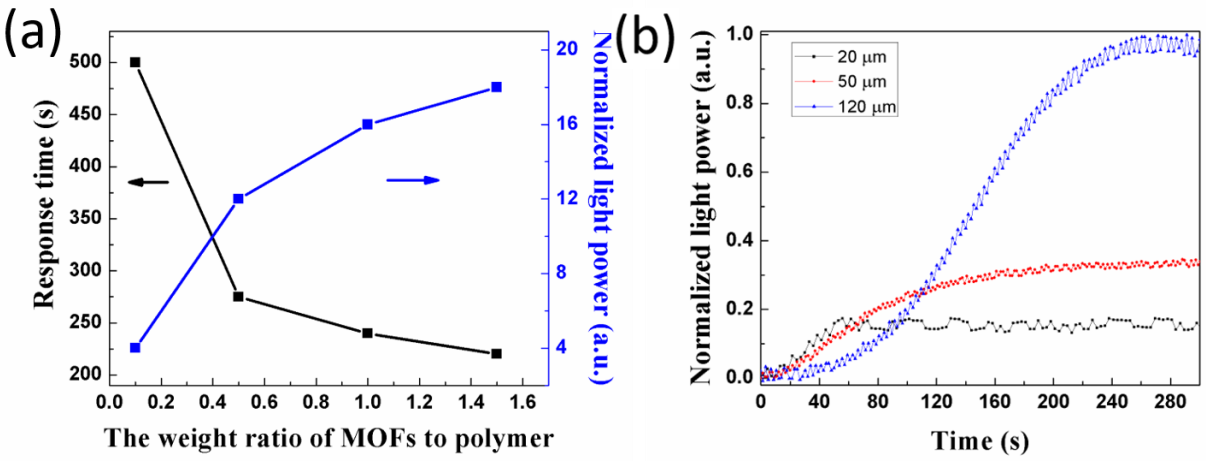

Figure 26. (a) Sensing speed and normalized power change as a function of different MOF weight ratios, (b) response of the three sensors with different coating thickness.

The response speed is calculated as the time needed for the transmitted light intensity reaching 90% of its maximum power. It is easy to note that sensors with lower MOF concentrations, for example 0.1, tends to response to the methane gas in a relative slow speed.

When increase the ratio to 0.5, an accelerated sensory speed was observed as the response time drops dramatically from 500 s to around 270 s. Further increasing the MOF weight ratio to above 0.5, the trending of sharply dropped response time did not continue. Instead, the accelerated response speed starts to slow down and tends to saturate gradually. This observation might result from the saturation of gas absorption and desorption by the MOFs. Meanwhile, a similar trace was obtained for the transmitted light intensity: the initially significant increase of the output power gradually statures when adding more MOF crystals into the sensory film. Although a larger MOF weight ratio appears to be more responsive and produces a more significant signal, the degradation of the mechanical properties prevents it from forming a flexible and uniform coating on the optical fiber. Overall, the weight ratio of 1 was chosen as the optimal concentrations for the MOF-Polymer mixture.

Sensors that can rapidly react to the environment change is very crucial for energy usage especially for the explosive gas monitoring in the pipeline or storage unit. Although the weight ratio of the functional coating has been optimized, the slow response speed of the sensor could still be problematic for real applications. To address this issue, the coating thickness of the sensor was adjusted in hoping to reduce the response time. Two sensors with coating thickness of 50 and 20 μm were fabricated and compared with the previous sensor functionalized by thick coating of 120-μm. MOF-Polymer weight ratio of 1 was applied in those sensors, and their response under the pure methane gas is shown in figure 26(b).

Compared with thick coating of 120 μm, the response time of sensor with 50 μm functional cladding is around 120 s when exposed to pure methane gas, which is twice faster than the previous result. The response speed can be further improved to 50 s when the coating thickness of the film is reduced to 20 μm. The accelerated response speed of the sensor with thin coating film can be

explained by the methane molecule diffusion process through the sensory film. A thick polymer cladding requires longer time for the methane molecule to diffuse to the interface betwen the polymer and fiber core, which is crucial for the refractive index tuning when the functional film expands. To further increase the gas response, thin film coating would be beneficial assuming the same overall sensitivity.

Besides, the coating length of the functional polymer is also a non-neglecting factor in determining the sensor performance. To investigate the effect of the MOF-Polymer functional coating length, another two MMF sensors were prepared with the coating length of 5 and 10 cm, respectively. MOF/Polymer weight ratio of 1 was also utilized as the functional coating in this case. Both sensors were loaded into the gas tube with the same sequence of gas exposure, and the experimental results are shown in figure 27.

In the figure, sensor with short sensory coating tends to have lower detection limits. Compared with sensor of 15-cm coating, sensor with 10-cm functional cladding only responds to methane gas with the concentration up to 50% as indicated in the inset. A further degradation of detection limits was also observed for the methane sensor when the coating length is shorted to 5 cm. Only pure methane gas can be differentiated with the nitrogen gas as confirmed by the time-dependent response of sensor in the inset. The degradation of the detection limits is associated with the reduced light interference with the polymer cladding. As indicated by Beer-Lambert Law [35], the absorption of the evanescent wave is proportional to the coating length L. The elongated coating length of the sensor introduced enhanced light interaction between the evanescent field and the functional polymer, generating a significant transmitted output power change that can responses to lower gas levels. For example, the transmitted power of sensor with 5-cm coating only increase by 0.6% upon pure methane exposure which is only 1/20 as compared with the 15-

cm sensor. Meanwhile, the intensity change for the 15-cm coated sensor is 14 time of the sensor with 10-cm coating. However, the output power intensity is also in reverse proportional to the coating length as indicated by equation 2.10, which will introduce huge attenuation loss when the functional coating is too long, preventing it from long-distance monitoring. To address this issue, a good balance of the coating thickness and spatial range needs to be considered. One possible solution is to improve the efficiency of the methane absorption by MOF crystals so that the etching depth of the fiber will be limited in order to achieve the same light interactions.

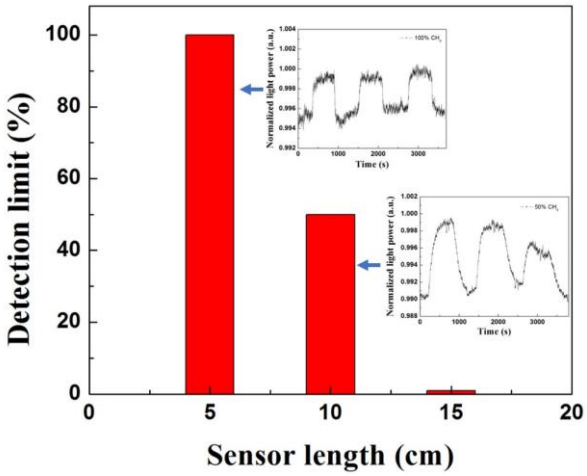

Figure 27. Detection limits of MMF sensor with various sensing length, inset is the response of the sensor exposed to the methane gas with the maximum detectable concentrations.

In additional to multimode fiber, D-shaped fiber has also been widely utilized for chemical sensing [72-74]. Unlike single mode fiber where the core located within 60 μm of the fiber, the flat cladding surface of D-shaped fiber is usually less than 10 μm from the fiber core, which makes it more accessible for the functionalization process. In our work, a D-shaped fiber with core diameter around 9 μm was utilized. The fiber core is located approximately 4 μm beneath the flat cladding surface and the same doping of SMF-28 is applied.

15-cm section of the D-shaped fiber was first etched by buffer oxide etchant solution to remove the top cladding until the exposed the fiber core (figure 28(a)). The MOF-Polymer solution with MOF weight ratio of 1 was utilized in the coating. The fabricated sensor is shown in the figure 28(b) with the D-shape fiber being outlined. The diameter of the coated sensor is around 100 μm, and the optical fiber has some shift towards the center of fabricated sensor.

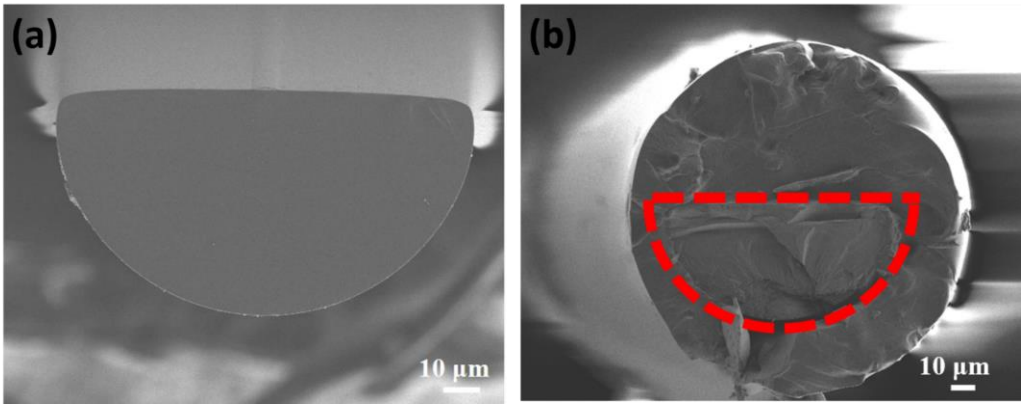

Figure 28. (a) Etched D-shape fiber, (b) Cross-sectional view of the fabricated sensor based on D-shape fiber.

Methane gas with the concentration ranging from 100% to 1% was introduced into the measurement chamber at room temperature. The same nitrogen gas resetting process was also applied. The time-dependent response of the sensor is recorded and plotted in the figure 29. In the figure, a well-defined trace with the similar trending for transmitted light as compared with MMF was obtained in response to methane exposure, which confirmed the sensitivity of the D-shaped fiber-based sensor and the functionality of the coating matrix across all the fiber platform. Besides, it is also worth noting that the output power variation of the D-shaped fiber when exposed to 50% methane gas is 15% as compared with 24% for the MMF sensor with the same level of gas exposure. The decrease of the output power change might be resulted from the reduced evanescent wave interaction caused by the shrinkage of interface area.

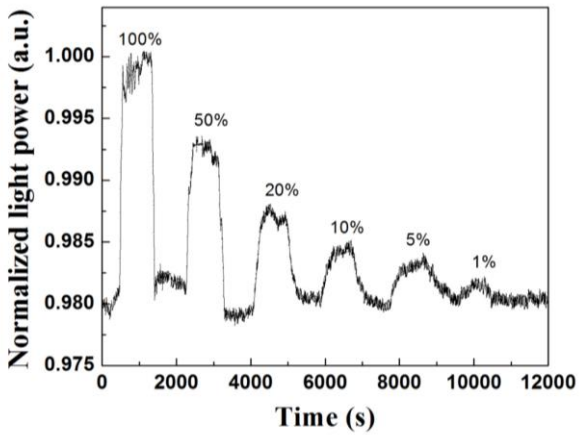

Figure 29. Time-dependent response of sensor based on D-shaped fiber.

The repeatability of the D-shaped fiber was also characterized by introducing of multiple cycles of methane flux with concentrations ranging from 1% to 100%. The time-dependent sensory profiler is plotted in figure 30.

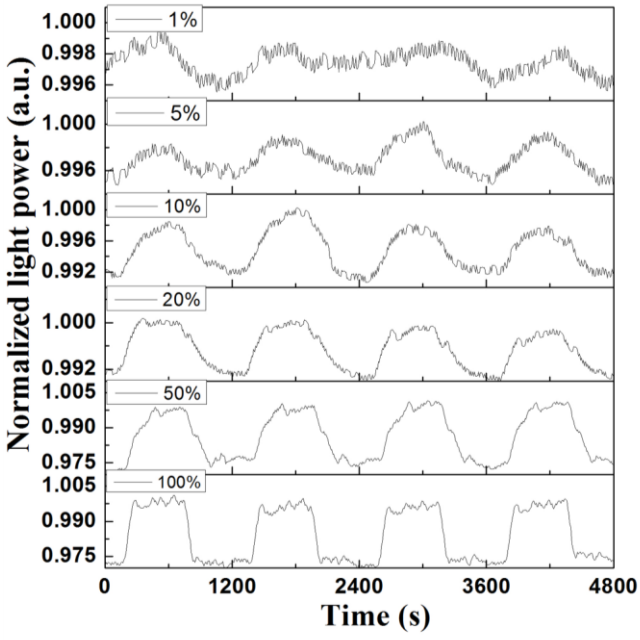

Figure 30. Response of the D-shaped fiber to multiple cycles of methane gas with various gas concentrations.

In the figure, a repetitive response of sensor to methane gas exposure with the concentration above 10% is observed. The power variation under pure methane cycles is less than 3%, indicating a very repeatable trace. A gradual increase of the intensity variation upon lower concentration of methane exposure is in accordance to the previous results of MMF. Although the transmitted power fluctuates around 10% when the sensor is subjected to methane gas with the concentration of 1%, the sensor is still capable of differentiating the methane levels as low as 1% due to the relatively large intensity change upon 1% methane exposure that can be distinguished even with slightly increased gas level of 2%.

In summary, we developed a scalable and low-cost fiber optical methane sensor based on MOF-Polymer functional coating as the new fiber cladding. The prepolymer composition was optimized in term of the mechanical and optical property. Meanwhile, the MOF to polymer weight ratio was also adjusted for the enhancement of the sensor performance. The optical sensor shows a repetitive and reversible response with the gas detection limits of 1%. The effects of coating thickness and length were also investigated to fully understand the sensory behavior. D-shaped optical fiber was also utilized in combination with same functional coating to fabricate single-mode methane sensor. A comparable sensory performance was achieved in terms of the gas detection limits, repeatability and reversibility, confirming the robust and universal of the functional coating for methane sensor development.

4.0 Optical Hydrogen Sensor Based on Metal Alloy Functionalized Nanocones

In this chapter, we present our work of developing fiber optic sensor for real-time monitoring of the hydrogen gas. The optical sensor is based on the nanocone-textured D-shaped fiber followed by pallidum gold thin film functionalization. The enlarged surface-to-volume ratio of the sensory film on top of the optical fiber accommodates more active sites for gas interaction and generates an accelerated sensing speed with the response time being shorten by 3-4 times as compared with the sensor without nanostructures. Meanwhile, the introduction of nanostructure underneath the thin functional film could effectively alleviate the accumulated internal stain during multiple cycles of gas exposure, which helps to improve the repeatability and reversibility of the sensor upon continuously gas exposure. The highly controllable VLSI microfabrication scheme in this chapter for the fabrication of textured fiber surface provide a low-cost and compatible solution for other optical sensing applications.

4.1 Overview

Hydrogen gas has been extensively researched due to the increasing demand of the clean energy to address the serious environmental challenges worldwide including pollution and global warming. The only byproducts generated during the hydrogen combustion process is water, which makes it an ideal energy source. The initial effort of utilizing hydrogen gas as major energy source for the combustion engine in the automobile instead of the traditional fossil fuel has been deployed. The large-scale implementation of hydrogen industry requires close monitoring of infrastructure

during all phases of applications including gas storage and transportation since the wide flammable concentration range from 4% to 75% can be easily met when gas is leaked. Meanwhile, the low ignition energy of 0.017 mJ could also create huge safety concerns when exposes to oxygen gas [75, 76]. The above issues introduced by the large deployment of the hydrogen gas requires fast, low-cost, and reliable sensing metrologies for gas monitoring.

Palladium functionalized sensors, benefiting from its high solubility and detection limits, have been intensively studied [77-79]. The formation of PdH and its corresponding phase transition from α to β during the presence of the hydrogen gas resulted in elevated Femi level and reduction in reflectivity of the sensory thin film, which serves as the fundamental principle for most hydrogen sensing applications [80]. However, researchers found that this phase transition yields significantly slow response when exposed to the low hydrogen concentrations (0.1-0.2%), and the Pd alloys such as PdAu with high alloy concentration (above 17%) can prevent this phase transition, thereby producing an accelerated response [80]. Moreover, saturation of the signal change was also observed in serval literatures for sensors with Pd sensing film in response to hydrogen gas with the concentration over 3% [81-83], which could be problematic for the gas detection upon higher hydrogen levels. In this chapter, we will present our work of developing optical hydrogen sensor utilizing PdAu sensing film with the atomic ratio of 1.2.

Although optimization of the sensory material was confirmed to be effective in accelerating the sensory response, the bulky PdAu alloy films still has the limitation of the slow diffusion rate and bucking effect resulted from built-up stress [83, 84]. To further improve the sensing speed, hydrogen sensors based on nanostructures and nanomaterials were developed [85-88]. A pronounced increase in the sensory response and sensitivity was confirmed for those nanostructure-based sensors. Most of the sensors are based on characterization of electrical

resistance of the sensory material, which resides some safety concerns due to spark generation [89]. Fiber optical sensor is considered as an alternative solution owing to its distinguished property such as the high resilience to environmental variation and stability under harsh environment. Besides, fiber optical sensor has the potential for remote and distributed sensing, which could substantially broaden the applicable scenarios for the hydrogen sensing. There are increasing papers that combines the nanomaterials with optical fiber [90-92]. However, most of the nanomaterials is expansive to synthesis and has poor attachment to the fiber surface, limiting its practicability for large-scale applications.

In this work, a new fabrication scheme compatible with current VLSI approach was presented to create nanostructure on D-shaped fiber. The metrology utilized in this work is based on the evanescent wave absorption, which basically monitors the optical transmission power variations as a consequence of the modification of the sensor film properties such as the refractive indices after exposure to hydrogen gas [91, 93]. Nanocones were manufactured by adjusting reactive ion etching (RIE) conditions without any masking layer. Compared with traditional approaches such as electron-beam lithography [94, 95], electrodeposition into nano-frame [96-98], pulsed laser deposition [99], electrochemical step-edge decoration [100, 101], our fabrication process provides a more convenient and less expensive approach. The sensing material of PdAu alloy is then sputtered-coated on the nanocones on top of the fiber surface after RIE process. The response time of sensor upon gas exposure with varied concentrations was reduced by two thirds compared with reference counterpart with continuous functional film. Meanwhile, the stability and response speed of the sensor were also investigated as a function of sensing film thickness and temperature to fully understand the sensory behavior.

4.2 Sensory Fabrication

D-shaped fiber with a core dimension of 9 μm and distance between core to upper cladding of 3.5 μm was specially made through D-shaped platform utilizing the conventional fiber fabrication approach. The core of D-shaped fiber has the same doping as SMF-28. The fabrication process is sketched as inset in figure 31(a). 7-cm section of optical fiber was initially subjected to the buffer oxide acid by Transene for 16-min to etch away the upper cladding. The processed fiber was fixed on pure silica glass as the flat-cladding facing upwards. The sample was then introduced to the Trion RIE system. Mixture gas of CHF_3 (30 sccm), SF_6 (10 sccm) and inert gas of Ar (100 sccm) was utilized to produce the byproduct of the polymer radicals at pressure of 200 mT, which serves as the sacrifice mask to generate the nanostructures [16]. The processing time was optimized to 80 min as the RIE power fixed at 100 W. The etched fiber was then immersed into solvent (acetone, ethanol, and deionized water) to clean the polymeric residue before metal alloy functionalization. Thin PdAu film with molecule ratio of 1.2 was coated on the surface of optical fiber by sputter coater (Denton TSC). The pressure of sputtering chamber was adjusted to 5.3×10^{-3} mTorr. Argon gas was initialized as the carrier gas during the deposition process.

Fabricated D-shaped fiber sensor was characterized by Zeiss SEM to observe the topography. Cross-sectional view of the sensor with 15-nm PdAu thin functional coating was shown in figure 31(a). Outlined area is the fiber core, of which top 2-μm region has been etched away to expose more core area for large interface between the fiber core and sensory film. The sensor surface was further zoomed in and presented in figure 31(b) with the enlarged cone structures as the inset. The nanocone array were characterized to be around 100 nm in height. The dimension of the nanocone was less than 60 nm. Although there is small variation of the exact size of the cones, most of them falls into 50-nm range with good uniformity. Besides, the distances

between cones varies within 100 nm. The distribution of the sensing film could have significant impact on the performance of the sensor and needs to be particularly investigated. In our work, we utilized transmission electron microscopy (TEM) with probe of Cs being corrected to study the PdAu film distribution on top of the nanocones. High angle angular dark field (HAADF) observation of the fabricated nanostructure is shown in the figure 31(c). A thin film of metal layer was observed on top of the nanocones across the whole fiber surface. Meanwhile, it is easy to note that the coating thickness appears to be nonuniform across the whole sample, which, in this case, is caused by the cutting angle variation of the sample that produces partially, merely, and totally-cut nanocones by the focus ion beam during the sample preparation. To further investigate the metal alloy distribution, energy-dispersive X-ray spectroscopy (EDS) mapping was performed to study the element distribution on top of the nanocones. The mapping spectrum is shown in figure 31(d). The bright area in the top figure corresponds to the Au and Pd element as yellowish spectrum, further confirming the previous observations. The atomic ratio of Pd to Au was calculated to be 1.4, which is way beyond the weight limits that can eliminate the phase transition.

In order to measure the time-dependent profiler of the fiber optics sensor, transmitted output power change in response to the hydrogen gas exposure is monitored and plotted. The measurement setup is shown in figure 32. A broadband source (Er-doped, EBS-7210) working between 1515 nm and 1615 nm was utilized as the input light source. Pure hydrogen gas was diluted by pure nitrogen at specific flow ratio controlled by the mass flow controller. The mixed gas was then introduced to testing chamber with flow rate fixed to 20 sccm. The output signal was measured through a semiconductor photodetector in real-time which attaches to a data collection card. The whole experiment was carried out at room temperature.

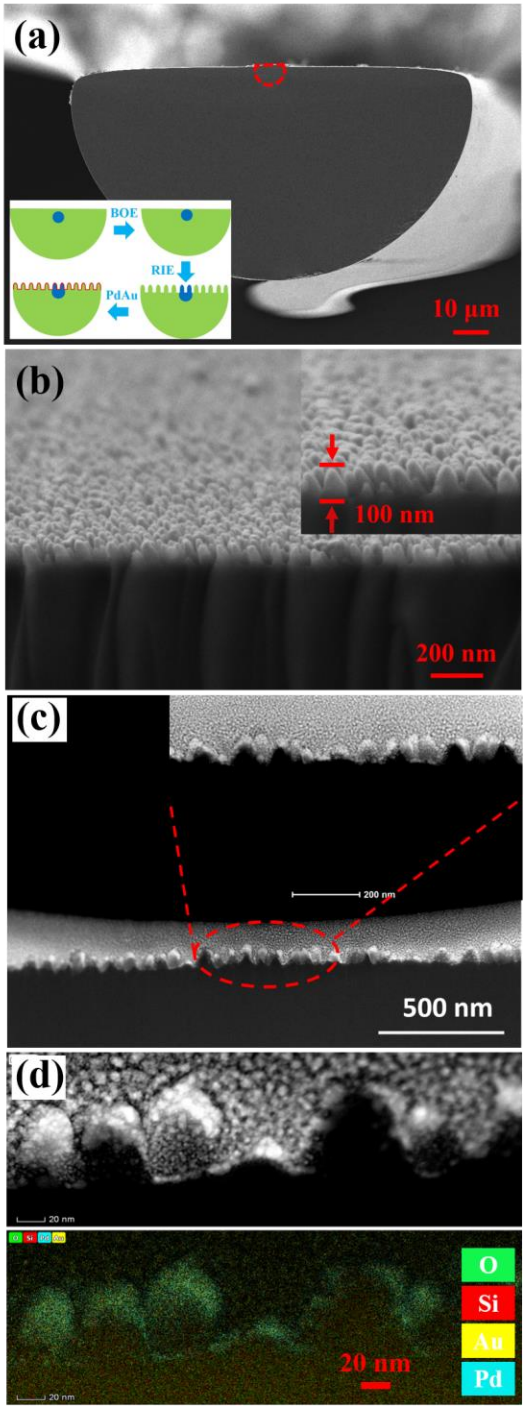

Figure 31. (a) Cross-sectional view of the coated fiber with fiber core being marked by red circle, inset describes the whole sensor manufacturing process, (b) image of the fiber surface, enlarged view is shown in the inset, (c) the distribution of the metal alloy on top of the nanocones by TEM, inset shows the magnified image, (d) top figure shows area selected for EDS mapping, and bottom figure shows the mapping result.

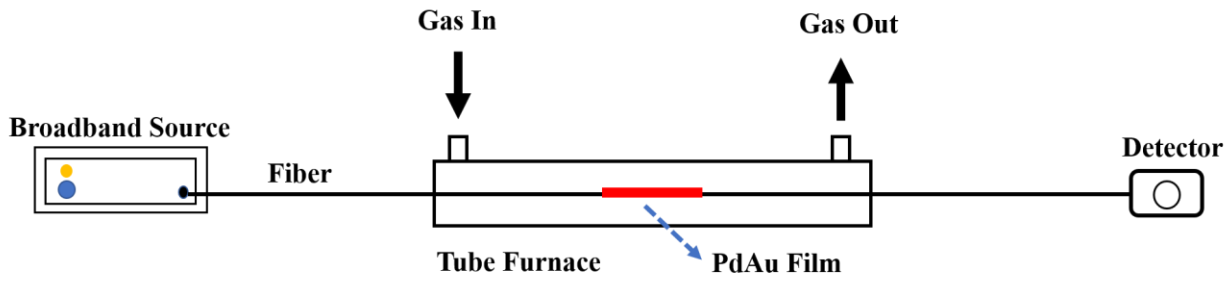

Figure 32. Setup for sensor characterization.

4.3 Sensory Characterization

The time dependence of the output power responding to hydrogen fluctuations at room temperature is plotted in figure 33(a). Similar as the sample textured by nanostructure, the fiber without nanocone undergoes the same etching process with the exact remaining thickness and metal alloy was coated on the etched surface. Gas mixture with various concentrations has been introduced to the test chamber continuously through 10-min cycles without any resetting process (flux of pure nitrogen) after each testing cycle, which, in fact, has higher requirement of senor in sensitivity, stability. The black line in the figure shows the response of senor without nanostructure-textured surface to the hydrogen exposure with gas level between 10% and 0.25%. While the transmitted power change in accordance with the gas fluctuations, for example, output light increase (decrease) regarding to the related hydrogen rise (fall), the response can no longer be differentiated within hydrogen concentrations after 3 intervals. Besides, the response profile is also quite noisy with large signal fluctuation under the same concentrations. On the contrary, the response of sensor based on nanostructure-textured surface (red line) presents a smooth signal trace responding to the same gas levels, which demonstrates the potential of the sensor for fast

continuously measurement. In fact, reliable response profile with better sensitivity was also observed by both electrical and optical hydrogen sensors with nanostructures and nanomaterials [75, 85, 88, 99, 102]. The non-responsive behavior of the reference sensor after several cycles is mainly resulted from the accumulated internal stress when the functional coating is continuously subjected to hydrogen environment, deteriorating the mechanical property of the sensory film to the degree that it can no longer able to react to the gas fluctuation as confirmed by previous literatures [83, 84, 103].

The instability of reference sensor in response to hydrogen absorption of various concentrations is mainly associated with the degradation of mechanical properties such as delamination, buckling and cracking [103] upon hydrogen up taking and unloading. The extent of sensing film deterioration is proportional to the built-in stress introduced by functional film and Zhao [104] has improved the sensory stability and reversibility by alleviating the compressive stress of the sensing film through thermal annealing process. Nanostructure has also been proven and extensively utilized as interlayer structures for the alleviation of built-in internal stress for thin film growth [105], which helps to explain the more stable response of the sensor with sensing film deposited on top of nanocones instead of flat and continuous surface.

Another point worth investigating is the output power change. The maximum output power changes in response to hydrogen exposure for both sensors are relatively small: 2% power variation associated with nanostructure-textured sensor, and only 1% was introduced by the sensor without nanostructure. Compared with pure Pd functional film, sensing film consists of PdAu metal alloy undergoes a shrinkage of the lattice dimension with the introduction of the gold element, which, in turn, reduces the interstitial site available for gas accommodations. Meanwhile, noncatalytic Au, when compared with noble metals, has relatively lower hydrogen solubility and

resulted in the less absorbed hydrogen molecules [106]. It is easy to notice that the output power change of nanostructure-textured surface is significantly larger than that of the reference sensor, indicating a more significant interaction between the evanescent wave and functional film. The improved sensory performance can be explained by the improved surface-to-volume ratio of the nanocone structure and the expansion of thin film when exposed to hydrogen gas. Unlike traditional flat and continuous films, film deposited on top of nanocones has enlarged space available for film expansion in volume and sectional direction, which further enables it to accommodate more hydrogen molecules.

Another fact that cannot be neglected when utilizing nanostructure in optical device, especially optical sensing device, is the attenuation loss introduced by the Rayleigh scattering during the interaction of nanocone with coupled light. The extent of the scattering is related to the nanostructure dimension and density. Rayleigh scattering, in fact, can be suppressed for nanostructure-textured surface as long as the average period of the nanostructure array is within the dimension of $\lambda/\pi n$ [107]. In our case, the broadband source utilized in the experiment has a wavelength range between 1515 to 1615, and the refractive indices of the fiber core is 1.45. So, the calculated minimal period to avoid significant scattering of the nanostructure is around 330 nm, which is far above the observed average period of < 100 nm for our sample, indicating a less significant scattering of nanocones in our case. The same observation of limiting scattering through adjusting the nanostructure dimension was also investigated and confirmed by the previous experimental results [16].

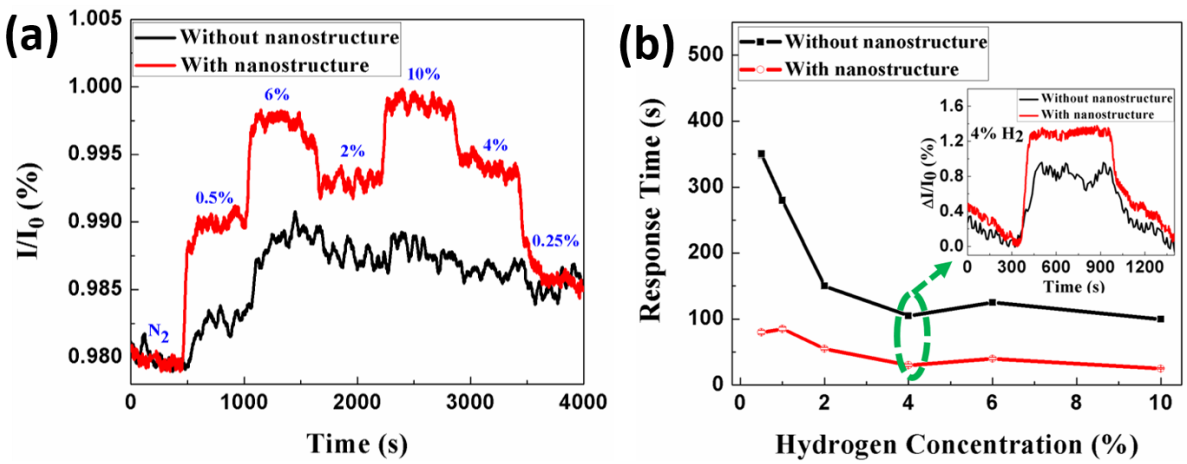

Figure 33. (a) Response of the sensors with and without nanostructures to various hydrogen concentrations, (b) response speed of those two sensors. Inset shows the sensing profiles of those two sensors upon 4% hydrogen exposure.

Response time, as well as sensitivity and stability, is also essential in evaluating the sensor performance. In order to further analyze the effect of nanocone structures on sensing speed, both sensors were investigated by the presence of the same hydrogen concentrations with recovery process induced by pure nitrogen influx after each hydrogen cycle and the response speed is shown in Figure 33(b). The response time is defined as the time taken for the sensor to increase its output power to 90% of its maximum value within hydrogen cycle. It can be seen from the figure that the sensor textured by nanocones achieves accelerated response when compared with the reference sensor. The response time required upon hydrogen exposure with concentration of 10% and 0.5% for sensor with textured surface is only 1/4 of the one without, for example, around 100 s for the reference sensor compared with 25 s for the sensor with nanocones after exposing to 10% hydrogen. Besides, the response time of sensor to the hydrogen exposure within those two concentrations was also shorten to approximately 1/3 of previous level. Inset depicts the time-dependent response of sensor to 4% hydrogen exposure, in which the transmitted signal for the

sensor with nanostructures is much more stable with accelerated responding time of only 30 s compared with 105 s for the reference sensor. The comparison of time-dependent behaviors of those two sensors in response to other hydrogen levels such as 2% and 10% is shown in the figure 34, and the same trend was observed in both cases. The diffusion rate of gas to coating film was usually considered as limiting factor in the sensor response speed and it is mainly affected by the coating thickness and temperature. The diffusion rate for nanocone-textured fiber sensor and reference sensor is supposed to be the same due to the same coating thickness and characterization temperature. Actually, surface-to-volume ratio is proven to be the limited factor in determining response speed for the sensor with nanostructures and nanomaterials [97]. In fact, the accelerated response speed was observed for most of the hydrogen sensor with nanostructures. The underlying mechanism is quite straightforward [75, 88]: compared with the continuous sensing film, film deposited on nanostructures can exceedingly increase the sensory film surface area. The enlarged surface-to-volume ratio leads to the denser Pd distribution, providing more sites available for the absorption of the hydrogen molecule. Moreover, it also facilitates the accessibility of hydrogen gas to the site, leading to the accelerated formation of PdH during the absorption process.

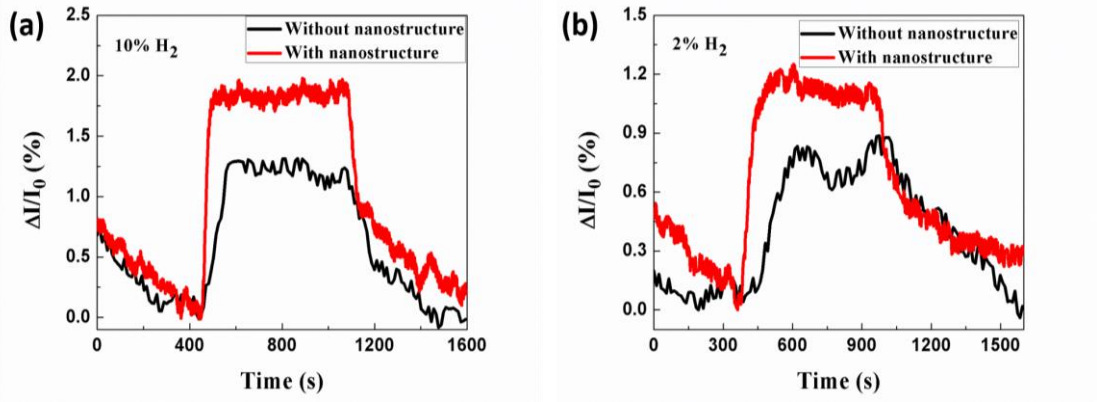

Figure 34. The response of the sensor to both 10% (a) and 2% (b) hydrogen exposure.

In addition to the response speed, sensors with repeatable and reversible response are also essential for gas sensing. Herein, multiple cycles of mixture gas were introduced to the gas chamber at room temperature followed by nitrogen flux to reset the sensor back to its initial level in terms of the output power intensity. The results upon various hydrogen concentrations are summarized in figure 35(a). As can be seen in the figure, the stability of sensor varies upon different gas exposures as indicated by the gas intensity variations among each cycle. For instance, a relatively small output power variation of 2.2% was obtained during the multiple cycles of hydrogen exposure of 10%. The variation of the signal further increases to 5.4% when exposed to the lower level of the hydrogen gas with 1% concentration.

It is easy to notice that there is a major drop in initial the recovery process of the sensor and then this trend starts to compromise as the slopes of the traces slow down, indicating a non-uniform gas desorption process from β-PdH [104]. The increased surface-to-volume ratio of the functional coating on textured-surface, as expected, introduces an accelerated desorption process as compared with the continuously coating, which, as a result, largely accounts for the initial recovery process [88]. When the Pd hydride transition on nanocone is accomplished, the less significant desorption of the continuously films located within nanocones starts to become more significant. It is worth noticing that the hysteresis phenomenal, referring to the irreversible behavior of the sensor resulted from the structural variations [83], has been significantly alleviated as the transmitted signal of the sensor resetting back to the initial status after nitrogen exposure. The enhancement of sensing performance in terms of reversibility and repeatability can be accounted for the introduction of both nanostructure and Pd alloy sensory film. In this case, the PdH phase transition occurring at lower hydrogen concentration can be avoid. The built-in internal stress that can potentially degrade sensor performance will be alleviated through introduction of

nanostructures. To address the slow response issue, the introduction of oxygen gas during the resetting process can speed the recovery process of the sensor due to the formation of intermitted by-products PdO [102, 108].

The transmitted power variation upon the hydrogen exposure with various concentrations is plotted in figure 35(b). When the sensor was characterized in the hydrogen environment with lower concentration of 0.25%, the output power change is only 0.5%; the output power gradually increases to around 2% when the hydrogen gas concentration was raised to 10%, which was within expectation and in accordance with previous observations.

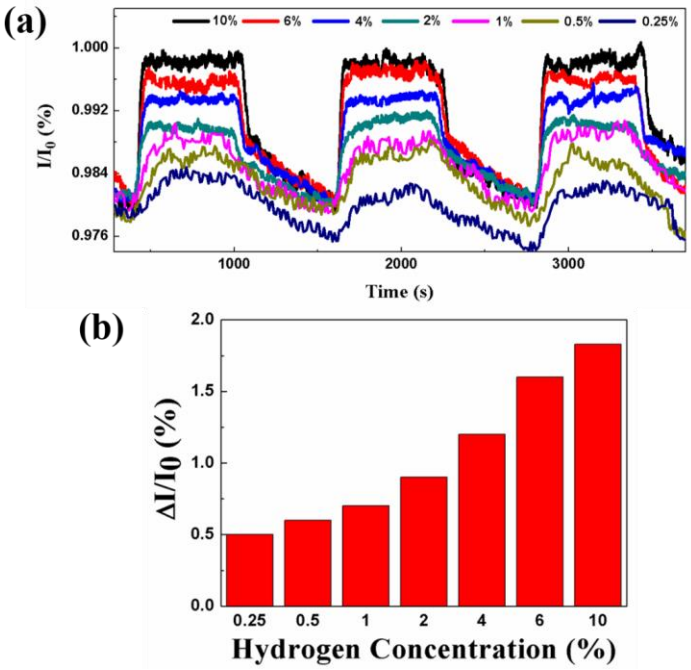

Figure 35. (a) Time-dependent response of sensor to repeative cycles of hydrogen with concentration up to 10%, (b) corresponding output light power variations.

The sensory film thickness is a non-neglecting factor that is worth investigating for the comprehensive understanding of sensor design and behavior. Herein, two hydrogen sensors are

fabricated, and the functional film coating thickness was adjusted to 30 and 60 nm. Response speed of the sensor was calculated according to previous method and the response time of those sensors in response to different hydrogen concentrations were calculated and plotted in figure 36(a). Response time of original sensor with 15-nm coating thickness was also plotted for comparison. As shown in the figure, the response time increases when the coating of functional film becomes thicker. The observed experimental results were in good agreement with other literatures for both electrical and optical sensing applications[109]. The working principle might be associated with the decrease of surface-to-volume ratio introduced by thick coating layers [97]. The non-neglecting film thickness of 30 and 60 nm when compared with the small cones (100 nm) with narrow gaps (less than 100 nm) decreases the curvature of the topography, forming a sensory film with reduced surface-to-volume ratio. Meanwhile, thicker film, compared with thinner one, needs longer time for the hydrogen gas to diffuse through, which will also contribute to the increased response time. Inset shows the time-dependent response of the three sensors with various coating thickness to hydrogen exposure with 4% concentration. The response of the sensor functionalized by thin sensory film tends to be more stable than thicker ones, which is in a good agreement with the previous results. The output power change was found to be increasing with thicker coatings. This is associated with increasing active sites for PdH formation. The response of the sensor to hydrogen gas with the concentration of 2% is also illustrated in figure 36(b).

The investigation of sensor's behavior with elevated temperature was also performed. Sensor with 15 nm sensing layer was heated up to 40, 80, and 120 ℃ by a tube furnace with an accelerating rate of 1 ℃/min and the time-dependence response of the output power upon same hydrogen measurement sequences is shown in figure 37. A slightly decrease of the output power change is observed when the sample is heated to 80 ℃ compared with 40 ℃. This reduction of

transmission power with elevated temperature is due to the reduction of the sensing film solubility [80]. Meanwhile, the output power in response to 0.25% hydrogen gas increases gradually and the power mismatch between 0.5% and 0.25% hydrogen become less apparent as temperature increases from room temperature to 80 ℃. When the temperature stabilized at 120 ℃, the response of sensor to the last two hydrogen cycles with the concentration of 4% and 0.25% can no longer be distinguishable with previous response any more, indicating a degradation of sensitivity and performance. This behavior might be resulted from the severely degraded hydrogen solubility as well as accumulated internal strain of the sensory film at higher temperature that generates more significant deformation of functional film after initial test cycles.

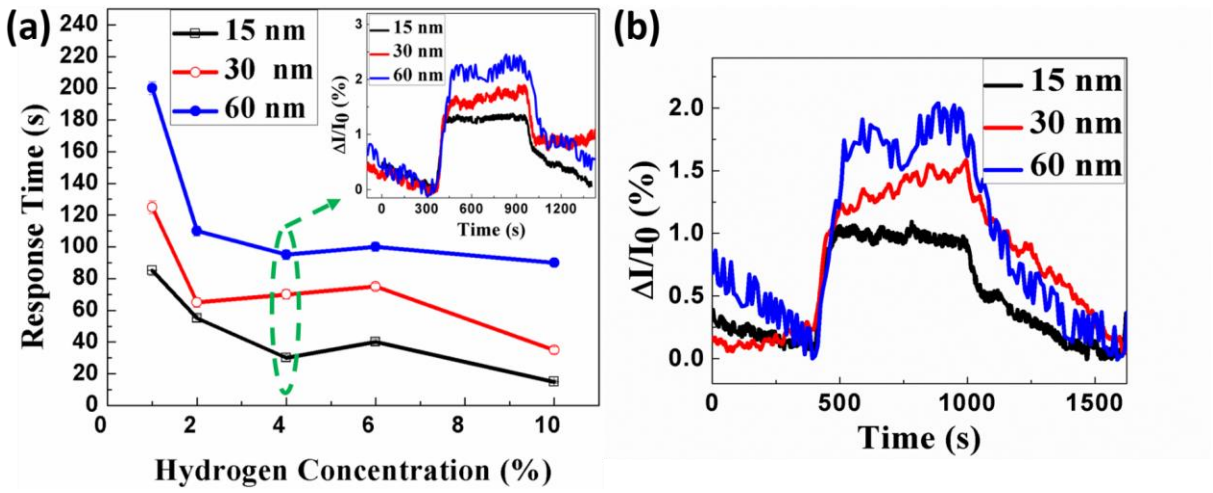

Figure 36. (a) Response time versus gas concentration when varies the coating thickness of the functional film, the response of sensors with various coating thickness to 4% (inset) and 2%(b) hydrogen gas.

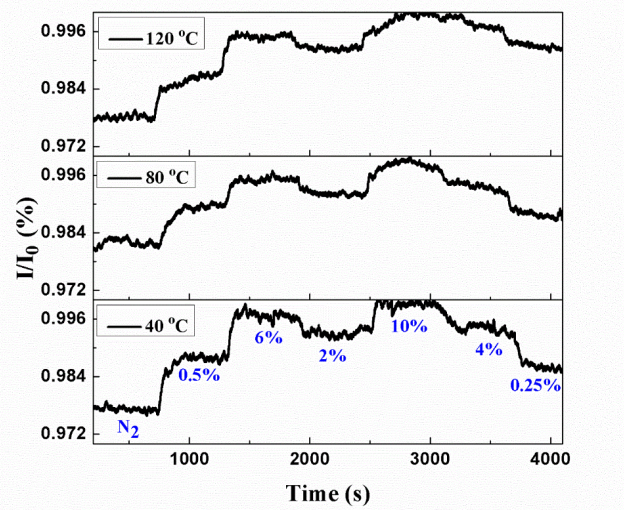

Figure 37. Sensory response at elevated temperatures upon hydrogen exposure with various concentrations.

In summary, we fabricated nanocone structures on D-shaped fiber and functionalized them with PdAu alloy thin film for fiber optical hydrogen sensing in this chapter. In comparison with reference sensor without nanocones, sensor with sensory film coated on nanostructures achieves more stable responses as well as accelerated response speed. Furthermore, sensory film thickness was proven to have a major factor in determining the response speed, and the elevated operational temperature can also affect sensor stability.

5.0 Optical Sensors Based on Fabry-Perot Interferometer

Fiber optical sensor based on Fabry-Perot interferometer (FPI) has great potential for chemical monitoring due to the high sensitivity, small form factor, large dynamic range, and fast response speed. In this chapter, we will present our work of developing fiber optical sensors for hydrogen and methane gas detection based IFPI. Distributed hydrogen sensing at room temperature was also achieved with high spatial resolution of 5-mm and detection limits of 1%. Meanwhile, methane gas detection was also performed, and distinguishable cavity length change was observed upon gas exposure with varying concentrations. A repeatable and reversible response was also performed during the measurement. Moreover, an IFPI sensor was introduced to the harsh environment with operating temperature around 750 ℃ for the monitoring of hydrogen gas for fuel cell applications, the slope of the responsive trace was calculated and utilized as an indicator for different hydrogen levels.

5.1 Overview

Optical sensors based on FPI have been extensively investigated for various sensing applications, for example, the pressure monitoring [110], humidity measurement [111], strain measurement [112], and temperature sensing [113]. The response of the sensor is based on the cavity length change induced by the environmental change. In which, the light reflected from the two mirrors of the cavity recombines and forms the interference fringes. The intensity of the interference light is a function of the phase difference of the two-split beam, providing the

metrology of monitoring the cavity length variations by demodulating the interference spectrum. Most of the sensors were fabricated utilizing fiber optics in order to reduce sensor dimension and improve the resilience of the sensor to harsh environment including high temperature and electromagnetic interference.

In terms of the cavity formation, FPI sensor can be categorized into two types: the intrinsic and extrinsic. Most of the extrinsic cavities consists of two independent fiber pieces with an air gap of specific distance which were bonded together to form a cavity. Multiple approaches have been adopted to create extrinsic FPI cavity including the adhesive gluing [114], thermal fusion [115], and electrical fusion [116]. Although FPI sensor based on extrinsic cavity has been widely implemented, the complicated fabrication process limits its repeatability of the cavity length as well as the sensor performance for large-scale applications. Besides, thermal coefficient mismatch between multiple materials such as the glass fiber and polymer glue could be problematic for high temperature applications. The high coupling loss introduced by extrinsic cavity could not be neglected, which prevents the deployment of series of FPI cavities in one fiber for distributed measurement.

To address those issues, IFPI sensors based on intrinsic cavity were developed. The intrinsic cavity was fabricated inside the glass fiber, which can effectively resolve the issues introduced by extrinsic cavities. In this work, we presented our work of developing gas sensors based on the intrinsic cavities. The cavities were formed by the two Rayleigh enhanced point in optical fiber. The enhancement of Rayleigh scattering to 40-50 dB was introduced by femtosecond laser writing, which provides an easy, highly sensitive, low-loss, and low-cost approach for IFPI sensor development. In this chapter, three optical sensors were fabricated to monitor the hydrogen, methane gas at room or high temperature with the utilized of intrinsic cavities in combination with

functional coatings, for example, Pd thin film for hydrogen detection at room temperature, MOF-Polymer coating for methane gas detection, and Pd-doped metal oxide thin film utilized for hydrogen monitoring at high temperature.

5.2 Hydrogen Sensor at Room Temperature

5.2.1 Sensor Fabrication

Standard single mode SMF-28 was utilized in the experiment. The fiber was initially cleaned in the solvent (acetone, methane, and deionized water), and further dried in nitrogen gas flow. The thoroughly cleaned optical fiber was then mounted on moving stage followed by laser irradiation for the manufacturing of enhanced Rayleigh scattering point. The detailed fabrication process can be referred to figure 17(a) of chapter 2. 14 Rayleigh enhanced points were inscribed onto optical fiber core to form 7 IFPI cavities. The distance between each cavity is around 5-mm and the cavity length increase from 489 μm to around 2 mm with a step of 200 nm. The profiler of Rayleigh enhancement can be characterized by OFDR system (OBR4600), and the result is shown in the figure 38(a). In the figure, the intensity of Rayleigh inscribed points appears to be uniform with an enhancement of 45 dB on average. Laser processed optical fiber was transferred into e-beam evaporation chamber (Thermionics) with first two cavities being covered by Kapton tape, and thin layer (10-nm) of Cr was deposited on top of the fiber followed by 500 nm Pd deposition. After the initial deposition, the fiber was rotated by 180 degree and the same metal film was deposited onto the remaining area of fiber surface. The fabricated sensor has 5 sensory cavities for gas monitoring and other two cavities with the length of 489 μm and 684 μm serving as reference.

The cross-sectional view of the fabricated sensor is shown in figure 38(b). In the figure, the whole fiber surface is covered by Pd thin film. Although the coating thickness is not uniform across the whole fiber, most of the area has been covered by the film with the thickness around 500 nm.

In addition to the distributed sensor, a point sensor was also fabricated with 2 sensory cavities. The length of the cavity is around 484 and 1686 μm, respectively, and same coating has also been applied to this sensor.

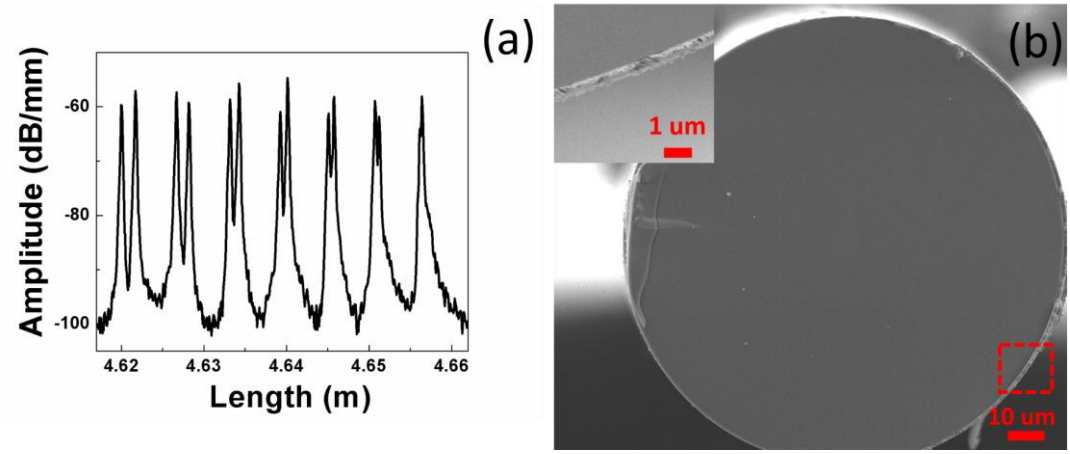

Figure 38. (a) OFDR spectrum of the Rayleigh enhanced points in optical fiber, (b) Cross-sectional view of the optical fiber, inset is the enlarged area (red rectangular) of the Pd thin film.

The experimental setup is illustrated in figure 39. A broadband source (Exalos) with the center wavelength of 1550 and tunable range of 60 nm was utilized as the light input during the test. The light was coupled into optical fiber with functionalized film through a circulator, and the backscattered light was collected and analyzed by a spectrometer (BaySpec). The hydrogen gas was delivered into the test tube with concentrations between 0.25% and 10% at room temperature. The gas flow was fixed to be 20 sccm.

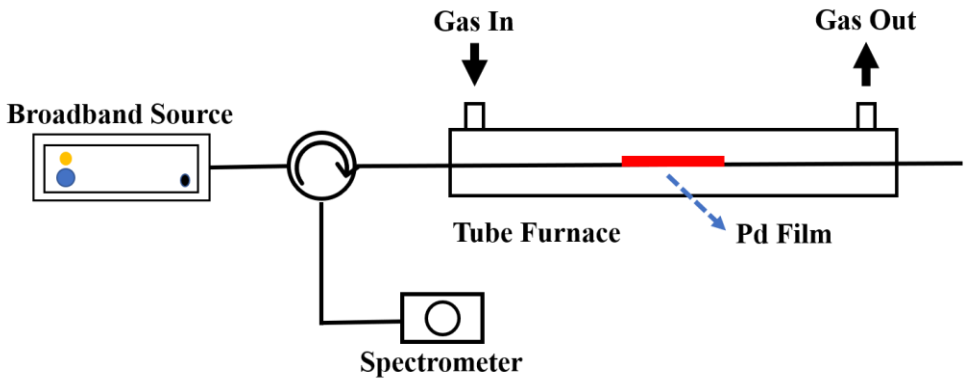

Figure 39. Schematic of experimental setup.

5.2.2 Sensor Characterization

The spectrum of interference backscattered-light is recorded by the spectrometer and illustrated in figure 40(a). In the figure, well-defined fringes with good contrast ranging from about 1505 to 1590 nm was observed, which indicates the stronger interference of the backscattered light and good enhancement of the Rayleigh scattering. The demodulation process is implemented by fast Fourier transform followed by Buneman frequency estimation of the interference spectrum to roughly extract the fringe orders. A more sophisticated estimation was then performed in combination with the total phase calculation approach to generate a more accurate fringe order, which, when in combination with optical path difference, could provide the absolute information of the cavity length [117-119], and the result is shown in figure 40(b).

The time-dependent response of the sensor to various hydrogen concentrations is shown in the figure 40(c). In the figure, cavity length of the sensor increases as exposed to the hydrogen gas. The expansion of fiber is in proportional to the gas concentrations. A significant expansion of 22-nm and 80-nm was obtained for cavity 1 and cavity 2, respectively, when exposed to hydrogen gas with concentration of 10%. As the gas concentration decreases, the cavity length expansion

reduces as well for both cavities. For example, when exposed to hydrogen gas with concentration of 4%, the expansion of cavity is reduced to 17% and 14.8%, respectively. A further decrease of the cavity length change is within expectation when we introduce lower concentrations of hydrogen gas such as 0.25%. However, the responses of the sensor can still be differentiable even when subjected to lower concentrations.

The underlying mechanism of the increased cavity length can be explained by the Pd lattice constant expansion as exposed to the hydrogen gas. The lattice constant change as well as the volume increase has been observed and quantified in many literatures [120-123]. The diffused hydrogen molecules inside the Pd thin film generates a tensile mechanical stress, which transfers onto the elastically rigid fiber optical substrate through a shear force. Once the stress introduced by the hydrogen gas is balanced by shear stress at one point, the deformation of the glass fiber will occur [124], expanding the Rayleigh enhanced cavity length. The tensile strain is a function of the hydrogen partial pressure, and can be quantified by Sievert's law [125]:

$$\varepsilon = \frac{0.026\sqrt{p}}{k} \tag{5.1}$$

where p is the hydrogen partial press, k is the Sievert coefficient (350 $Torr^{1/2}$).

The relationship of gas partial pressure and the number of gas molecules can be described as:

$$pV = \mathrm{nRT} \tag{5.2}$$

From the above equation, the gas partial pressure is linearly proportional to number of the gas molecules. The gas flow was fixed in our experiment, so the partial pressure is in fact related to the gas concentrations.

Figure 41(a) shows the relationship between the ratio of hydrogen concentrations and the ratio of tensile strain when exposed to various hydrogen concentrations in referring to the reference gas level of 0.25% and the corresponding tensile stain. The tensile strain can be calculated by the ratio of the cavity length change ΔL to the original cavity length L. The inset shows the trace of square root function of the gas ratio in terms of reference gas level of 0.25%. In the figure, a good agreement of trace was observed for the concentration ratios (black line) and measured cavity length change ratio (blue rectangular and red dot) when the sensor is exposed to lower hydrogen concentration of less than 6%, which matches very well the description of the equation 5.1 and indicates an elastic response of the sensor under lower hydrogen levels. However, as the hydrogen concentration is increased to 10%, the tensile strain change ratio cannot follow the concentration ratio for both cavities indicated by the enlarged mismatch in the figure. The underlying mechanism of this behavior is still unknown. One possible reason might be associated with the release of accumulated internal stress through the generation of cracks or delamination phenomena that alters the elastic interaction between the Pd thin film and glass fiber so that the optical fiber cannot response to the internal stress linearly under high levels of hydrogen gas exposure.

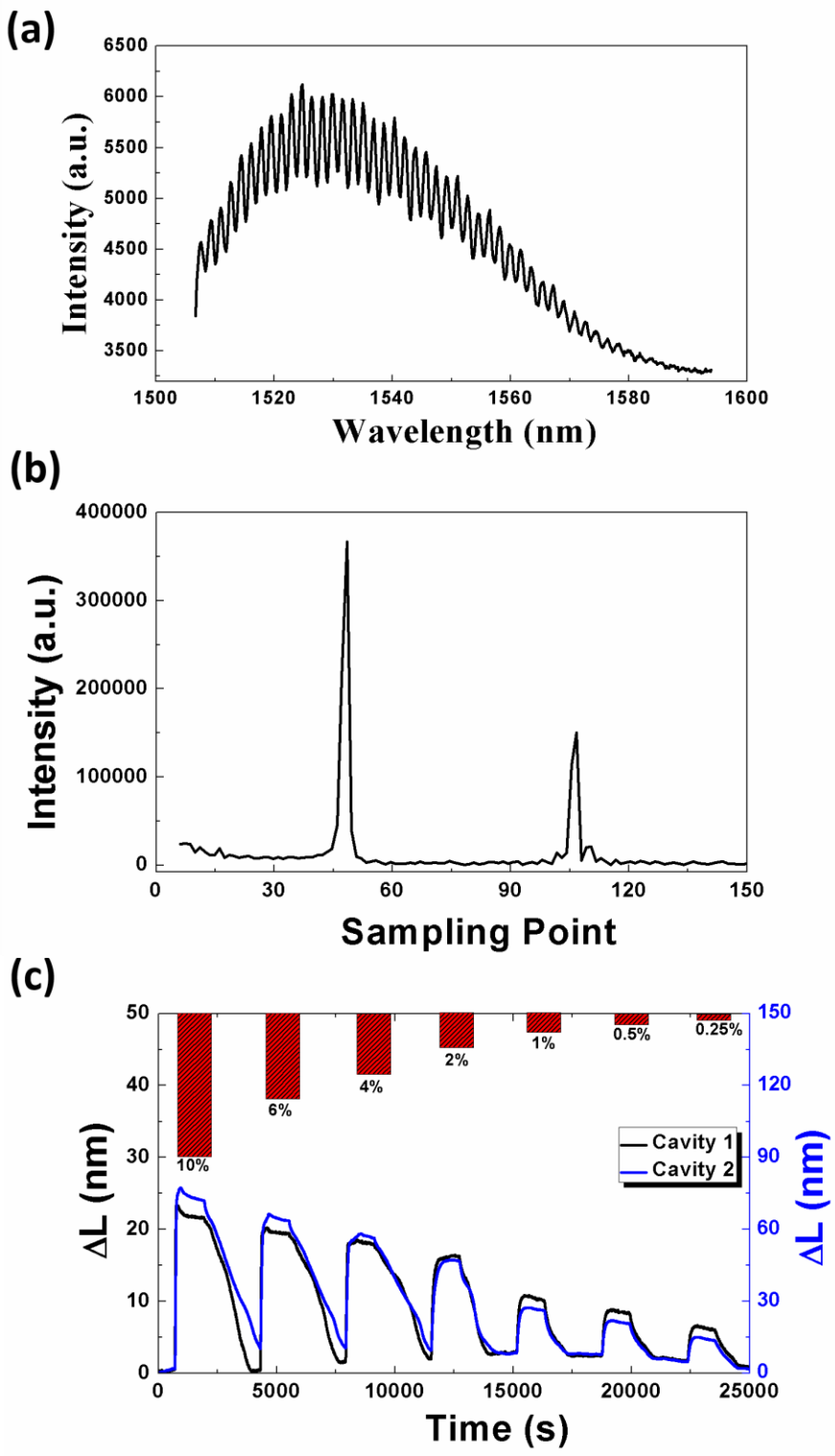

Figure 40. (a) Interference spectrum of the point sensor, (b) demodulated spectrum of the sensor, (c) time-dependent response of the sensor to various hydrogen concentrations.

The sensory speed is also crucial in determining the performance of the sensor especially for the application of explosive gas monitoring. In this work, the response time of IFPI sensor is plotted in figure 41(b) in referring to various hydrogen concentrations, and it was calculated as the time duration when the output power reached 90% of its maximum value.

In the figure, the response time increases gradually for both sensors when the hydrogen concentration decreases from 10% to 0.25%, for example, the response time required for the cavity 1 and 2 upon 10% hydrogen exposure is 24 s and 54 s, respectively. However, sensor response slows down as the time required for both sensing points to react to hydrogen exposure with a concentration of 0.25% increases to 175 and 170 s, respectively. Meanwhile, the error range also bumps from around 4 s to more than 15 s for both cavities, which can be better understood by the less well-defined response of the sensor to the lower hydrogen concentrations. The decrease of the response time referring to the enlarged gas concentrations, can be easily explained by the gas diffusion process. The more concentrated gas provides an enlarged hydrogen partial pressure, which accelerates the gas diffusion into Pd film to form PdH, resulting an increased response speed. Besides, it is also worth noting that the response speed varies for these two cavities, and the mismatch enlarges when the gas concentration increases. The mismatch might be associated with the variation of the Pd film thickness above those two cavities. When exposed to hydrogen gas with low concentrations, the coating thickness is not a limiting factor since the gas can only penetrates the film with limited distance below the surface, and the number of Pd crystals involved in the PdH formation is not significantly different. However, when further increases the gas concentrations, the effects of film thickness start to become a dominated factor in the process due to the deeper diffusion of hydrogen gas. To be more specific, the time required for signal of the

sensor with thicker functional coating to saturate is significantly longer than the thinner one, which generates different response speed and enlarged gas of the responsive traces of those two cavities.

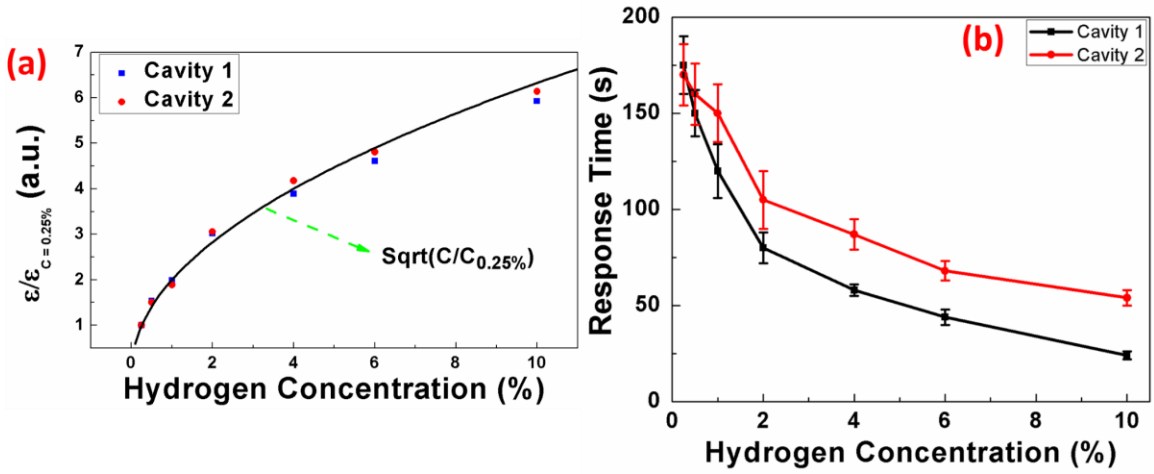

Figure 41. (a) Tensile strain ratio in response to gas concentrations in referring to the hydrogen level of 0.25%, inset is fitted curve, and (b) response time of the two cavities upon hydrogen exposure with various concentrations.

The repeatability and reversibility of the IFPI sensor was also investigated by introducing multiple cycles of hydrogen gas followed by the nitrogen flux as the resetting process to fully understand the sensor behavior. The targeted gas flow was kept as the previous level of 20 sccm. The experiment was carried out at room temperature, and the response of sensor to the gas concentration of 0.5% and 2% are shown in the figure 42.

In the figure, a good reproduction of the trace was obtained for both concentrations upon multiple cycles of the hydrogen exposure. For example, the cavity length change varies within 1.5% when the sensor is operated under hydrogen gas of 2%, indicating a highly repeatable response of the sensor. When reduced the gas concentration to 0.5%, a slightly increase of 3% of the cavity length variation occurs, which still performs well reproducible response. Meanwhile, the sensor can also be reset back to its initial level for both traces during nitrogen gas exposure.

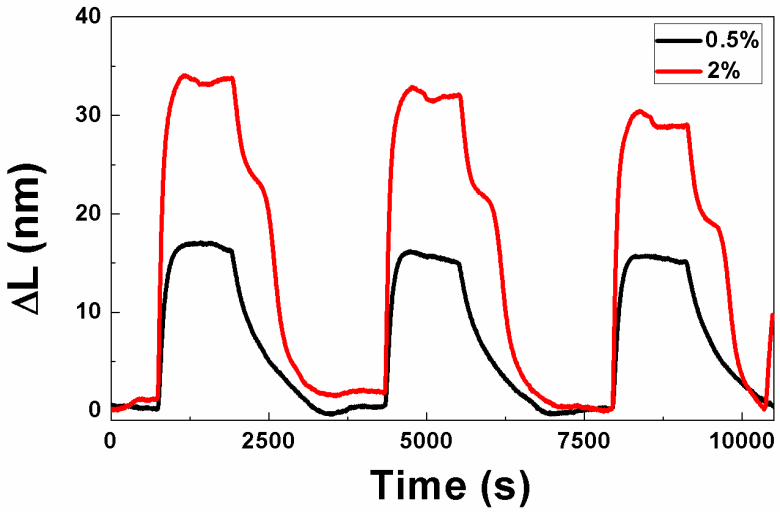

Figure 42. The time-dependent response of the point sensor to multiple cycles of hydrogen gas with the concentration of 0.5% and 2%.

The interference of the distributed IFPI sensor with 7 sensory cavities is shown in the figure 43(a). The large contrast of the interference fringes indicates the good cavity quality. The demodulated cavity profiler of the sensor is shown in the figure 43(b). Seven cavities were detected in the spectrum with the length ranging from 489 μm to 1875 μm.

To characterize the profiler of distributed sensor, a mixed hydrogen gas with concentrations ranging from 0.5% to 8% was introduced into the tube furnace. The gas flow was tuned to 20 sccm and the experiment was carried out at room temperature. The time-dependent behavior of the sensor upon hydrogen exposure is plotted in the figure 43(c). In the figure, the first two sensors with the cavity length of 489 μm and 684 μm were utilized as the reference sensors since there is no Pd functional film coating on top of those two cavities. No significant response was observed for those two sensing points during the whole measurement. This result not only confirms the functionality of the Pd thin film but also eliminates the interference of other parameters in the experiment such as the temperature. The response of other cavities with Pd coating upon gas

exposure were plotted as curves from the sensor 3 to sensor 7. A well-defined sensory profiler was observed for all the cavities with detection limit of 1%, indicating the functionality of multiplex sensor with the spatial resolution of 5-mm.

The calculated tensile strain for each cavity under various gas exposure was shown in the figure 43(c). A gradually increase of the tensile strain was observed with increasing gas concentrations which meets our previous observations of figure 41(a). Meanwhile, the tensile strain distribution under the same gas level is quite uniform when exposed to lower level of hydrogen. A small increase of the non-uniformity was observed when the gas level reaching to 10%, which is with expectation. Overall, the tensile strain distribution meets the description of equation 5.1.

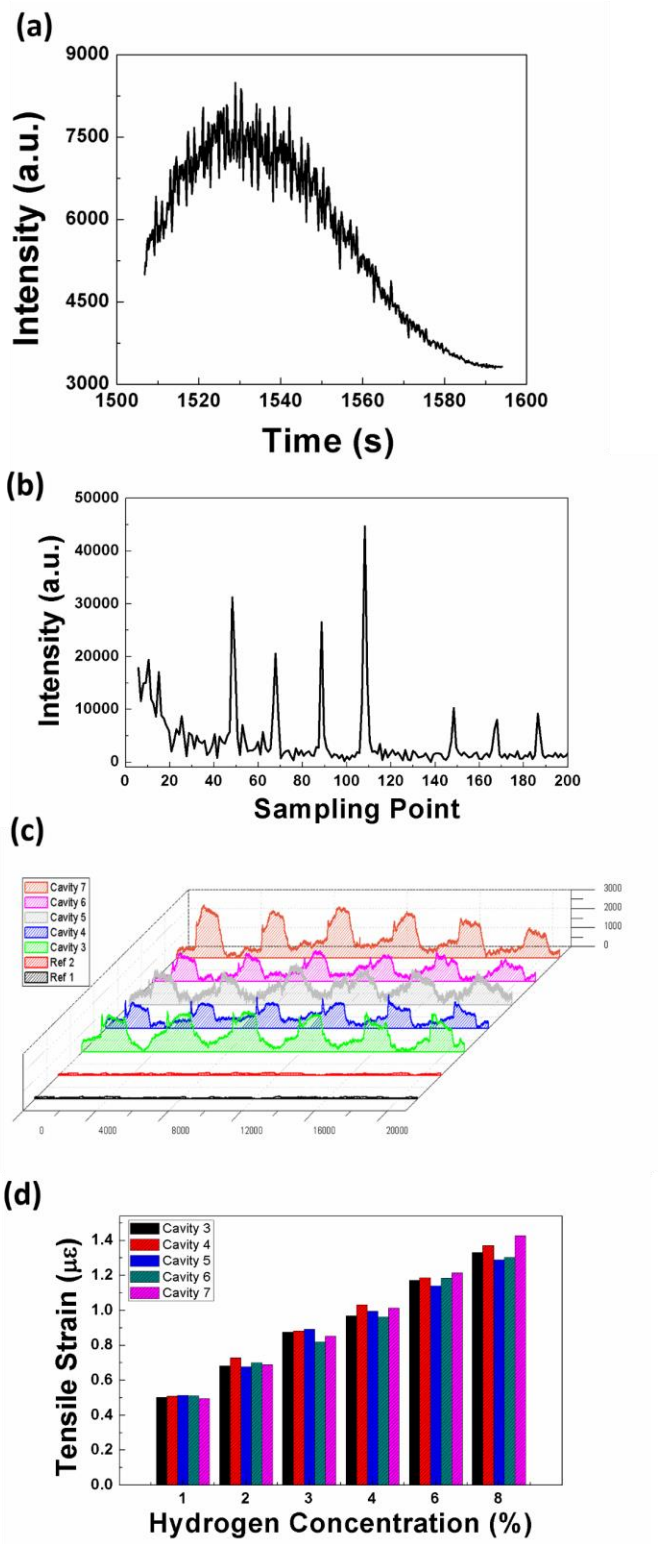

Figure 43. (a) The interference spectrum of the distributed sensor, (b) the demodulated profiler, (c) the time-dependent response, and (d) tensile strain profiler of the multiple sensors to hydrogen gas exposure.

5.3 Hydrogen Sensor at High Temperature

5.3.1 Overview

Fiber optical sensor has been intensively explored for hydrogen gas applications at room temperature or lower operating temperature (< 300 ℃). In addition to conventional scenarios, hydrogen gas has also been utilized in fuel cell for the energy harvest. Most of the fuel cell operates at high temperatures, typically over 700 ℃, which is way beyond the temperature limit of the traditional electrical sensor. Optical fiber, made of the slightly doped pure silica, can be resilient to the harsh environment, especially high temperature. Multiple efforts have been deployed for the development of the optical sensor for chemical detection under high temperature [21, 126, 127]. Most of the sensors operates relying on the evanescent wave interaction with the sensory material and can only be utilized as a point sensor. To increase the interaction, most of the optical fiber was first etched using highly erosive solutions to expose the fiber core before functional material coating, which will introduce tremendous loss during the light coupling, and prevent the sensor from large scalable manufacturing and long-distance applications.

To address this issue, we fabricated IFPI optical sensor for high temperature hydrogen monitoring. Pallidum doped metal oxide deposited on top of optical fiber through sol-gel process was utilized as the functional coating as described in the literature [21]. The IFPI cavities was fabricated using the same ultrafast laser irradiation. The response of the sensor, cavity length change rate in particular, is proportional to the hydrogen concentrations, which could be utilized as a distributed sensor with multipixel of cavities. Besides, the cavity length change can be quite repeatable when exposed to multiple cycles of hydrogen gas with same concentrations. No saturation of signal was observed in the experiment, and detailed explanation will be presented.

5.3.2 Sensor Fabrication and Characterization

The standard SMF-28 single mode fiber was utilized in the experimental. The 15-cm section of polymer jacket of the fiber was first striped away followed by the solvent cleaning with acetone, methanol, and deionized water. The IFPI cavity was then fabricated through femtosecond laser irradiations according to the description of the section 5.2.1. The interference pattern of the Rayleigh backscattered light on optical fiber is recorded by a spectrometer and shown in figure 44(a) with good contrast of the fringes. Meanwhile, the length of the fabricated fiber cavity was demodulated to be 458 μm and demonstrated in the figure 44(b). Pd-doped TiO_2 thin film was utilized as the sensory material and coated onto the optical fiber by sol-gel method [21]. The cross-sectional view of the IFPI sensor is shown in the figure 44(c). The functional film appears to be uniform across the optical fiber and the coating thickness is estimated to be around 1 μm. Inset shows the enlarged image of the film. The densely-packed nanocrystals aggregates with each other and forms the functional coating.

The experiment was carried out utilizing the same setup as figure 39. Before the measurement, the tube furnace was pre-heated to 750 ℃ with a step of 4 ℃/min and stabilized for 1 h with pure nitrogen purge to create nitrogen atmosphere. Hydrogen gas with various concentrations was then introduced to the testing chamber for 20 min followed by 40 min of the nitrogen gas to reset the sensor at each testing cycle. The gas flow was fixed at 20 sccm during the measurement.

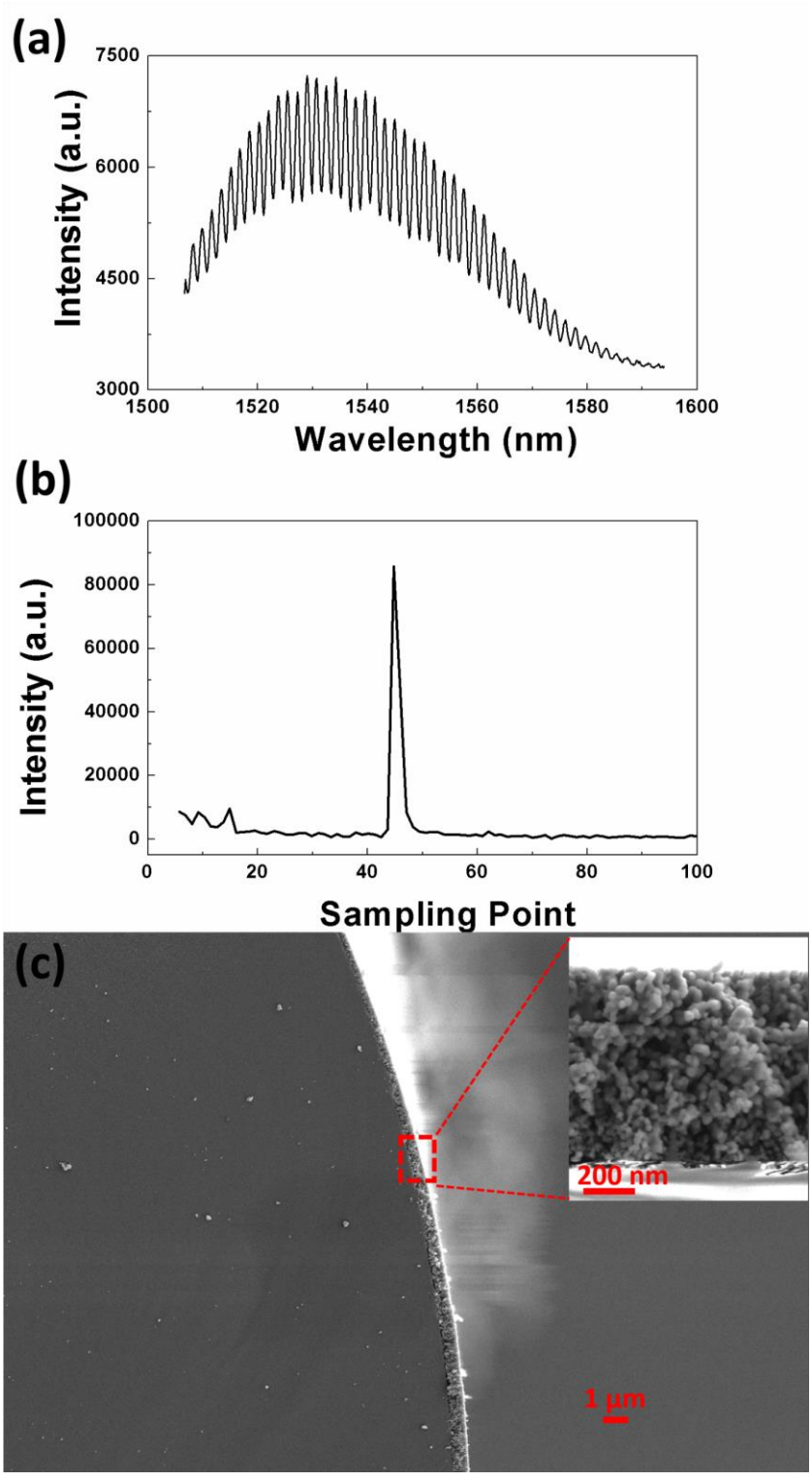

Figure 44. (a) Interference pattern of the laser processed cavity, (b) demodulated cavity spectrum, (c) Cross-sectional view of the sensor, inset is the enlarged Pd-TiO_2 film.

The cavity length change in response to the hydrogen gas exposure with various concentrations is shown in the figure 45(a). In the figure, the cavity length varies according to different gas concentrations. For example, less than 5-nm of the fiber expansion was obtained for the hydrogen exposure with the concentration of 0.5%. The expansion becomes more significant with increased gas concentrations. More than 20-nm of the fiber was stretched due to the accumulated internal stress when the fiber is measured using 6% hydrogen gas. The rate of the cavity length variation is shown in the figure 45(b). It is easy to note that the accelerated cavity length change rate was obtained in responses to the more concentrated gas exposure.

The cavity length increases continuously as long as the hydrogen environment is not altered. No saturation of the signal was observed as indicated by the inset of figure 45(b) when the fiber was exposure to 3% hydrogen for almost 1 h. The reason might be due to the degradation of the elastic expansion process. The optical fiber becomes soft when exposed to high temperature, reducing the Young' modulus. The accumulated internal strain generates a shear force that cannot be balanced due to the reduced Young's modulus, stretching the optical fiber continuously as a result. Meanwhile, a slightly decrease of the cavity length was obtained when the sensor was exposed to the nitrogen gas for 40 min as shown in the figure 45(a). The reason why the sensor cannot reset back to its initial cavity length is due to the inelastic behavior of the fiber at high temperature, which indicated the non-reversibility of the sensor under this circumstance.

The repeatability of the sensor was also characterized by the introduction of the multiple hydrogen gas cycles of 3%, and the time-dependent response is illustrated in the figure 45(c). In the figure, the traces of the sensor under each cycles of the hydrogen gas parallels with each other, indicating the repeatable response of the sensor to the multiple cycles of hydrogen exposure. The slope of the sensor response could be utilized as the indicator for hydrogen gas detection.

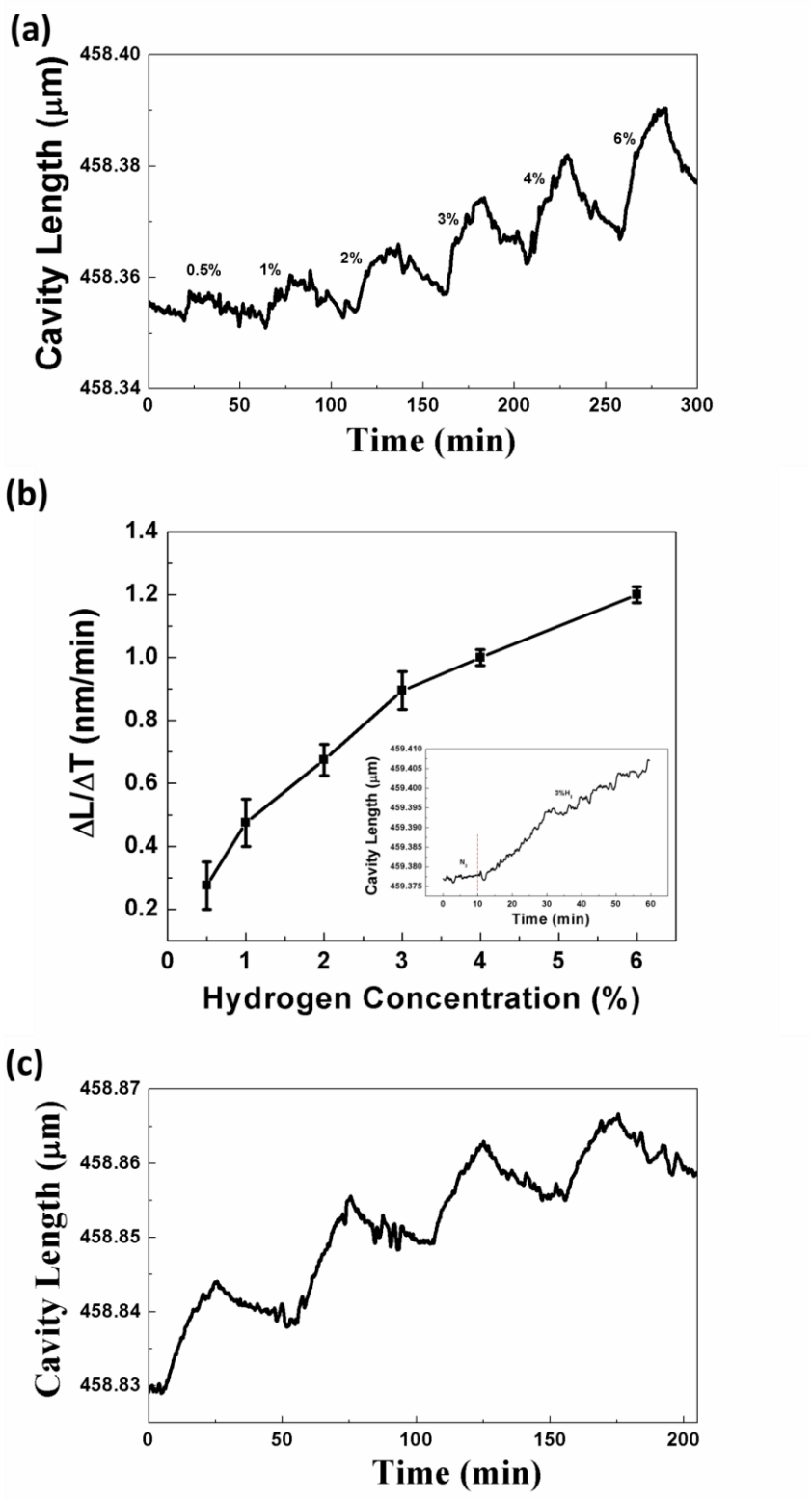

Figure 45. (a) Time-dependent cavity length and (b) the slope of the cavity length change in response to varied hydrogen gas exposure, (c) response of the sensor to multiple cycles of hydrogen gas of 3%.

5.4 Methane Sensor

In addition to hydrogen sensors, we also developed the IFPI sensor for the measurement of methane gas at room temperature. The same MOF-Polymer functional coating with the MOF to Polymer ratio of 1 in chapter 3 was applied in this work. However, compared with previous multimode and D-shaped fibers, the standard SMF-28 single mode fiber was utilized in this experiment without acid etching, which could be very beneficial for the long-distance monitoring applications due to the reduced transition loss by the light scattering and absorption. Meanwhile, the IFPI sensor has the potential for distributed gas monitoring with the deployment of multiple cavities serving as the distributed sensing points along the optical fiber. As we discussed before, the spatial resolution could be up to 5-mm.

In this work, we did the initial fabrication and characterization of the IFPI methane sensor. The same laser processing method was applied for the fabrication of the sensory cavities. The profiler of the fabricated cavity was characterized by OFDR (OBR 4600) as shown in the figure 46(a). Two Rayleigh backscattering points with a separating distance around 1 mm were enhanced by 50 dB through the ultrafast laser writing, which forms a sensory cavity. The backscattered light creates an interference pattern in the input end of the fiber and being captured by the spectrometer and displayed in figure 46(b). The inference fringes have been demodulated and the cavity length of 1007 μm was extracted as shown in figure 46(c).

The experimental setup is the same as previous IFPI sensors of figure 39. Methane gas mixture with concentrations ranging from 100% to 40% was introduced to the testing chamber with fixed flow of 20 sccm at room temperature.

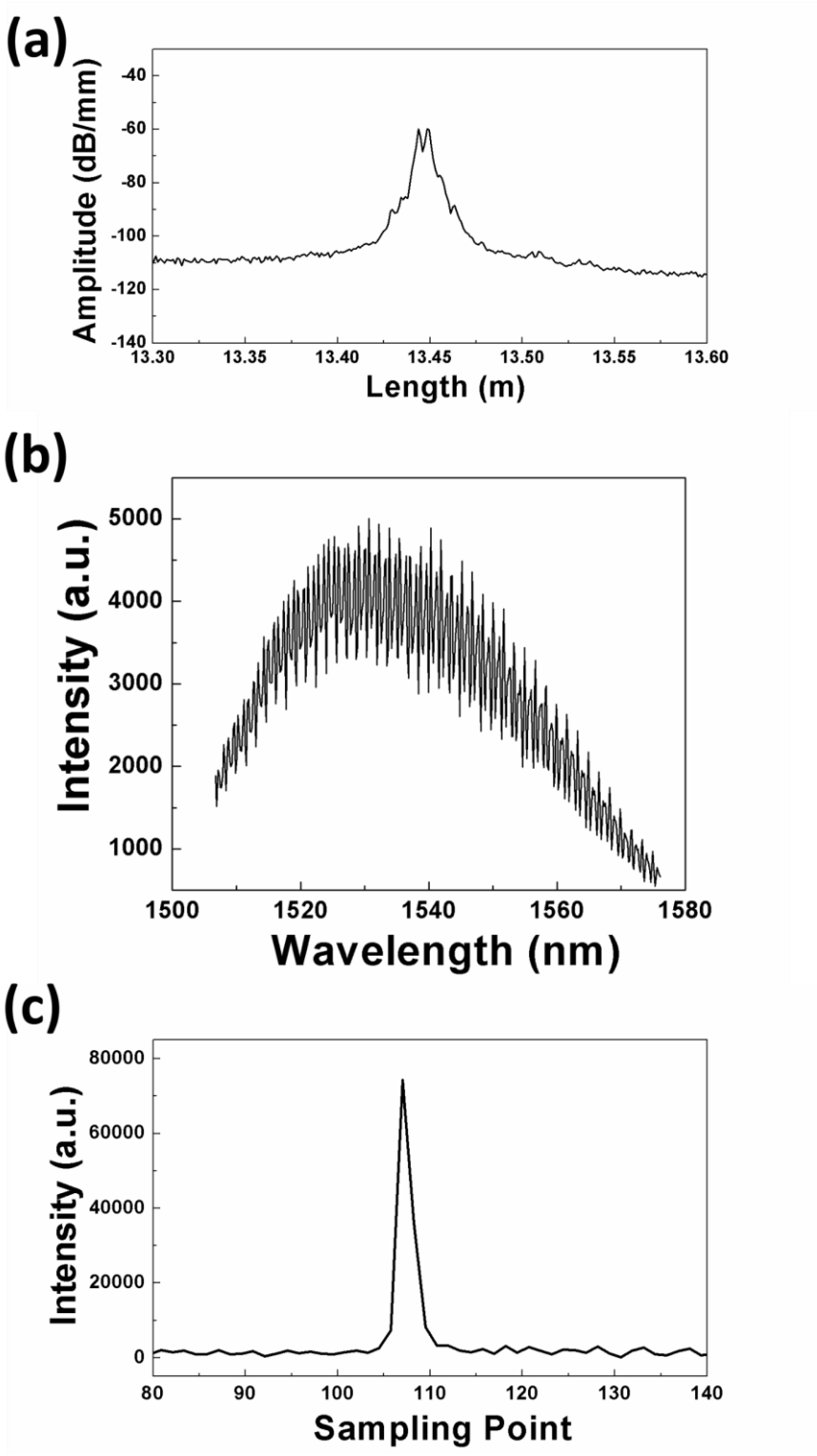

Figure 46. (a) Characterization of the sensor cavity through OFDR, (b) interference spectrum of the sensor, (c) demodulated cavity spectrum.

The cavity length change in response to methane gas with various concentrations is plotted in the figure 47(a). In the figure, the sensor shows well-defined response to hydrogen gas with a detectable concentration up to 40%. Compared with evanescent-wave based sensor fabricated in chapter 3, the detection limit of IFPI sensor is relatively high. Moreover, the cavity length change is quite insignificant as compared with hydrogen sensor (figure 47(b)). The maximum expansion of the fiber caused by pure methane exposure is still less than 1 nm, which is less than 1/20 of the hydrogen sensor. The less significant response might be resulted from the relatively small Young's modulus of the sensory film that produces small tensile strain and the strain cannot be effectively transferred onto the glass fiber. However, the expansion of MOF-Polymer film was first observed in our experiment, which confirms the previous assumptions in chapter 3. It is worth noting that the cavity length fluctuates quite dramatically during the test. The underlying mechanism is still unknown and the internal strain of the MOF-Polymer coating system during the UV curing process might contribute to the observation.

The repeatability and reversibility of the sensor were also investigated through multiple cycles of hydrogen exposure with the concentration of 50% and 100 %, respectively. Compared with the sensory response upon 50% methane gas, a repeatable response for the sensor was obtained for pure methane exposure.

To summarize, in this chapter, we demonstrated three types of IFPI sensor: a distributed IFPI sensor for hydrogen detection at room temperature, a point sensor for hydrogen detection at high temperature, and a methane sensor. Both hydrogen sensors show well-defined response that can be utilized for the distributed or high temperature measurement. The expansion of the MOF-Polymer coating system was first observed in the experiment during the methane test, which could be very beneficial for understanding the behavior of MOF-Polymer based sensor.

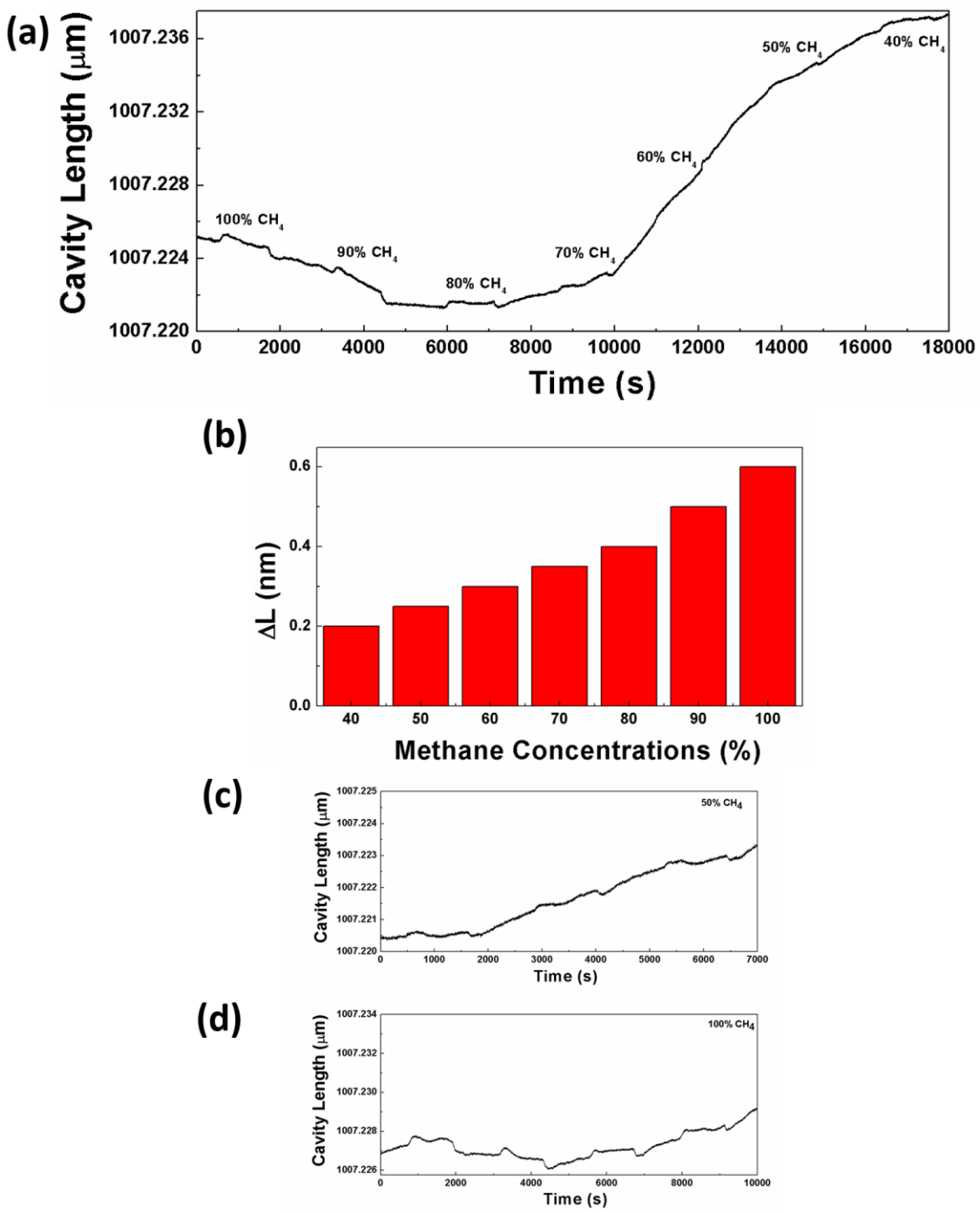

Figure 47. (a) time-dependent response and (b) cavity length change of the sensor to various methane concentrations, response of the sensor to multiple cycles of methane exposure with concentration of (c) 50% and (d) 100%.

6.0 Fiber Optical Distributed Hydrogen Sensor at High Temperature

The distributed hydrogen sensor based on optical frequency domain reflectometry (OFDR) is presented in this chapter. This work utilizes metal oxide thin film as functional material in combination with nanostructures to fabricate fiber optic hydrogen sensor for harsh environment usage. The large surface-to-volume ratio significantly enhanced the light interaction with the sensing material and resulted in improved performance. Meanwhile, the effect of nanostructure dimension on the sensor performance was also investigated in this chapter.

6.1 Overview

Benefiting from the low transition loss, optical fiber has been considered as a great candidate by researchers for distributed sensing applications. In the last decades, multiple distributed fiber sensors have been developed for strain and temperature monitoring based on various mechanism including the Rayleigh and Brillouin backscattering [128-130]. The initial deployment of the technology in the construction industry is mainly based on recording the strain change associated with the structural variations such as the generation of cracks. The successful implementation of optical fiber stimulates great enthusiasm of researchers to tackle even more complicated issues such as the chemical sensing applications. Nowadays methane and hydrogen gas have been utilized as major form for energy source. Methane gas is transferred from the gas well to the custom end by pipelines, which brings the enormous safety concerns. The fast detection of the gas leakage becomes increasing important for the sake of preventing huge financial loss.

Similar as methane, hydrogen gas was widely used in the fuel cell for auto industry. The effective monitoring the hydrogen distribution in the fuel cell is also critical for the debugging of the engine. In 2005, Sumida [131] has presented a distributed optical fiber sensor utilizing Pt/WO_3 as the functional material based on the optical time domain reflectometry (OTDR). The spatial resolution of the sensor is still too low for a reliable point-by-point distribution measurement. In the last few years, our lab has also developed multiple optical hydrogen sensor based on metal oxide (Pd-doped TiO_2), which is capable of operating at 750 ℃ with high resolution and low loss [43, 126, 127]. However, the interaction between evanescent wave and the sensory material is still not significant enough for distributed hydrogen sensing due to low spatial resolution and narrow sensing range. Based on the previous works, in this chapter, we will present our work of developing distributed hydrogen gas sensors by incorporating nanostructures as textured-surface. OFDR was utilized in the experiment for the distributed measurement.

6.2 Sensor Fabrication

D-shaped fiber was used in the experiment with nanostructures fabricated on top of the fiber cladding as shown in chapter 2. The functional material was prepared according to previous works of our group [127]. The prepared solution was diluted by ethanol to achieve a uniform coating on top of the nanostructures. Experimental setup is shown in figure 48, where OBR is used as the OFDR system and a quartz tube furnace is used as the gas chamber. The gas flow was fixed at 20 sccm and the furnace was heated and kept at 750 ℃ before the measurement. The topography of the sensor was characterized by Zeiss SEM system (Zeiss Sigma 500 VP). Meanwhile, an MPB Er^{3+} Broadband source (EBS-7210) with operating wavelength between 1515 nm and 1615 nm

was chosen as the light source. The same semiconductor photodetector was also used for the measurement of transmitted power.

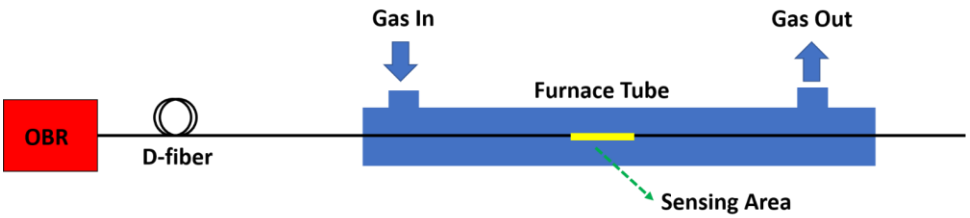

Figure 48. Schematic of experimental setup.

6.3 Sensor Characterization

Topography of the functional coating is shown in the figure 49. In the top view, a uniform sensing layer was formed on top of the nanostructures, confirming the penetration of the sensing material to the gaps between the nanograss, which is further identified by the inset and cross-sectional image. The thickness of the coating is around 700 nm.

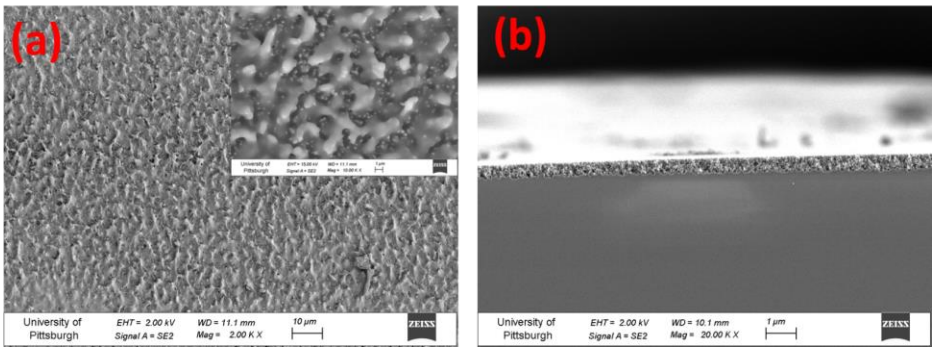

Figure 49. (a) Top view of sensor, inset is the enlarged image, (b) cross-sectional view of the sensor.

The distributed sensory response to various hydrogen concentrations is shown in the figure 50. In the figure, a distinguishable amplitude distribution of the backscattered light is presented in response to hydrogen gas with concentration between 1% and 6%. When the hydrogen concentration is low (0.5%), the response becomes hardly differentiable compared with the result of 1%, which might be resulted from the insufficient PdH formation during the transition. Meanwhile, the backscattered signal intensity upon 10% hydrogen exposure is comparable with the result of 6%, indicating the saturation of sensing film during PdH formation. As a result, the sensor exhibits a wide sensing range from 0.5% to 10%.

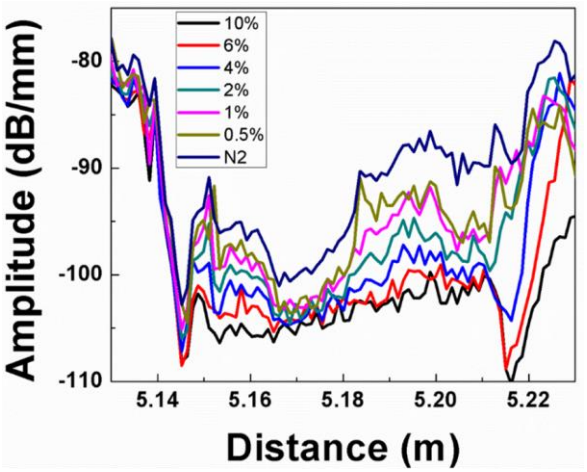

Figure 50. Distributed response of the sensor to various hydrogen concentrations.

To investigate the time-dependent behavior of the distributed sensor upon hydrogen and nitrogen cycles, the backscattered signal level was recorded at different time and plotted in the figure 51. In figure 51(a), the signal level starts to drop around 2.5-min, which is reasonable as time is required for the hydrogen gas delivery through the gas pipeline. However, the whole reaction finished within 30 s as the signal level finish dropping at 3 min. Meanwhile, there is a continuously signal drop from 2.5 to 3 min when exposed to 1% hydrogen, which is within

expectation due to the less hydrogen involvement for reaction. Figure 51(c) and (d) shows the nitrogen resetting cycle after the hydrogen exposure with concentration of 10% and 1%, respectively. It is easy to note that the response of sensor to nitrogen gas upon 10% hydrogen exposure tends to be faster as compared with the resetting cycle for 1% hydrogen, which might be related with the hydrogen penetration depth within different concentrations.

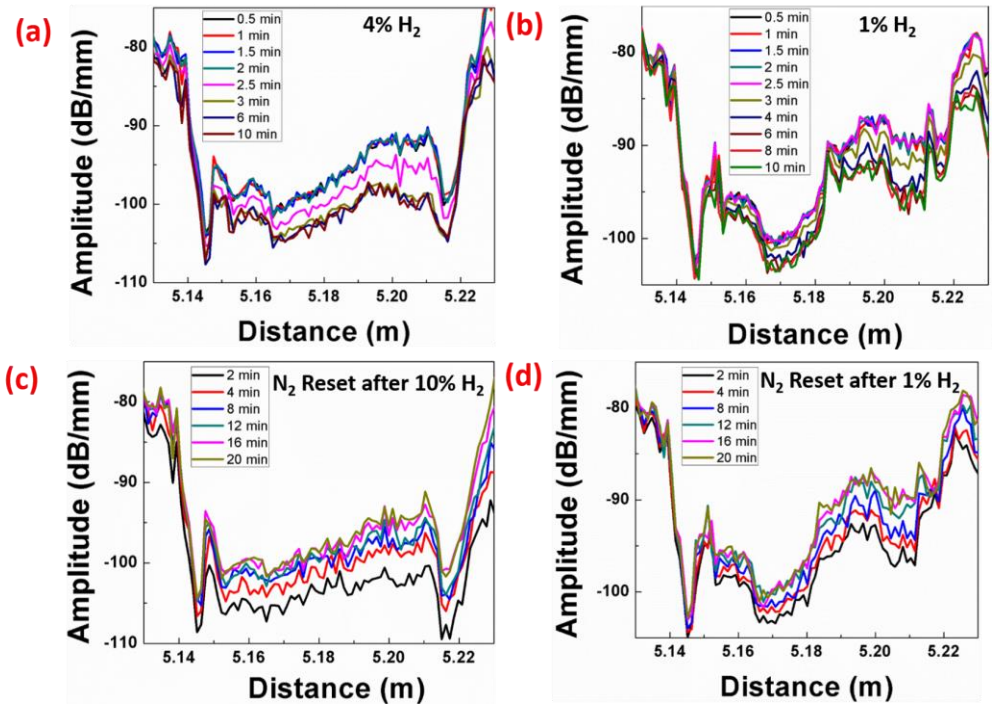

Figure 51. Distributed response of the sensor to (a) 4% hydrogen and (b) 1% hydrogen, nitrogen resetting process after the hydrogen exposure of (c) 10% and (d) 1%.

Finally, the transmitted power change under varied operating temperature is measured and illustrated in figure 52. Compared with previous results [43, 126], the output power change increases from 22% to 35% upon 4% hydrogen exposure even when the thickness of functional coating is reduced by half, indicating that the nanostructures utilized in the sensor significantly improve the sensory response by enlarging the surface-to-volume ratio of the functional coating.

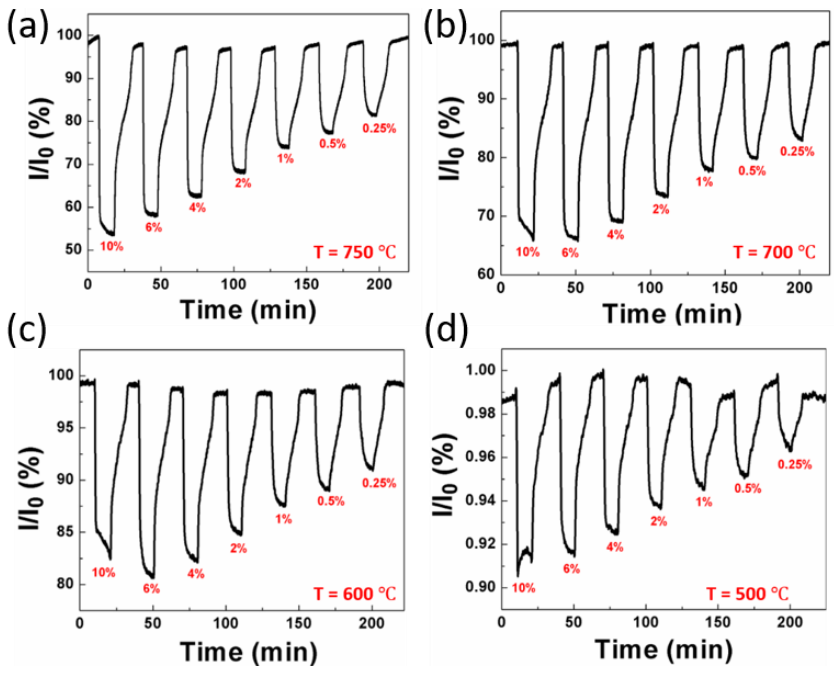

Figure 52. Response of sensor to various hydrogen concentrations at (a) 750 ℃, (b) 700 ℃, (c) 600 ℃, (d) 500 ℃.

In conclusion, we presented our works of developing distributed hydrogen sensor based on nanostructure-textured fiber surface at high temperature in this chapter. The functionality of the nanostructure has been confirmed in the experiment by both distributed and point sensing measurement. To further improve the detection limits, increasing the Pd doping level in the metal oxide sensory film would be very beneficial.

7.0 Conclusion and Future Work

In this dissertation, we presented our works in developing fiber optical sensors for the monitoring of natural gas and hydrogen gas. Multiple optical metrologies such as evanescent-wave absorption, Fabry-Perot interference, and optical frequency domain reflectometry were deployed for the development of the gas sensors.

In chapter 3, a methane sensor based on evanescent-wave interference was developed. Metal organic framework with the capability of capturing methane molecules was premixed with the polymer to form a functional coating on top of optical fiber as the new cladding. The sensory film expansion upon methane exposure introduces an enlarged refractive index mismatch between the sensory coating and fiber core, attenuating the transmitted light power in referring to the gas concentrations. The sensor performs a repetitive and reversible response with the high detection limit of 1%. Meanwhile, the functional coating was also proven to be highly compatible for multiple types of optical fibers with the large-scale capability, providing an easy, low-cost, and reliable solution for the monitoring of natural gas infrastructures.

In chapter 4, we improved the performance of hydrogen sensor in terms of the response speed, repeatability, and stability during continuously gas exposure by introducing the nanocone-textured optical fiber. The nanostructure was fabricated on top of the D-shaped fiber through direct ion etching followed by PdAu alloy film deposition as the sensory film. The nanostructure dramatically increases the surface-to-volume ratio of the functional film while preserving very limited light scattering, resulting more significant response with the accelerated sensory speed of more than 3 times. Meanwhile, compared with reference sensor with no surface texture, the time-dependent response of the sensor with nanostructure appears to be more stable with good

repeatability and reversibility, which, to large extent, is resulted from the alleviated internal strain of the functional film introduced by gas absorption that prevents the deterioration of the functional sensory film.

Chapter 5 of this dissertation focuses on the implement of Fabry-Perot interferometer on optical fiber for gas sensing. The intrinsic interference cavity was formed by two Rayleigh enhanced points with specific separating distance on optical fiber. The Rayleigh enhancement was achieved through femtosecond laser irradiation process. Multiple sensors were demonstrated in this chapter including a distributed hydrogen sensor operating at room temperature, a point hydrogen sensor working under high temperature, and a methane sensor. The distributed sensor shows high detection limits of 1% and spatial resolution of 5-mm. The slope of the response of point sensor at high temperature varies according to the hydrogen gas concentrations, which could be used for the hydrogen sensing in harsh environment such as the solid oxide fuel cell. Moreover, the expansion of the functional polymer coating was first confirmed by the methane IFPI sensor, providing solid evidence for better understanding of the principles in chapter 3.

In chapter 6, we presented our work of combing optical frequency domain reflectometry (OFDR) with nanograss-textured optical fiber to enhance the performance of the distributed optical sensor for hydrogen sensing at high temperature. Compared with sensors based on interferometer, sensor utilizing OFDR metrology has the advantages of high spatial resolution up to micrometer. Moreover, the optical sensor fabricated on top of the nanostructure-textured fiber surface demonstrates improved sensory performance in terms of the resolution. The time-dependent response of distributed sensor was also investigated to fully understand the sensory behavior.

Bibliography

[1] Q. Zhao, D. Ju, X. Deng, J. Huang, B. Cao, and X. J. S. r. Xu, "Morphology-modulation of SnO 2 hierarchical architectures by Zn doping for glycol gas sensing and photocatalytic applications," vol. 5, p. 7874, 2015.

[2] J. Zhang, E. Ding, S. Xu, Z. Li, X. Wang, and F. J. O. F. T. Song, "Sensitization of an optical fiber methane sensor with graphene," vol. 37, pp. 26-29, 2017.

[3] L. K. Verma *et al.*, "Self-cleaning and antireflective packaging glass for solar modules," vol. 36, no. 9, pp. 2489-2493, 2011.

[4] K. Keis, E. Magnusson, H. Lindström, S.-E. Lindquist, A. J. S. e. m. Hagfeldt, and s. cells, "A 5% efficient photoelectrochemical solar cell based on nanostructured ZnO electrodes," vol. 73, no. 1, pp. 51-58, 2002.

[5] Y.-C. Kim and Y. R. J. O. E. Do, "Nanohole-templated organic light-emitting diodes fabricated using laser-interfering lithography: moth-eye lighting," vol. 13, no. 5, pp. 1598-1603, 2005.

[6] H. Ono, Y. Ono, K. Kasahara, J. Mizuno, and S. J. J. J. o. A. P. Shoji, "Fabrication of high-intensity light-emitting diodes using nanostructures by ultraviolet nanoimprint lithography and electrodeposition," vol. 47, no. 2R, p. 933, 2008.

[7] G. Lozano, S. R. Rodriguez, M. A. Verschuuren, J. G. J. L. S. Rivas, and Applications, "Metallic nanostructures for efficient LED lighting," vol. 5, no. 6, p. e16080, 2016.

[8] M. E. Stewart *et al.*, "Nanostructured plasmonic sensors," vol. 108, no. 2, pp. 494-521, 2008.

[9] J.-H. J. S. Lee and A. B. Chemical, "Gas sensors using hierarchical and hollow oxide nanostructures: overview," vol. 140, no. 1, pp. 319-336, 2009.

[10] R. Kumar, O. Al-Dossary, G. Kumar, and A. J. N.-M. L. Umar, "Zinc oxide nanostructures for NO 2 gas–sensor applications: A review," vol. 7, no. 2, pp. 97-120, 2015.

[11] A. Kaniyoor, R. I. Jafri, T. Arockiadoss, and S. J. N. Ramaprabhu, "Nanostructured Pt decorated graphene and multi walled carbon nanotube based room temperature hydrogen gas sensor," vol. 1, no. 3, pp. 382-386, 2009.

[12] D. Infante *et al.*, "Durable, superhydrophobic, antireflection, and low haze glass surfaces using scalable metal dewetting nanostructuring," vol. 6, no. 6, pp. 429-440, 2013.

[13] J. W. Leem, Y. Yeh, and J. S. J. O. e. Yu, "Enhanced transmittance and hydrophilicity of nanostructured glass substrates with antireflective properties using disordered gold nanopatterns," vol. 20, no. 4, pp. 4056-4066, 2012.

[14] S. Ji, K. Song, T. B. Nguyen, N. Kim, H. J. A. a. m. Lim, and interfaces, "Optimal moth eye nanostructure array on transparent glass towards broadband antireflection," vol. 5, no. 21, pp. 10731-10737, 2013.

[15] T. Hoshii, R. Tamaki, K. Watanabe, M. Sugiyama, Y. Okada, and K. J. J. o. O. Miyano, "Maskless fabrication of broadband antireflection nanostructures on glass surfaces," vol. 18, no. 6, p. 064008, 2016.

[16] X. Ye *et al.*, "Formation of broadband antireflective and superhydrophilic subwavelength structures on fused silica using one-step self-masking reactive ion etching," vol. 5, p. 13023, 2015.

[17] M. E. Franke, T. J. Koplin, and U. J. s. Simon, "Metal and metal oxide nanoparticles in chemiresistors: does the nanoscale matter?," vol. 2, no. 1, pp. 36-50, 2006.

[18] D. Haridas, V. Gupta, and K. J. B. o. M. S. Sreenivas, "Enhanced catalytic activity of nanoscale platinum islands loaded onto SnO 2 thin film for sensitive LPG gas sensors," vol. 31, no. 3, pp. 397-400, 2008.

[19] C. Wang, L. Yin, L. Zhang, D. Xiang, and R. J. S. Gao, "Metal oxide gas sensors: sensitivity and influencing factors," vol. 10, no. 3, pp. 2088-2106, 2010.

[20] Z. Poole, P. Ohodnicki, A. Yan, Y. Lin, and K. J. a. p. a. Chen, "Sub-cm Resolution Distributed Fiber Optic Hydrogen Sensing with Nano-Engineered TiO2," 2015.

[21] A. Yan, S. Huang, S. Li, R. Chen, P. Ohodnicki, and K. Chen, "Fiber Optical Methane Sensors Using Functional Metal Oxide Nanomaterials," in *Asia-Pacific Optical Sensors Conference*, 2016, p. W4A. 12: Optical Society of America.

[22] W. J. T. C. R. Zhou, "Methane storage in porous metal− organic frameworks: current records and future perspectives," vol. 10, no. 3, pp. 200-204, 2010.

[23] R. B. Getman, Y.-S. Bae, C. E. Wilmer, and R. Q. J. C. r. Snurr, "Review and analysis of molecular simulations of methane, hydrogen, and acetylene storage in metal–organic frameworks," vol. 112, no. 2, pp. 703-723, 2011.

[24] K.-J. Kim, P. Lu, J. T. Culp, and P. R. J. A. s. Ohodnicki, "Metal–organic framework thin film coated optical fiber sensors: a novel waveguide-based chemical sensing platform," vol. 3, no. 2, pp. 386-394, 2018.

[25] R. Cao *et al.*, "Fiber Optical Sensor for Methane Detection Based on Metal-Organic Framework/Silicone Polymer Coating," in *CLEO: Applications and Technology*, 2018, p. JW2A. 168: Optical Society of America.

[26] X. Liu and W. J. A. C. Tan, "A fiber-optic evanescent wave DNA biosensor based on novel molecular beacons," vol. 71, no. 22, pp. 5054-5059, 1999.

[27] W. Cao, Y. J. S. Duan, and A. B. Chemical, "Optical fiber-based evanescent ammonia sensor," vol. 110, no. 2, pp. 252-259, 2005.

[28] S. Sekimoto *et al.*, "A fiber-optic evanescent-wave hydrogen gas sensor using palladium-supported tungsten oxide," vol. 66, no. 1-3, pp. 142-145, 2000.

[29] S. K. Khijwania, K. L. Srinivasan, J. P. J. S. Singh, and A. B. Chemical, "An evanescent-wave optical fiber relative humidity sensor with enhanced sensitivity," vol. 104, no. 2, pp. 217-222, 2005.

[30] L. Xu, J. C. Fanguy, K. Soni, and S. J. O. l. Tao, "Optical fiber humidity sensor based on evanescent-wave scattering," vol. 29, no. 11, pp. 1191-1193, 2004.

[31] A. Gaston, I. Lozano, F. Perez, F. Auza, and J. J. I. S. J. Sevilla, "Evanescent wave optical-fiber sensing (temperature, relative humidity, and pH sensors)," vol. 3, no. 6, pp. 806-811, 2003.

[32] D. J. A. O. Gloge, "Weakly guiding fibers," vol. 10, no. 10, pp. 2252-2258, 1971.

[33] Y. Tian, W. Wang, N. Wu, X. Zou, and X. J. S. Wang, "Tapered optical fiber sensor for label-free detection of biomolecules," vol. 11, no. 4, pp. 3780-3790, 2011.

[34] J. Villatoro and D. J. O. e. Monzón-Hernández, "Fast detection of hydrogen with nano fiber tapers coated with ultra thin palladium layers," vol. 13, no. 13, pp. 5087-5092, 2005.

[35] H. Tai, H. Tanaka, and T. J. O. l. Yoshino, "Fiber-optic evanescent-wave methane-gas sensor using optical absorption for the 3.392-μm line of a He–Ne laser," vol. 12, no. 6, pp. 437-439, 1987.

[36] E. Udd, *Fiber optic smart structures*. Wiley-Interscience, 1995.

[37] Z. Huang, Y. Zhu, X. Chen, and A. J. I. p. t. l. Wang, "Intrinsic Fabry-Pe/spl acute/rot fiber sensor for temperature and strain measurements," vol. 17, no. 11, pp. 2403-2405, 2005.

[38] D.-W. Duan, Y.-j. Rao, Y.-S. Hou, and T. J. A. o. Zhu, "Microbubble based fiber-optic Fabry–Perot interferometer formed by fusion splicing single-mode fibers for strain measurement," vol. 51, no. 8, pp. 1033-1036, 2012.

[39] G. Z. Xiao, A. Adnet, Z. Zhang, F. G. Sun, C. P. J. S. Grover, and A. A. Physical, "Monitoring changes in the refractive index of gases by means of a fiber optic Fabry-Perot interferometer sensor," vol. 118, no. 2, pp. 177-182, 2005.

[40] Y. Zhu and A. J. I. P. T. L. Wang, "Miniature fiber-optic pressure sensor," vol. 17, no. 2, pp. 447-449, 2005.

[41] A. Yan *et al.*, "Distributed Optical Fiber Sensors with Ultrafast Laser Enhanced Rayleigh Backscattering Profiles for Real-Time Monitoring of Solid Oxide Fuel Cell Operations," vol. 7, no. 1, p. 9360, 2017.

[42] C. da Silva Monteiro, "Optical Sensors Based on Fabry-Perot Interferometry," 2016.

[43] A. Yan, R. Chen, M. Zaghloul, Z. L. Poole, P. Ohodnicki, and K. P. J. I. P. T. L. Chen, "Sapphire fiber optical hydrogen sensors for high-temperature environments," vol. 28, no. 1, pp. 47-50, 2015.

[44] A. Kersey, T. Berkoff, and W. J. O. l. Morey, "Fiber-optic Bragg grating strain sensor with drift-compensated high-resolution interferometric wavelength-shift detection," vol. 18, no. 1, pp. 72-74, 1993.

[45] M. Islam, M. Ali, M.-H. Lai, K.-S. Lim, and H. J. S. Ahmad, "Chronology of Fabry-Perot interferometer fiber-optic sensors and their applications: a review," vol. 14, no. 4, pp. 7451-7488, 2014.

[46] T. Yoshino, K. Kurosawa, K. Itoh, T. J. I. T. o. M. T. Ose, and Techniques, "Fiber-optic Fabry-Perot interferometer and its sensor applications," vol. 30, no. 10, pp. 1612-1621, 1982.

[47] T. H. Chan *et al.*, "Fiber Bragg grating sensors for structural health monitoring of Tsing Ma bridge: Background and experimental observation," vol. 28, no. 5, pp. 648-659, 2006.

[48] J.-S. Heo, J.-H. Chung, J.-J. J. S. Lee, and A. A. Physical, "Tactile sensor arrays using fiber Bragg grating sensors," vol. 126, no. 2, pp. 312-327, 2006.

[49] S. V. Shatalin, V. N. Treschikov, and A. J. J. A. o. Rogers, "Interferometric optical time-domain reflectometry for distributed optical-fiber sensing," vol. 37, no. 24, pp. 5600-5604, 1998.

[50] T. Horiguchi and M. J. O. L. Tateda, "Optical-fiber-attenuation investigation using stimulated Brillouin scattering between a pulse and a continuous wave," vol. 14, no. 8, pp. 408-410, 1989.

[51] J. Dakin, D. Pratt, G. Bibby, and J. J. E. l. Ross, "Distributed optical fibre Raman temperature sensor using a semiconductor light source and detector," vol. 21, no. 13, pp. 569-570, 1985.

[52] K. Yüksel, M. Wuilpart, and P. J. O. e. Mégret, "Analysis and suppression of nonlinear frequency modulation in an optical frequency-domain reflectometer," vol. 17, no. 7, pp. 5845-5851, 2009.

[53] E. Karamehmedovic and U. Glombitza, "Fiber optic distributed temperature sensor using incoherent optical frequency domain reflectometry," in *Emerging Optoelectronic Applications*, 2004, vol. 5363, pp. 107-115: International Society for Optics and Photonics.

[54] S. Liehr, N. Nöther, K. J. M. S. Krebber, and Technology, "Incoherent optical frequency domain reflectometry and distributed strain detection in polymer optical fibers," vol. 21, no. 1, p. 017001, 2009.

[55] M. Froggatt, T. Erdogan, J. Moore, and S. Shenk, "Optical frequency domain characterization (OFDC) of dispersion in optical fiber Bragg gratings," in *Bragg Gratings, Photosensitivity, and Poling in Glass Waveguides*, 1999, p. BC2: Optical Society of America.

[56] M. Froggatt, J. Moore, and T. Erdogan, "Full complex transmission and reflection characterization of a Bragg grating in a single laser sweep," in *Optical Fiber Communication Conference*, 2000, p. WB1: Optical Society of America.

[57] U. Glombitza and E. J. J. o. L. t. Brinkmeyer, "Coherent frequency-domain reflectometry for characterization of single-mode integrated-optical waveguides," vol. 11, no. 8, pp. 1377-1384, 1993.

[58] B. J. Soller, D. K. Gifford, M. S. Wolfe, and M. E. J. O. E. Froggatt, "High resolution optical frequency domain reflectometry for characterization of components and assemblies," vol. 13, no. 2, pp. 666-674, 2005.

[59] A. K. Sang, M. E. Froggatt, D. K. Gifford, S. T. Kreger, and B. D. J. I. S. J. Dickerson, "One centimeter spatial resolution temperature measurements in a nuclear reactor using Rayleigh scatter in optical fiber," vol. 8, no. 7, pp. 1375-1380, 2008.

[60] G. Stewart, W. Jin, B. J. S. Culshaw, and A. B. Chemical, "Prospects for fibre-optic evanescent-field gas sensors using absorption in the near-infrared," vol. 38, no. 1-3, pp. 42-47, 1997.

[61] M. Benounis, N. Jaffrezic-Renault, J.-P. Dutasta, K. Cherif, A. J. S. Abdelghani, and A. B. Chemical, "Study of a new evanescent wave optical fibre sensor for methane detection based on cryptophane molecules," vol. 107, no. 1, pp. 32-39, 2005.

[62] N. Gayraud *et al.*, "Mid-infrared methane detection in a photonic bandgap fiber using a broadband optical parametric oscillator," vol. 15, no. 18, pp. 11219-11224, 2007.

[63] J. Yang *et al.*, "Photonic crystal fiber methane sensor based on modal interference with an ultraviolet curable fluoro-siloxane nano-film incorporating cryptophane A," vol. 235, pp. 717-722, 2016.

[64] A. Cubillas, J. Lazaro, O. Conde, M. Petrovich, and J. J. S. Lopez-Higuera, "Gas sensor based on photonic crystal fibres in the 2ν3 and ν2+ 2ν3 vibrational bands of methane," vol. 9, no. 8, pp. 6261-6272, 2009.

[65] S.-G. Li *et al.*, "Study of the sensitivity of gas sensing by use of index-guiding photonic crystal fibers," vol. 46, no. 22, pp. 5183-5188, 2007.

[66] M. A. Nasalevich, M. G. Goesten, T. J. Savenije, F. Kapteijn, and J. J. C. C. Gascon, "Enhancing optical absorption of metal–organic frameworks for improved visible light photocatalysis," vol. 49, no. 90, pp. 10575-10577, 2013.

[67] J. Yang, C. Tao, X. Li, G. Zhu, and W. J. O. e. Chen, "Long-period fiber grating sensor with a styrene-acrylonitrile nano-film incorporating cryptophane A for methane detection," vol. 19, no. 15, pp. 14696-14706, 2011.

[68] J. Yang *et al.*, "Sensitivity enhancing of transition mode long-period fiber grating as methane sensor using high refractive index polycarbonate/cryptophane A overlay deposition," vol. 207, pp. 477-480, 2015.

[69] A. Cubillas, M. Silva-Lopez, J. Lazaro, O. Conde, M. Petrovich, and J. J. O. E. Lopez-Higuera, "Methane detection at 1670-nm band using a hollow-core photonic bandgap fiber and a multiline algorithm," vol. 15, no. 26, pp. 17570-17576, 2007.

[70] T. Ritari *et al.*, "Gas sensing using air-guiding photonic bandgap fibers," vol. 12, no. 17, pp. 4080-4087, 2004.

[71] X. Chong, K.-J. Kim, P. R. Ohodnicki, E. Li, C.-H. Chang, and A. X. J. I. S. J. Wang, "Ultrashort near-infrared fiber-optic sensors for carbon dioxide detection," vol. 15, no. 9, pp. 5327-5332, 2015.

[72] F. De-Jun, Z. Mao-Sen, G. Liu, L. Xi-Lu, and J. J. I. S. J. Dong-Fang, "D-shaped plastic optical fiber sensor for testing refractive index," vol. 14, no. 5, pp. 1673-1676, 2014.

[73] Y. Zhang, C. Gu, A. Schwartzberg, and J. J. A. P. L. Zhang, "Surface-enhanced Raman scattering sensor based on D-shaped fiber," vol. 87, no. 12, p. 123105, 2005.

[74] N. Luan, R. Wang, W. Lv, and J. J. O. e. Yao, "Surface plasmon resonance sensor based on D-shaped microstructured optical fiber with hollow core," vol. 23, no. 7, pp. 8576-8582, 2015.

[75] X. Zeng *et al.*, "Hydrogen gas sensing with networks of ultrasmall palladium nanowires formed on filtration membranes," vol. 11, no. 1, pp. 262-268, 2010.

[76] A. Esfandiar, A. Irajizad, O. Akhavan, S. Ghasemi, and M. R. J. i. j. o. h. e. Gholami, "Pd–WO3/reduced graphene oxide hierarchical nanostructures as efficient hydrogen gas sensors," vol. 39, no. 15, pp. 8169-8179, 2014.

[77] M. A. J. J. o. t. E. S. Butler, "Fiber optic sensor for hydrogen concentrations near the explosive limit," vol. 138, no. 9, pp. L46-L47, 1991.

[78] C.-L. Tien, H.-W. Chen, W.-F. Liu, S.-S. Jyu, S.-W. Lin, and Y.-S. J. T. S. F. Lin, "Hydrogen sensor based on side-polished fiber Bragg gratings coated with thin palladium film," vol. 516, no. 16, pp. 5360-5363, 2008.

[79] J. Villatoro, A. Díez, J. L. Cruz, and M. V. J. I. s. j. Andres, "In-line highly sensitive hydrogen sensor based on palladium-coated single-mode tapered fibers," vol. 3, no. 4, pp. 533-537, 2003.

[80] Z. Zhao, M. Carpenter, H. Xia, D. J. S. Welch, and A. B. Chemical, "All-optical hydrogen sensor based on a high alloy content palladium thin film," vol. 113, no. 1, pp. 532-538, 2006.

[81] M. Ramanathan, G. Skudlarek, H. Wang, and S. J. N. Darling, "Crossover behavior in the hydrogen sensing mechanism for palladium ultrathin films," vol. 21, no. 12, p. 125501, 2010.

[82] T. Xu *et al.*, "Self-assembled monolayer-enhanced hydrogen sensing with ultrathin palladium films," vol. 86, no. 20, p. 203104, 2005.

[83] E. Lee, J. M. Lee, J. H. Koo, W. Lee, and T. J. I. j. o. h. e. Lee, "Hysteresis behavior of electrical resistance in Pd thin films during the process of absorption and desorption of hydrogen gas," vol. 35, no. 13, pp. 6984-6991, 2010.

[84] A. J. A. E. M. Pundt, "Hydrogen in nano‐sized metals," vol. 6, no. 1‐2, pp. 11-21, 2004.

[85] Z. Chen, J. Jie, L. Luo, H. Wang, C. Lee, and S. J. N. Lee, "Applications of silicon nanowires functionalized with palladium nanoparticles in hydrogen sensors," vol. 18, no. 34, p. 345502, 2007.

[86] V. R. Khalap, T. Sheps, A. A. Kane, and P. G. J. N. l. Collins, "Hydrogen sensing and sensitivity of palladium-decorated single-walled carbon nanotubes with defects," vol. 10, no. 3, pp. 896-901, 2010.

[87] Y.-T. Pan, X. Yin, K. S. Kwok, and H. J. N. l. Yang, "Higher-order nanostructures of two-dimensional palladium nanosheets for fast hydrogen sensing," vol. 14, no. 10, pp. 5953-5959, 2014.

[88] K. T. Kim, J. Sim, and S. M. J. I. S. J. Cho, "Hydrogen gas sensor using Pd nanowires electro-deposited into anodized alumina template," vol. 6, no. 3, pp. 509-513, 2006.

[89] X. Wei, T. Wei, H. Xiao, Y. J. S. Lin, and A. B. Chemical, "Nano-structured Pd-long period fiber gratings integrated optical sensor for hydrogen detection," vol. 134, no. 2, pp. 687-693, 2008.

[90] P. Ohodnicki, J. Baltrus, T. J. S. Brown, and A. B. Chemical, "Pd/SiO2 and AuPd/SiO2 nanocomposite-based optical fiber sensors for H2 sensing applications," vol. 214, pp. 159-168, 2015.

[91] D. Monzón-Hernández, D. Luna-Moreno, D. J. S. Martínez-Escobar, and A. B. Chemical, "Fast response fiber optic hydrogen sensor based on palladium and gold nano-layers," vol. 136, no. 2, pp. 562-566, 2009.

[92] Z. L. Poole, P. R. Ohodnicki, A. Yan, Y. Lin, and K. P. J. A. s. Chen, "Potential to detect hydrogen concentration gradients with palladium infused mesoporous-titania on D-shaped optical fiber," vol. 2, no. 1, pp. 87-91, 2016.

[93] D. Luna-Moreno, D. Monzón-Hernández, J. Villatoro, G. J. S. Badenes, and A. B. Chemical, "Optical fiber hydrogen sensor based on core diameter mismatch and annealed Pd–Au thin films," vol. 125, no. 1, pp. 66-71, 2007.

[94] K. J. Jeon, J. M. Lee, E. Lee, and W. J. N. Lee, "Individual Pd nanowire hydrogen sensors fabricated by electron-beam lithography," vol. 20, no. 13, p. 135502, 2009.

[95] E. Menke, M. Thompson, C. Xiang, L. Yang, and R. J. N. m. Penner, "Lithographically patterned nanowire electrodeposition," vol. 5, no. 11, p. 914, 2006.

[96] S. Yu, U. Welp, L. Z. Hua, A. Rydh, W. K. Kwok, and H. H. J. C. o. M. Wang, "Fabrication of palladium nanotubes and their application in hydrogen sensing," vol. 17, no. 13, pp. 3445-3450, 2005.

[97] F. Yang, S.-C. Kung, M. Cheng, J. C. Hemminger, and R. M. J. A. N. Penner, "Smaller is faster and more sensitive: the effect of wire size on the detection of hydrogen by single palladium nanowires," vol. 4, no. 9, pp. 5233-5244, 2010.

[98] F. Yang, D. K. Taggart, and R. M. J. s. Penner, "Joule heating a palladium nanowire sensor for accelerated response and recovery to hydrogen gas," vol. 6, no. 13, pp. 1422-1429, 2010.

[99] A. O. Dikovska *et al.*, "Optical sensing of ammonia using ZnO nanostructure grown on a side-polished optical-fiber," vol. 146, no. 1, pp. 331-336, 2010.

[100] E. Walter *et al.*, "Sensors from electrodeposited metal nanowires," vol. 34, no. 1, pp. 409-412, 2002.

[101] F. Favier, E. C. Walter, M. P. Zach, T. Benter, and R. M. J. S. Penner, "Hydrogen sensors and switches from electrodeposited palladium mesowire arrays," vol. 293, no. 5538, pp. 2227-2231, 2001.

[102] Y. Ou *et al.*, "Nanostructures of Pd–Ni alloy deposited on carbon fibers for sensing hydrogen," vol. 569, pp. 130-135, 2013.

[103] A. Mandelis, J. A. J. S. Garcia, and A. B. Chemical, "Pd/PVDF thin film hydrogen sensor based on laser-amplitude-modulated optical-transmittance: dependence on H2 concentration and device physics," vol. 49, no. 3, pp. 258-267, 1998.

[104] Z. Zhao and M. J. J. o. a. p. Carpenter, "Annealing enhanced hydrogen absorption in nanocrystalline Pd ／ Au sensing films," vol. 97, no. 12, p. 124301, 2005.

[105] T. Karabacak, C. R. Picu, J. J. Senkevich, G.-C. Wang, and T.-M. J. J. o. A. P. Lu, "Stress reduction in tungsten films using nanostructured compliant layers," vol. 96, no. 10, pp. 5740-5746, 2004.

[106] I. J. S. Lundström and actuators, "Hydrogen sensitive MOS-structures: part 1: principles and applications," vol. 1, pp. 403-426, 1981.

[107] O. L. Muskens, J. G. Rivas, R. E. Algra, E. P. Bakkers, and A. J. N. l. Lagendijk, "Design of light scattering in nanowire materials for photovoltaic applications," vol. 8, no. 9, pp. 2638-2642, 2008.

[108] P. R. Ohodnicki Jr *et al.*, "High temperature optical sensing of gas and temperature using Au-nanoparticle incorporated oxides," vol. 202, pp. 489-499, 2014.

[109] D. Zalvidea, A. Diez, J. Cruz, M. J. S. Andrés, and A. B. Chemical, "Hydrogen sensor based on a palladium-coated fibre-taper with improved time-response," vol. 114, no. 1, pp. 268-274, 2006.

[110] M. Li, M. Wang, and H. J. O. E. Li, "Optical MEMS pressure sensor based on Fabry-Perot interferometry," vol. 14, no. 4, pp. 1497-1504, 2006.

[111] L. H. Chen *et al.*, "Chitosan based fiber-optic Fabry–Perot humidity sensor," vol. 169, pp. 167-172, 2012.

[112] C. Belleville and G. J. O. l. Duplain, "White-light interferometric multimode fiber-optic strain sensor," vol. 18, no. 1, pp. 78-80, 1993.

[113] H. Y. Choi, K. S. Park, S. J. Park, U.-C. Paek, B. H. Lee, and E. S. J. O. l. Choi, "Miniature fiber-optic high temperature sensor based on a hybrid structured Fabry–Perot interferometer," vol. 33, no. 21, pp. 2455-2457, 2008.

[114] V. Bhatia *et al.*, "Optical fibre based absolute extrinsic Fabry-Perot interferometric sensing system," vol. 7, no. 1, p. 58, 1996.

[115] A. Wang, H. Xiao, J. Wang, Z. Wang, W. Zhao, and R. J. J. o. l. t. May, "Self-calibrated interferometric-intensity-based optical fiber sensors," vol. 19, no. 10, p. 1495, 2001.

[116] Y. Zhang, X. Chen, Y. Wang, K. L. Cooper, and A. J. J. o. l. t. Wang, "Microgap Multicavity Fabry–Pérot Biosensor," vol. 25, no. 7, pp. 1797-1804, 2007.

[117] Y. Yang *et al.*, "A high-resolution dynamic fiber-optic inclinometer," vol. 283, pp. 305-312, 2018.

[118] Y. Yang, E. Wang, K. Chen, Z. Yu, and Q. J. I. S. J. Yu, "Fiber-Optic Fabry–Perot Sensor for Simultaneous Measurement of Tilt Angle and Vibration Acceleration," vol. 19, no. 6, pp. 2162-2169, 2018.

[119] Z. Yu and A. J. I. P. T. L. Wang, "Fast white light interferometry demodulation algorithm for low-finesse Fabry–Pérot sensors," vol. 27, no. 8, pp. 817-820, 2015.

[120] J. Eastman, L. Thompson, and B. J. P. R. B. Kestel, "Narrowing of the palladium-hydrogen miscibility gap in nanocrystalline palladium," vol. 48, no. 1, p. 84, 1993.

[121] H. Peisl, "Lattice strains due to hydrogen in metals," in *Hydrogen in metals I*: Springer, 1978, pp. 53-74.

[122] Z. Hu, T. Thundat, and R. J. J. o. A. P. Warmack, "Investigation of adsorption and absorption-induced stresses using microcantilever sensors," vol. 90, no. 1, pp. 427-431, 2001.

[123] A. De Ninno, V. Violante, and A. J. P. R. B. La Barbera, "Consequences of lattice expansive strain gradients on hydrogen loading in palladium," vol. 56, no. 5, p. 2417, 1997.

[124] T. L. Pedersen, C. Liesch, C. Salinga, T. Eleftheriadis, H. Weis, and M. J. T. S. F. Wuttig, "Hydrogen-induced changes of mechanical stress and optical transmission in thin Pd films," vol. 458, no. 1-2, pp. 299-303, 2004.

[125] M. Butler and D. J. J. o. a. p. Ginley, "Hydrogen sensing with palladium ‐ coated optical fibers," vol. 64, no. 7, pp. 3706-3712, 1988.

[126] A. Yan, Z. L. Poole, R. Chen, P. W. Leu, P. Ohodnicki, and K. P. J. J. Chen, "Scalable fabrication of metal oxide functional materials and their applications in high-temperature optical sensing," vol. 67, no. 1, pp. 53-58, 2015.

[127] Z. L. Poole, P. Ohodnicki, R. Chen, Y. Lin, and K. P. J. O. e. Chen, "Engineering metal oxide nanostructures for the fiber optic sensor platform," vol. 22, no. 3, pp. 2665-2674, 2014.

[128] T. Kurashima, T. Horiguchi, and M. J. O. l. Tateda, "Distributed-temperature sensing using stimulated Brillouin scattering in optical silica fibers," vol. 15, no. 18, pp. 1038-1040, 1990.

[129] M. Froggatt and J. J. A. O. Moore, "High-spatial-resolution distributed strain measurement in optical fiber with Rayleigh scatter," vol. 37, no. 10, pp. 1735-1740, 1998.

[130] T. Parker, M. Farhadiroushan, V. Handerek, and A. J. I. P. T. L. Roger, "A fully distributed simultaneous strain and temperature sensor using spontaneous Brillouin backscatter," vol. 9, no. 7, pp. 979-981, 1997.

[131] S. Sumida *et al.*, "Distributed hydrogen determination with fiber-optic sensor," vol. 108, no. 1-2, pp. 508-514, 2005.